

MEASURING CONFORMATIONAL DYNAMICS OF
BIOLOGICAL MOLECULES WITH SINGLE-MOLECULE
TRACKING AND FLUORESCENCE CORRELATION
SPECTROSCOPY

A DISSERTATION
SUBMITTED TO THE DEPARTMENT OF APPLIED PHYSICS
AND THE COMMITTEE ON GRADUATE STUDIES
OF STANFORD UNIVERSITY
IN PARTIAL FULFILLMENT OF THE REQUIREMENTS
FOR THE DEGREE OF
DOCTOR OF PHILOSOPHY

Charles Limouse
August 2014

© 2014 by Charles Bruno Maurice Limouse. All Rights Reserved.
Re-distributed by Stanford University under license with the author.



This work is licensed under a Creative Commons Attribution-Noncommercial 3.0 United States License.
<http://creativecommons.org/licenses/by-nc/3.0/us/>

This dissertation is online at: <http://purl.stanford.edu/yy851sh8400>

I certify that I have read this dissertation and that, in my opinion, it is fully adequate in scope and quality as a dissertation for the degree of Doctor of Philosophy.

Hideo Mabuchi, Primary Adviser

I certify that I have read this dissertation and that, in my opinion, it is fully adequate in scope and quality as a dissertation for the degree of Doctor of Philosophy.

Andrew Spakowitz

I certify that I have read this dissertation and that, in my opinion, it is fully adequate in scope and quality as a dissertation for the degree of Doctor of Philosophy.

Aaron Straight

Approved for the Stanford University Committee on Graduate Studies.

Patricia J. Gumport, Vice Provost for Graduate Education

This signature page was generated electronically upon submission of this dissertation in electronic format. An original signed hard copy of the signature page is on file in University Archives.

Abstract

The past two decades have seen great advances in single-molecule techniques capable of probing biomolecular systems with spatial resolution down to the nanometer level. However few techniques are specifically designed to measure larger scale organization between a few tens and a few hundreds of nanometers, especially when other figures of merit are considered, such as high time-resolution or the possibility to do measurements in bulk and without immobilization. Such features would be particularly useful in the study of molecular structures like chromatin or other nucleoprotein complexes, that exhibit organizational details and dynamics across a broad range of time and length scales.

I present how the combination of fluorescence correlation spectroscopy (FCS) and single molecule tracking can be used to measure the conformational dynamics of molecules that diffuse freely in solution, at the scale of a few tens of nanometers. I discuss some aspects of the instrumentation as well as the parameters that define the spatial and temporal resolution. I describe other advantages of the technique such as the possibility to bypass a common difficulty associated with fluorescence correlation measurements and obtain a signal that is not convolved with the blinking dynamics of the fluorescent probe itself. Finally I present an experimental proof-of-principle where tracking-FCS was applied to measure the end-to-end Brownian dynamics of short DNA fragments in the semiflexible regime.

Acknowledgments

First, I would like to thank my advisor Hideo. I truly had an incredible chance to do my thesis under Hideos guidance. Hideo has put a lot of trust in me for continuing the efforts on the biology side of the lab, and I am deeply thankful to him for giving me this opportunity. Developing the tracking microscope, and trying to decipher some chromatin biology questions has been an incredibly exciting and enjoyable project that allowed me to learn a lot of different things. It really did take me a lot of time to get to the point in the project where interesting things could happen, but Hideo relentlessly supported me and guided me in this effort. I am extremely thankful for his patience, and for giving me the time and the encouragements to really pursue the things I was the most interested in, without fear of the difficulties ahead. I believe it is important to have this opportunity in graduate school to mature as a scientist. My labmate Jie once said the probability of finding another Hideo is zero, and this really is an accurate statement. Hideo is unique in many ways, but his kindness, his modesty and curiosity-driven approach to science are things that have really inspired me and that I believe I will often reflect back onto in the later stages of my path.

Perhaps a privilege of belonging to the minority of people in the lab working with visible light as well as pipettes, I had the chance to have in fact not one, but two advisors. Aaron did so well at convincing me that chromatin was awesome, that I ended up spending probably almost as much time doing or attempting to do biology in Beckman, as in my own lab. Aaron has been a fantastic mentor, and I have learned an immense amount from him. None of my work would have been possible or nearly as fun without his help and relentless excitement to put the tracking microscope to good use. In whatever endeavors life carries me, I will never forget that the best attitude and possibly the solution to practically any problem is to attack attack attack! Also, Aarons firm belief before each experiment that how could it possibly not work has certainly contributed to my desire to pursue my path in the academic world. After all, how could it possibly not work!

I would like to thank Andy, who in addition to being on my thesis committee, has provided me with valuable advice and suggestions throughout my PhD. I am thankful

for his interest in my work and the multiple discussions we had. His students, Tom in particular, have given me inputs on my work as well.

The entire group of students in the Mabuchi lab has been an incredible group of labmates and friends. As nerdy as this can sound, doing science among them might very well have been the best refuge on campus. I would like to thank in particular Mikey who was my unique true bio and tracking labmate for the most part of my PhD. Sharing the tracking instrument was an adventure, and he and I became very close friends. In the small bio universe of the Mabuchi lab, many thanks go to Kevin McHale as well, who introduced me first to single molecule tracking.

Everyone in the Mabuchi lab has been important in his own unique way. Dmitri has been my consultant mathematician and helped me with statistics and probability problems on regular basis. Yeong Dae started his PhD at the same time as I did, and has always been a wonderful friend and scientific colleague to talk to. He and I both enjoyed working late at night, and it was great to have him around. Gopal has been an attentive and close friend and I will remember for a long time many of our discussions together. Jie is an incredibly kind and giving person, and has been here to share advice with me. Hardeep has been very good at taking care of my (and other peoples!) constant need for caffeine. He has also been the electronics wizard (alongside Dr. Mikey), always ready to help out with these sort of things. I cannot be more thankful to Dodd and Chris for coping with my need to keep the lights off in the microscope room, which was as frequent as it was unpredictable. Nina has helped me with Stochastic calculus and Nate with instrumentation control. I thank Jeff for giving me advice on various practical things regarding life abroad. Nick is the best programmer I have ever met, and I thank him for his regular help with computer related things and for converting me to python. Joe, Tony and Orion have been some of the first people to welcome me in the lab. Last but not least, the lab for sure would not be the same without Dr. Mikey. Mikey holds the prize for the most acknowledged labmate at PhD defenses, and he truly deserves it. Thanks Dr. Mikey for knowing everything about optics and electronics. Despite his intimidating earphones, Mikey does listen and is in fact the most selfless of all of us. He has spent time helping with so many things for the bio experiments.

In the Straight lab, I would like to say a special thank you to Colin, who shared his bench with me for a while and taught me many essential biology skills. Special thanks go to Fred as well, my tennis partner and best British friend. Entering room 411 in Beckman and hearing Ah the Frenchman! has always been a cheerful way to start the day at the bench. To all the other people in the Straight lab: Whitney, Bradley, Shengya, Matt, Jason, Annika, Topher, Ben, Teddy, Amanda and Namita, thank you for including me as an authentic Straight Lab person. You are all incredible scientists and amazing people and I have learned tons from you. In the Biochemistry faculty, I would also like to say thank you to Suzanne Pfeffer. Suzanne has been very kind to embark me onboard her research on membrane trafficking, and she has provided me with a lot of scientific and personal guidance. Patricia, in her lab, is the best scientific collaborator I have ever worked with, and I am very thankful we have been able to work together on the GCC185 project. I thank all of my friends I have made at Stanford in general, James, Liz, Aakash, Christine, JongMin, Michelle and many others.

Paula and Claire are doing a lot more than just taking care of the administrative side of the Applied Physics department, and thanks to them I really felt at home in AP. Thank you Paula and Claire. I am also thankful to the Stanford Biochemistry department for treating me as one of their own students.

Looking back to times before Stanford, I would like to thank Prof. Prentiss, who first introduced me to Biophysics and had an influential contribution to my desire to pursue a PhD in that field. I would also like to thank my English professor in college, Prof. Gusdorf, who was influential in my coming to the US. One of my best college friends Stephane is getting married this weekend, and I am thinking of him. I thank Stephane for being an incredibly supportive friend when I was applying to graduate school. He is part of the group of friends who were very important in my undergraduate life. In the moments I shared with them, especially during rowing, I have learned things that have been important in graduate school. Thank you to all my friends of the aviron section (BAJ).

Most importantly, I would like to thank my family infinitely. My family has given me such inspiration, strength and happiness throughout my life and the distance did

not change any of that. I am thinking of my grandmother Yo, who I am sure would have been very happy to see me get my PhD degree. I am also thankful to Anh's family for their continuous support. Finally, I would like to tell all of my gratitude for the most special person in my life. Anh has walked by my side during a large part of my journey in graduate school. Her support is an unmatched source of energy and joy. She has been my lucky star here at Stanford.

Contents

1	Introduction	1
1.1	Biological motivation	1
1.2	A brief history of single particle tracking in confocal microscopy . . .	3
1.3	Single molecule tracking is more than recording trajectories, and why FCS	6
1.4	Context with respect to previous work in the lab	7
1.5	Thesis organization	9
2	Tracking-FCS: theory and data analysis	10
2.1	Theory of fluorescence correlation functions in tracking-FCS	11
2.1.1	General expression of fluorescence correlation functions	11
2.1.2	First experimental test	16
2.1.3	Effects of background and tracking error	17
2.1.4	Tracking-FCS in a steep intensity profile: optimization of illumination conditions	21
2.2	Optimal performance of tracking-FCS and resolution	27
2.2.1	Noise on the correlation function	27
2.2.2	Optimal performance of tracking-FCS and spatio-temporal resolution	32
2.3	Deconvolution of fluorescence correlation functions and dye-blinking free signals	35
2.3.1	The convolution problem in FCS	35
2.3.2	Natural suppression of dye blinking from tracking-FCS signals	37

2.3.3	Model-free extraction of position dynamics from fluorescence correlation data	39
2.3.4	Suppression of tracking-error and extraction of the correlation function for the internal dynamics	41
2.4	Switched-illumination tracking-FCS and single molecule deconvolution of the dye dynamics	42
3	Instrumentation and tracking performance	46
3.1	Optical design	46
3.1.1	General principles and original design	46
3.1.2	Redesigned apparatus	49
3.1.3	Remote axial scanning using a relay objective lens in double pass configuration	53
3.1.4	Wide-band axial scanning and positioning using a Tunable Acoustic Gradient lens and an elastic polymer lens	56
3.2	Mathematical description of the tracking dynamics	62
3.2.1	General model for the tracking system dynamics	62
3.2.2	Mean square displacement of stage and laser	65
3.2.3	Model-free fitting of experimental correlation functions	67
3.2.4	Optimal tracking performance	68
4	End-to-end dynamics of DNA with tracking-FCS	71
4.1	Results	71
4.1.1	Description of the experiment	71
4.1.2	Background correction	72
4.1.3	Raw correlation functions	74
4.2	Initial data with switched-tFCS	83
4.3	Methods	87
5	Future improvements and concluding remarks	89
5.1	Future Instrumentation developments	89
5.1.1	Tracking bandwidth and axial control	89

5.1.2	Feedback loop in low photon count or large background regime	90
5.1.3	Tunable beam waist	90
5.2	Improvements and extensions of the tracking-FCS assay	91
5.2.1	Measuring static distances	91
5.2.2	Better Suppression of the tracking error	92
5.3	Conclusion and perspective	92
Bibliography		95

List of Figures

2.1	Schematic of the tracking-FCS assay	11
2.2	Calibration tracking-FCS data on immobilized beads	17
2.3	Simulated tracking-FCS data in centered and side illumination geometry	23
2.4	Sensitivity of the correlation function to probe motion	26
2.5	Spatial resolution $\sigma_{im,min}$ function of beam offset δ at timescales $\tau = 1\mu s$ (green and red) and $\tau = 100\mu s$ (black and blue) for various noise levels ($k = 0, 0.1, 0.2, 0.5$) and in presence of tracking error (blue and red, $\sigma_{err} = 100nm$) or with perfect tracking (black and green)	34
2.6	Optimal probe beam localization	35
2.7	Normalized and calibrated relative correlation function	41
2.8	tracking-FCS data processing workflow	42
2.9	Principle of switched-illumination tracking-FCS	43
3.1	Optical design of the tracking microscope	55
3.2	Picture of the tracking microscope in 2013	56
3.3	Picture of the TAG lens for axial scanning	57
3.4	Optical layout for the TAG lens	61
3.5	Tracking feedback loop	63
3.6	Tracking localization as a function of optimal tracking bandwidth . .	69
4.1	Molecule brightness classification and background correction	73
4.2	Background correlation functions	74
4.3	Raw correlation functions 472bp and 979bp	75
4.4	Relative correlation functions 470bp and 979bp	77

4.5	Detection of end-to-end dynamics in 470bp and 979bp DNA fragemnts: raw data	78
4.6	Normalized relative correlation functions using calibrated value of off- set. for all 4 samples and differences between OS (bottom) and SS (top) samples. Same plotting conventions as in fig. 4.3, ie. color rep- resents value of offset δ_1 . We discarded the smaller offset (green in previous figure) as the data at this offset were very noisy.	79
4.7	Normalized relative correlation functions 470bp and 979bp	80
4.8	Probe position correlation functions 472bp and 979bp	81
4.9	Probe position correlation functions 472bp and 979bp (calibration free approach)	82
4.10	End-to-end Position correlation functions 472bp and 979bp	83
4.11	Typical tracking-FCS data with switched illumination	84
4.12	Switched tracking-FCS data for DNA of various length: normalized relative correlation functions	86
4.13	Switched tracking-FCS data for DNA of various length: end-to-end correlation functions	86
4.14	Schematic of DNA labeling protocol	88

Chapter 1

Introduction

1.1 Biological motivation

Processes occurring across various length scales and time scales cohabit inside living cells. While a vast array of functions are performed by the activity of individual molecular components (nm scale), many higher level cellular functions, such as the regulation of gene expression, replication or intercellular transport, involve organization and dynamics of larger scale structures spanning tens to hundreds of nanometers. Mechanisms that drive organizational changes on these length scales are of critical importance, yet they are very difficult to probe with current measurement technologies.

To pause on a concrete example, we can look at the regulation pathways that involve physical contact between remote loci on the genome. Such pathways are ubiquitous and rely on communication between sites separated by distances ranging from a few tens of base pairs (bp) to several Mbp. For example, LacR mediated repression of the lac operon requires contact between Lac operators located from 40bp to 900bp away from each other [1]. Lambda-phage lysogenic cycle is controlled by the CI protein which induces the formation of a loop between regulatory Or and Ol sites that are distant by 2.3kbp [1, 2]. On longer length scales, the imprinted Igf2 and H19 genes are about 100kb apart and are reciprocally expressed in a differential parent-of-origin dependent manner [3, 4, 5]. The expression pattern of these two genes

is dependent on the binding of CTCF protein which drives a global reorganization of this large locus. This reorganization involves the formation of loops between the promoters of Igf2 and H19, the shared enhancers thousands of bp downstream of H19, and a differentially methylated region located in between Igf2 and H19 loci. Finally at the scale of entire chromosomes, increasing evidence is emerging suggesting that long range (Mbp) contacts play a major role in the establishment of chromosome domains and the coordinated activation or repression of genes during development [6, 7]. In all these examples, chromatin organization is modulated on length scales ranging from a few tens to a few hundreds of nm via an interplay between DNA binding factors and regulatory elements.

Unfortunately, even in the best studied systems, the mechanisms by which such long range interactions and loops are formed and maintained in the genome, and how they affect the dynamics of transcription remain poorly understood. Most of our knowledge comes from genetic studies or chromosome configuration capture methods, which indirectly indicate the existence of loops and cannot reveal their dynamics [8, 9]. In fact, besides a few specific examples [2], it remains extremely difficult to detect contacts between distant loci in live cells and distinguish them from the large background of random contacts.

A key to our understanding of these regulatory processes certainly resides in the development of techniques suited for the detection and ideally the visualization through time of the conformational changes occurring at this intermediate length scale (that is, between a few tens and a few hundreds of nanometers). Such techniques could greatly help us understand the molecular mechanisms underlying the activity of regulatory proteins (for ex. Binding of LacR, or binding of CTCF)

The last decade has seen great advances in both single-molecule and super resolution fluorescence microscopy techniques. Since the introduction of STED microscopy, a large array of imaging techniques that beat the diffraction limit using various strategies have been developed (see [10] for a review and [11, 12, 10, 8] for a few examples). These techniques have yielded unprecedented insights into numerous biological processes, but they still lack the temporal resolution necessary to tackle dynamical processes such as the ones discussed.

On the other end of the spectrum, several *in vitro* single molecule methods have the ability to measure fast processes and are suitable for monitoring the conformational changes of large structures. DNA looping processes have been studied through tethered particle assays for example [13, 14]. However, most of the common techniques rely on some form of surface immobilization, which complicates the experimental design, as immobilization strategies need to be worked out and characterized. More importantly, surface immobilization precludes the possibility of applying the *in-vivo*.

There is arguably therefore a gap in the landscape of available techniques. For the specific purpose of monitoring dynamics of large molecular assemblies, it would be extremely valuable to develop techniques that do not necessarily have nm spatial resolution (coarse grained resolution the few tens of nm level is sufficient), but that retain the temporal resolution of *in vitro* single molecule assays.

In an effort to provide one possible piece of this puzzle, we sought in this work to develop assays based on feedback based single molecule tracking with 2-color fluorescent labeling that benefit from the aforementioned features. The application of these single molecule tracking assays *in vivo* remains a far reach and will require other technical advances (in particular with respect to *in vivo* labeling), but the basic concepts shown here *in vitro* should in principle hold *in vivo*.

1.2 A brief history of single particle tracking in confocal microscopy

The idea of tracking the motion of individual particles to shed light on molecular processes has a long history, which can be traced back to at least as early as 1985. In what is certainly one of the first demonstrations of single particle tracking microscopy, Geerts et al. visualized the motion of individual gold nanoparticle captured in an *in vitro* system of purified microtubules and kinesin proteins [15]. They detected saltatory motion that they attributed to the transport of the nanoparticles by the kinesin motors. This paper already contained the essential concept that underlies single particle tracking assays (SPT), namely that the analysis of the trajectories of

individual particles reveals information about the observed system. The challenges associated with automatically and accurately locating the particle, which is still today the subject of active research, were also discussed in this paper.

Since then, single particle tracking and single molecule tracking (the latter referring to the situation where a fluorescent label rather than a tagging particle is used to localize the particle) have been very successfully applied to a variety of biological questions (see [16] for a review). One of the hallmark applications of SPT is perhaps the study of diffusion within phospholipid membranes, which is of great importance to understand protein interactions and signaling across the plasma membrane [17, 18].

In this work, we are focusing on a different paradigm for single molecule tracking, which emerged when strategies were proposed to track individual molecules in a confocal microscope without relying on wide field images. In a seminal paper, Enderlein proposed a localization scheme involving fluorescence modulation by a laser beam steered rapidly along a circular orbit. In that scheme, the particle position is obtained in real time using simple demodulation electronics and is used to drive a feedback loop that keeps the particle in the center of the confocal volume (typically using a piezo stage displacing the sample) [19]. The confocal implementation yields two essential advantages compared to particle tracking in wide field images: 1. It allows the use of efficient and high bandwidth single photon detectors rather than slower CCD cameras, and fast demodulation electronics rather than computer based image processing. This greatly increases the bandwidth of the position detection and the ability to track faster moving particles. 2. Since the feedback system maintains the particle in the focus plane of the microscope, there is no special difficulty associated with localizing the particle in the axial direction. In contrast, camera based tracking typically requires capturing z-stacks at each time point, which reduces the time-resolution of the measurement, or involves more sophisticated imaging systems to encode the axial position of the particle in the frames obtained at a fixed plane (for example, using asymmetric point-spread functions, see [20]).

Implementations of the algorithm proposed by Enderlein were first demonstrated between 2003 and 2005, with feedback-equipped confocal microscopes being successfully built in the group of H. Mabuchi as well as E. Gratton [21, 22, 23]. Using

feedback-based tracking, McHale et al. [21, 22, 23] were able to lock onto quantum dots diffusing as fast as $20\mu\text{m/s}$ (15nm diameter) and detect anti-bunching statistics in their emission [22]. These results nicely illustrated the fact that long observation periods of an individual molecule permits the accumulation of fluorescence statistics which give access to dynamics on very short timescales. While anti-bunching can be measured in conventional FCS, it requires thousands of molecule transits, whereas the same information can be obtained with a single quantum dot in a tracking setting. Exploring what could be seen as the other end of the spectrum (in vivo, slow diffusing objects, vs. in vitro fast diffusing objects), Valeria et al. demonstrated the feasibility of feedback-based tracking for in vivo measurements, and applied it to a measure the motion of a tagged-locus in interphase chromatin [24, 25, 21].

On the theory side, important work has been done by A. Berglund to characterize the optimal control strategies, and the performance limitations of the tracking routine [26, 27].

Despite these early studies and applications, the use of feedback based confocal tracking techniques in biology has so far remained limited. In fact, a Google Scholar search on single molecule tracking mostly returns references pointing to studies using traditional camera based tracking assays that do not involve any feedback. Perhaps a reason for this is that the measurement output that is most often considered in in vivo confocal single molecule tracking experiments, namely the trajectory of the particle, can either be obtained with camera based tracking, or contains information (diffusivity) that is also accessible through other more simple techniques.

For example, in membrane studies, a true 3D tracking method is not necessary because of the two-dimensional geometry of the membrane; in fact, it is more advantageous to monitor multiple molecules at once with TIRF illumination (especially with the development of high bandwidth cameras that permit sub ms integration timescales). In the field of chromatin dynamics, the large bandwidth of single molecule tracking and the automatic z positioning is not required since the motions measured are slow, and time lapsed scanning based imaging have sufficient time resolution [28]. In other cases where full 3D tracking would required, diffusion is typically measured by FCS or Fluorescence Recovery After Photobleaching (FRAP).

1.3 Single molecule tracking is more than recording trajectories, and why FCS

Based on these observations, it is interesting to employ single particle in combination with other more traditional fluorescence based assays in order to augment the information contained in the trajectory, with orthogonal readouts from the fluorescence signal. The central question then becomes how to make effective use of the fluorescence signal.

Many schemes can be thought of, to make use of the ability to maintain a freely diffusing particle in the detection volume of a confocal microscope. For example, tracking a molecule labeled with a FRET pair could provide a very effective way to relate conformational changes happening at two separate length scales: precise local conformation information could be obtained from the FRET signal whereas large scale conformational changes could be measured by monitoring variations in the diffusion coefficient. This approach might be particularly useful for large biological structures that exhibit organization across various length scales. Another simple possible assay could combine tracking with multichannel fluorescence measurement to detect binding and identify correlations between binding events and changes in mobility. Finally fluorescence signals in SMT can be subject to correlation analysis in a manner analogous to the analysis done in conventional fluorescence correlation spectroscopy (FCS) studies.

To my knowledge, only a small number of studies have reported the use of single-molecule feedback tracking in conjunction with classical single molecule fluorescence methods. An interesting study that came from Cardarelli et al., where they used 3D tracking and FCS to measure molecular transport through the nuclear pore complex (NPC)[29]. In that study, 3D tracking was applied to force the FCS beam to continuously track the center of mass of the NPC. This had two advantages: first, the slow ensemble motion of the NPC (as opposed to the motion of the transporters in the frame of the NPC) do not appear in the FCS data anymore, second, it is possible to place the beam at precise location with respect to the NPC, and therefore to distinguish between processes happenings on both side of the membrane. However in that

study, despite the use of tracking, the FCS signal is effectively a conventional FCS signal measuring the average diffusivity of an ensemble of molecules.

The use of fluorescence correlation techniques at the single molecule level and in the context of tracked particles was initially discussed by Enderlein and A. Berglund [23, 30]. These works, however, mostly examined the fluctuation of the same fluorescence signal that is used to localize the particle, and therefore these fluctuations were reflective of the localization error during tracking. The addition of a second excitation wavelength in coordination with two-color labeling rendered the assay much more interesting because the fluorescence fluctuations in the spectral channel not used for tracking relate to intermolecular dynamics. This approach was pioneered by K. McHale as he used two color tracking-FCS to measure and characterize the conformational Brownian dynamics of lambda-phage DNA [31]. This work is to my knowledge the only example of application where single-molecule tracking and FCS were combined to measure intermolecular dynamics.

It is a noteworthy application that clearly illustrates the main features and advantages of the tracking-FCS assay: 1. the fluorescence correlation signals obtained are true single molecule signals, which is evidently in contrast with conventional implementations of FCS where the correlation functions results from an averaging over thousands of molecules. 2. unlike what happens in conventional FCS where the fluctuations mostly originate from the diffusion of random molecules across the beam and therefore center of mass diffusion dominates the correlation signal, center of mass motion is effectively cancelled in tracking-FCS. Therefore, in tracking-FCS, the contribution of the intermolecular motion to fluorescence fluctuations is naturally enhanced.

1.4 Context with respect to previous work in the lab

The work presented in this dissertation diverges from standard applications of single molecule tracking, and extends the idea first introduced in the lambda-DNA study

by K. McHale. Rather than focusing on measuring accurate trajectories of diffusing molecule, we are interested in the information that is contained in the long lasting fluorescence signals obtained from a single molecule. The main difference between this work and the work from K. McHale ([31]) is in the amplitude of the internal motion that I sought to resolve. In the lambda-DNA study, the molecule size (48000bp, radius of gyration $\sim 1\mu\text{m}$) was larger than the probe beam. In this work, I show application of tracking-FCS to the measurement of conformational dynamics of DNA fragments as short as 479bp, which is less than 100nm, and therefore much smaller than the probe beam (which is diffraction limited). The two orders of magnitude difference in size changes the modalities of the experiment and the data analysis. The changes are related to the following three essential facts.

1. The particle localization error during tracking due to finite tracking bandwidth is almost negligible for large molecules, but dominated the correlation signal for small molecules
2. Smaller molecules diffuse faster which amplifies the effects of 1.
3. The exact position of the probe and tracking beam with respect to each other do not matter for large molecules, but strongly alters the signal for small molecules.

Because of the facts 1. and 2., the performance of the tracking apparatus in terms of feedback bandwidth and tracking accuracy becomes an essential limitation to the spatial resolution of the tracking-FCS assay. This led me to modify the tracking microscope instrumentation and to seek to improve its performance. Additionally, because of facts 1 through 3, the interpretation of the tracking-FCS data requires careful consideration of the instrumentation status. Finally, fact 3. Is not just a difficulty but also a source of possible optimization and extensions of the tracking-FCS assay, which are discussed in this thesis.

While the initial motivation for improving the spatial resolution of tracking-FCS resolution was to use the tracking microscope to measure and characterize the dynamics of nucleosome arrays induced by various chromatin binding proteins. I did not get the chance to get to this application by the end of my PhD. The development

of the instrumentation and of the assay turned out to be a large project by itself. I am hoping that the tracking-FCS methods discussed in this work will be used for interesting biological measurements in the near future.

1.5 Thesis organization

This dissertation is organized as follows. Chapter 2 lays out the theoretical foundations for describing fluorescence fluctuations in the context of single molecule tracking with two-color illumination. I discuss the importance of controlling the illumination geometry, and quantify the spatial and temporal resolution of tracking-FCS. One of the main difficulties of tracking-FCS at the experimental level resides in the data processing and analysis. Great care needs to be taken to properly account for the various processes that contribute to the correlation signal, and to extract meaningful information from it. The second part of the first chapter therefore focuses on describing the details of how the raw fluorescence correlation can be processed and converted into position correlation functions that represent the internal dynamics of the molecule. Chapter 3 describes the improvements in the feedback tracking microscope. The instrument uses the same core principles as the initial instrument built previously in the Mabuchi Lab, but uses a different optical design that permits higher tracking bandwidth and more flexible configuration of the beams. I highlight the changes in this chapter. The fourth chapter presents experimental results where tracking-FCS was applied to measure the end-to-end dynamics of short DNA fragments. This application serves as a proof of principle that tracking-FCS can be used to measure the end-to-end dynamics of small molecules well below the diffraction limit. I finally conclude in chapter 5 by discussing the future important improvements in the tracking microscope and the tracking-FCS assay.

Chapter 2

Tracking-FCS: theory and data analysis

In this chapter, we present the theory that describes fluorescence fluctuations in the context of single-molecule tracking-FCS. We consider the assay where individual molecules are labeled with two distinct fluorophores at two distant sites. One site is labeled with a Cy3-like fluorophore and serves as a reference point on the molecule. This site is actively tracked by the microscope feedback circuitry. The other site, or probe site, is labeled with a Cy5-like dye and can freely move with respect to Cy3 upon conformational change of the molecule. This chapter is devoted to quantifying the Cy5 fluorescence fluctuations induced by the conformational dynamics of the molecule.

In the first part of the chapter, we derive general expressions for the fluorescence correlation function, and show how the position of the probe beam with respect to the tracking beam affects the amplitude of the fluorescence fluctuations. We then derive the optimal illumination geometry to detect small distance fluctuations between the probe and reference sites. Finally we discuss the spatial and temporal resolution of the assay. The second part of the chapter is oriented towards data analysis and describes how the experimental fluorescence correlation functions can be processed to provide the correlation function of the distance between the probe and the reference sites.

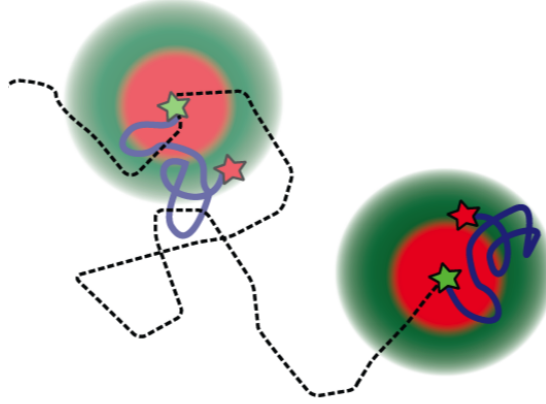


Figure 2.1: Schematic of a tracking-FCS assay. The microscope is configured with two excitation laser beams. A "tracking beam" (561nm wavelength) tracks the overall diffusion of the molecule by following the motion of a Cy3-labeled site. A "probe beam" (635nm wavelength) is aligned to the tracking beam and is actively displaced to match the motion of the tracking beam. In that configuration, the tracking feedback maintains the position of the Cy3-labeled site in the center of the probe beam, whereas the Cy5-labeled site is free to move. Changes in the molecule conformation cause Cy5 fluorescence fluctuations that can be measured and quantified.

2.1 Theory of fluorescence correlation functions in tracking-FCS

2.1.1 General expression of fluorescence correlation functions

In this section, we are deriving the general form of the fluorescence correlation function for a tracked particle. The fluorescence correlation function is commonly defined as

$$g(\tau, t) = \frac{E[I_t I_{t+\tau}] - E[I_t] E[I_{t+\tau}]}{E[I_t] E[I_{t+\tau}]} \quad (2.1)$$

This is the time covariance of the fluorescence signal measured at times t and at a time lag τ later, normalized by the product of the mean intensities at these two times. The expectation value in the definition refers to the ensemble average, which is convenient for doing calculations, but in the real world the correlation function is

computed from experimental data by using a time average instead of an ensemble average.

$$g_{\text{exp}}(\tau) = \frac{\langle I_t I_{t+\tau} \rangle - \langle I_t \rangle^2}{\langle I_t \rangle^2} \quad (2.2)$$

The two definitions are equivalent provided that the intensity process is stationary and ergodic. We will take that as an assumption for the rest of this section. This also means that for the experimental correlation function to be meaningful, the observation time of the molecule needs to be much larger than the longest characteristic time constant of the process. This ensures that the time average converges to the ensemble average. In the stationary case, the autocorrelation is only a function a function of the time lag τ so we can drop the subscript representing the time dependency t and simply write

$$g(\tau) = \frac{E[(I_t - \bar{I})(I_{t+\tau} - \bar{I})]}{\bar{I}^2} = \frac{E[I_t I_{t+\tau}]}{\bar{I}^2} - 1 \quad (2.3)$$

where $\bar{I} = E[I_t]$

There is one situation which gives rise to non stationarity but is useful to consider, and where we can extend the definition above. This is the situation where there is an externally imposed, periodic variation in the illumination conditions. For example, the rotation motion of the tracking laser creates a periodic modulation in the fluorescence signal. A similar situation arises when the laser is periodically switched off, for example if we are alternating excitation at different wavelengths. In that case, we can simply modify the definition of the correlation function (eq. 2.1) by replacing all the expectation values at time t (which are no longer independent of t) by their time average. More specifically we will define for the case with periodic modulation

$$g(\tau) = T \frac{\int_0^T dt E[(I_t - \bar{I})(I_{t+\tau} - \bar{I})]}{\left(\int_0^T dt \bar{I}_t\right)^2} \quad (2.4)$$

where T is the duration of the measurement. With this adapted definition, the experimental correlation function g_{exp} converges towards $g(\tau)$. For this reason, and since the time average can be thought of as an expectation value, we will write the correlation as in 2.3 even in the presence of periodic modulation, but we will bear in

mind the distinction in definition.

Before we start deriving expressions for the fluorescence correlation function in tracking-FCS, let us introduce a few general notation conventions which will be helpful for the rest of the paragraph. Given a real or vector-valued stationary stochastic process X_t , we define the raw (not normalized autocorrelation function) as

$$\chi_X(\tau) = E [X_t X_{t+\tau}^T]$$

Since we are interested in second-order statistics, it is convenient to collect the value of the process at two time points into a single vector

$$\vec{X} = \begin{pmatrix} X_t \\ X_{t+\tau} \end{pmatrix}$$

The vector sign above a quantity will be used to represent two-time points vectors.

Let's start with the 1-dimensional case. Consider the random motion x_t of a fluorescently labeled site inside a laser beam with a gaussian intensity profile. Let's assume this motion is a stationary gaussian process with covariance matrix $\Sigma(\tau)$

$$\Sigma(\tau) = E [\vec{x} \vec{x}^T]$$

and we center the coordinate system such that $E[x_t] = 0$. We write the laser intensity profile

$$\phi(x) = e^{-\frac{2}{w^2}(x-\delta)^2}$$

which is normalized so that the intensity is 1 in the center of the beam. w is the beam waist, and δ is the position of the beam in the frame centered on the particle mean position. We will refer to δ as the beam offset. Assuming for the time being that the dye does not blink (this will be considered thoroughly in the next section), the fluorescence signal is that of a Poissonian emitter with stochastic rate

$$I_t = P\eta\phi(x_t)$$

where η is the quantum yield of the dye and P is the laser power. For such a gaussian process, it is easy to compute the fluorescence correlation function. The probability density for \vec{x} is

$$\rho(\vec{x}) = \frac{1}{\sqrt{(2\pi)^2 \det(\Sigma)}} e^{-\frac{1}{2} \vec{x}^T \Sigma^{-1} \vec{x}}$$

The raw correlation can be calculated as

$$\chi_I(\tau) = \int_{-\infty}^{\infty} \rho(\vec{x}) \eta \phi_0 \exp\left(-\frac{2}{w^2} \vec{x}^T \vec{x}\right) d\vec{x}$$

Before going further, it is useful to convert the variables with units of length into adimensional variables by expressing them in units of beam waist, through the rescaling

$$x \rightarrow \frac{w}{2}x, \quad \delta \rightarrow \frac{w}{2}\delta \quad (2.5)$$

Likewise, since the correlation function is defined so as to be invariant by a rescaling of the average intensity, we can safely normalize all the fluorescence intensities by the maximum intensity $I_0 = I(x = \delta) = \eta P$, which is the fluorescence intensity of the dye in the center of the beam. Doing this, and using the following formula for a multivariate gaussian integral

$$\int_{\mathbb{R}^n} e^{-\frac{1}{2} y^T A y + v^T y} dy = \sqrt{\frac{(2\pi)^{\dim(A)}}{\det(A)}} e^{\frac{1}{2} v^T A^{-1} v} \quad (2.6)$$

we get

$$\chi_I(\tau) = E[I(t)I(t+\tau)] = \frac{1}{\sqrt{\det(\mathbb{I} + \Sigma)}} e^{-\frac{1}{2} \vec{\delta}^T (\mathbb{I} + \Sigma)^{-1} \vec{\delta}}$$

The average intensity is computed in a similar manner. In fact, it is easy to show that the product of the expectations $E[I(t)] E[I(t+\tau)]$ can be obtained directly from χ_I by replacing Σ by

$$\Sigma_{\infty} = \lim_{\tau \rightarrow \infty} \Sigma(\tau) = \begin{pmatrix} E[x_t^2] & 0 \\ 0 & E[x_{t+\tau}^2] \end{pmatrix}$$

Therefore we have

$$E[I(t)] E[I(t + \tau)] = \frac{1}{\sqrt{\det(\mathbb{I} + \Sigma_\infty)}} e^{-\frac{1}{2} \bar{\delta}^T (\mathbb{I} + \Sigma_\infty)^{-1} \bar{\delta}} \quad (2.7)$$

and from there, we obtain the correlation function

$$g(\tau) = -1 + \sqrt{\frac{\det(1 + \Sigma)}{\det(1 + \Sigma_\infty)}} \exp\left(-\frac{1}{2} \bar{\delta}^T ((\mathbb{I} + \Sigma)^{-1} - (\mathbb{I} + \Sigma_\infty)^{-1}) \bar{\delta}\right) \quad (2.8)$$

Equation 2.8 describes the coupling between fluctuations in position, represented by the covariance matrix Σ , and fluctuations in intensity, represented by $g(\tau)$.

Note that at this point the offset δ_t does not need to be constant, and can be any deterministic trajectory, in which case the correlation function is a function of both the time lag τ and the absolute time t . In the case of a constant offset $\delta_t = \delta_0$, the expressions 2.7 and 2.8 can be further simplified by writing Σ explicitly.

The most general form for Σ for a stationary process with zero mean is

$$\Sigma(\tau) = \begin{pmatrix} v & vc(\tau) \\ vh(\tau) & v \end{pmatrix} \quad (2.9)$$

where v is the variance of x_t and $c(\tau)$ is the normalized covariance

$$c(\tau) = \frac{E[x_t x_{t+\tau}]}{v} \quad (2.10)$$

Equation 2.8 then becomes

$$g(\tau) = -1 + A(\tau) \exp\left(\delta_0^2 \frac{c(\tau)v}{(v+1)(c(\tau)v + v+1)}\right) \quad (2.11)$$

where

$$A(\tau) = \sqrt{\frac{1}{1 + \left(\frac{vc(\tau)}{1+v}\right)}} \quad (2.12)$$

And the average normalized intensity yields

$$\bar{I} = \frac{e^{-\frac{1}{2} \frac{\delta_0^2}{v+1}}}{\sqrt{v+1}} \quad (2.13)$$

The 3-dimensional case can be treated similarly. The particle trajectory x_t is now a three dimensional vector. We make the assumption that the laser intensity profile can be well approximated by a 3-dimensional gaussian, with waist w_{xy} in the (xy) plane and w_z along z. This assumption is commonly used in open loop FCS and is valid in tracking-FCS as long as the particle remains in the Raleigh range of the beam. In the case where the dynamics along the three axis are independent, the cross-diagonal blocks in the covariance matrix Σ vanish and we can factorize the expression of the fluorescence correlation function into

$$g_{3D}(\tau) = (-1 + \prod_{i=1}^3 (1 + g_i(\tau))) \quad (2.14)$$

where $g_i(\tau)$ is the correlation function for a single axis computed from eq. (2.8) with $w = w_{xy}$ for $i = 1, 2$ and $w = w_z$ for $i = 3$ (w is indirectly present in eq. (2.8) via the renormalization eq. (2.5))

2.1.2 First experimental test

In order to verify the predictions from equation (2.14), we took tracking-FCS data on immobilized fluorescent microspheres. When tracking is turned on to lock onto an immobilized particle, the localization noise gives rise to a residual "jittering" of the stage position which is well described by an Ornstein Uhlenbeck process (O.U.) the variance of which can be directly measured from the stage position sensors. This is therefore a straightforward way to generate an O.U. process with well defined parameters. We varied the offset between probe beam and tracking center by applying a bias voltage on the VCOs that control the tracking beam motion, and recorded tracking-FCS data for each offset value. Fig. 2.2 shows the experimental data for 6 different values of offset ranging from $\delta = 0$ to 2.0 (normalized units), along with the

predicted tracking-FCS from eq. (2.14). Data agree well with the predictions. Note that for fluorescent microspheres the signal to noise is very large and therefore the optimal offset should be much larger than 1.

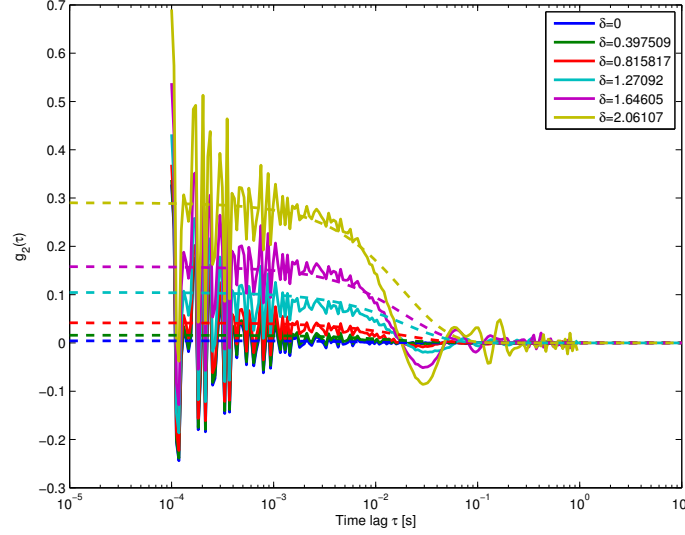


Figure 2.2: Experimental tracking-FCS data on immobilized beads for different values of offset δ and comparison with experimental prediction. The localization noise was measured from the stage trajectory at $\sqrt{v} = 0.27$. The beam waist size was near diffraction limit $w_0 = 305\text{nm}$

2.1.3 Effects of background and tracking error

Two important things need to be taken into account to properly interpret tracking-FCS data: the presence of background and the finite bandwidth of the tracking feedback, which generate a residual tracking error in the position of the particle with respect to the probe beam. This section analyzes these contributions.

Algebraic rules for correlation functions

We first derive a few rules to compute correlation functions of sum and products of stochastic process. These rules will make it easy to take into account background, dye blinking, and laser dynamics. Consider two stationary stochastic processes A_t

and B_t . We use the notation $g_{A,B}$ to refer to the cross correlation function between the processes A_t and B_t , and we write \bar{A} and \bar{B} the mean of A and B respectively

$$g_{A,B}(\tau) = \frac{E[A(t)B(t+\tau)]}{\bar{A}\bar{B}} - 1 \quad (2.15)$$

For the autocorrelation of the process A_t , we will write g_A as a shorthand for $g_{A,A}$. We list a few algebraic rules that will be useful to compute correlation function involving several processes in the next sections.

- Sum of processes. Let $A_{1,t}$ and $A_{2,t}$ be two processes, not necessarily independents. The correlation function of the sum $A_{1,t} + A_{2,t}$ is

$$g_{A_1+A_2} = \frac{\bar{A}_1^2}{(\bar{A}_1 + \bar{A}_2)^2} g_{A_1} + \frac{\bar{A}_2^2}{(\bar{A}_1 + \bar{A}_2)^2} g_{A_2} + 2 \frac{\bar{A}_1 \bar{A}_2}{(\bar{A}_1 + \bar{A}_2)^2} g_{A_1, A_2} \quad (2.16)$$

- Product of independent processes. The cross-correlation function of the products $A_{1,t}A_{2,t}$ and $B_{1,t}B_{2,t}$ is

$$g_{A_1 A_2, B_1 B_2} = (1 + g_{A_1, B_1})(1 + g_{A_2, B_2}) - 1 \quad (2.17)$$

- Product of a stochastic process with a periodic signal. $S_{1,t}$ and $S_{2,t}$ are two periodic signals. The previous rule applies, provided that the expectation value in the correlations involving the periodic signal is replaced by a time average

$$g_{S_1 A_1, S_2 A_2} = (1 + g_{A,B}) \left(1 + \frac{\langle S_1(t) S_2(t+\tau) \rangle}{\langle S_1 \rangle \langle S_2 \rangle} \right) - 1 \quad (2.18)$$

Effect of finite background

The collected photon stream from which the correlation function is computed always contains some contribution from "background" photons, which originate from the auto-fluorescence of the sample and the optics, and from the dark counts of the detector. Taking proper account of the background photons is important in tracking-FCS, as the amplitude of the tracking-FCS signal is reduced with increasing background and

this could be misinterpreted as a smaller amplitude of motion. The detector dark counts are usually negligible compared to the sample autofluorescence, and therefore the background emission rate is proportional to the beam intensity. The total measured fluorescence rate can be expressed in the form

$$I_{\text{meas}} = I_{\text{signal}} + I_{\text{background}} = (\Phi(x) + k) \quad (2.19)$$

where k represents the number of "background" photons per number of "signal" photons coming from the fluorescent particle, when the particle is located in the center of the illumination beam at $x = \delta$ where $\Phi(\delta) = 1$. We will refer to k as the background level. Note that the background level k is defined so that it is only a function of intrinsic parameters of the system and the instrument (quantum yield of the dye, autofluorescence of the buffer, beam waist), but does not depend on the dynamics of the particle or on the beam location. The signal to noise on the other hand is a function of the beam location x_0 and of the variance of the particle internal motion. Using the algebraic rules for correlation functions and expression (2.19), we can compute the measured correlation function in presence of background

$$g_{\text{meas}}(\tau) = \left(\frac{\bar{I}_{\text{signal}}}{\bar{I}_{\text{signal}} + \bar{I}_{\text{background}}} \right)^2 g_{\text{signal}} = \frac{g_{\text{signal}}(\tau)}{\Theta} \quad (2.20)$$

where we have defined

$$\Theta = (1 + k/E[\Phi(x_t)])^2 \quad (2.21)$$

The effect of background is to scale down the correlation function by a factor Θ uniformly across all time lags.

Effect of tracking error

In any experimental implementation, the bandwidth of the feedback loop is finite. The limitation stems from either the bandwidth of the actuators, or if the actuators are fast, from the finite fluorescence rate. Tracking bandwidth is discussed in more details in chapter 2. Because of the bandwidth limitation, the particle can never be perfectly tracked, and there is a residual jittering in the position of the reference site

with respect to the probe beam. This residual jittering contributes to the fluorescence fluctuations in a way similar to the end-to-end motion. In fact, the typical localization error for a particle diffusing around $10\mu m^2 s^{-1}$ and labeled with a single dye for tracking, is on the order of $100nm$ (localization error is discussed in chapter 3). This means that for internal motion smaller than $100nm$, which is the regime of spatial sensitivity we are interested in, the tracking error dominates the fluorescence fluctuation signal. The presence of tracking error is straightforward to take into account as we simply need to replace x_t with

$$x_t = x_{im,t} + x_{err,t} \quad (2.22)$$

where $x_{im,t}$ represents the true end-end to vector joining the reference and the probe dye, and $x_{err,t}$ is the position of the probe dye with respect to the tracking center and accounts for the tracking error. Since the molecular dynamics and the tracking error are independent, the covariance matrix becomes

$$\Sigma(\tau) = \Sigma_{im}(\tau) + \Sigma_{err}(\tau) \quad (2.23)$$

and the correlation function is now

$$g(\tau) = -1 + \sqrt{\frac{\det(1 + \Sigma_{im} + \Sigma_{err})}{\det(1 + \Sigma_{im,\infty} + \Sigma_{err,\infty})}} \exp\left(-\frac{1}{2}\bar{\delta}^T ((\mathbb{I} + \Sigma_{im} + \Sigma_{err})^{-1} - (\mathbb{I} + \Sigma_{im,\infty} + \Sigma_{err,\infty})^{-1}) \bar{\delta}\right) \quad (2.24)$$

Note that the contributions from the tracking error and the end-to-end motion do not factorize, and we cannot write the correlation function as a product of an internal dynamics part and a tracking error part.

2.1.4 Tracking-FCS in a steep intensity profile: optimization of illumination conditions

One great advantage of using feedback in a FCS assay is that the molecule can be maintained in a well defined position within the illumination volume. The localization accuracy is sub-diffraction limit, which implies that the fluorescence correlation signal is essentially determined by the local geometry of the beam intensity. This makes it possible to tune the sensitivity of the measurement by changing the intensity gradient at the tracking center, without worrying about the overall shape of beam. This contrasts with a traditional FCS setting where via Brownian diffusion, the molecule stochastically explore various parts of the beam, and the entire illumination pattern contributes to the fluorescence correlation signal. It is in particular intuitively clear that in tracking-FCS, the relative position of the probe beam with respect to the tracking center strongly affects the amplitude of the fluorescence fluctuations generated by the end-to-end motion of the molecule (fig. 2.3).

Simulations

Fig 2.3 is a simulation study that illustrates this. We first consider the case of a perfectly tracked molecule: the reference site is perfectly maintained at the tracking center, whereas the probe site is free move as the molecule changes conformation. We simulated a toy model where the end-to-end dynamics of the molecule is governed by an isotropic Ornstein-Uhlenbeck process with a characteristic timescale $\tau_{\text{im}} = 1\text{ms}$. To mimic molecules of various sizes, we varied the amplitude of the end-to-end motion by setting the standard deviation along each axis to $\sigma_{\text{im}} = 0, 10\text{nm}, 20\text{nm}, 50\text{nm}$. For this model, the covariance of the end-to-end vector is a monoexponential relaxation $E[x_t x_{t+\tau}] = E[y_t y_{t+\tau}] = E[z_t z_{t+\tau}] = \sigma_{\text{im}}^2 e^{-t/\tau_{\text{im}}}$. The beam was near diffraction limit with a waist size of $w = 350\text{nm}$. For each amplitude of motion, 3 random trajectories of 10 seconds were simulated. Since the amplitude of motion is much smaller than the beam Raleigh range, we ignored the motion along the z-axis and simulated motion in the x,y plane only. For each trajectory, we then simulated a Poisson process with time varying rate given by $I_t = \Phi(x_t)\Phi(y_t) + k$, and computed the fluorescence correlation

function g . The average fluorescence rate from the dye was 50kPhotons/s for all the simulations, so that the total number of photons received from the dye was about $1e6$. This is a reasonable number that can be obtained with a single organic fluorophore provided careful tuning of the oxygen scavenger system. Finally, we use a background level of $k = 0.2$, which is typical in our experiments. Simulation was repeated for two positions of the beam: $\delta = 0$ corresponding to a centered-illumination (tracking center centered on probe beam), and $\delta = 1$, corresponding to a side-illumination with the tracking center positioned at the point of steepest gradient of the gaussian profile of the probe.

Clearly, the side-illumination geometry improves the ability to resolve the end-to-end dynamics for short molecules. 10nm, 20nm, and 50nm motion are all separated from each other and resolved above the background ($\sigma = 0$). In the centered-illumination geometry however, only the 50nm motion is clearly distinguishable away from background. Note that the theoretical form of the correlation function obtained from eq. (2.14) matches very well the simulated data.

We then repeated the simulation in presence of tracking error. $x_{\text{err},t}$ is modeled as an Ornstein-Uhlenbeck process independent from $x_{\text{im},t}$ (characteristic timescale $\tau_{\text{err}} = 1ms$, which corresponds to a tracking bandwidth of 1kHz, and $\text{std}(x_{\text{err},t}) = \sigma_{\text{err}} = 100nm$.) Similar to the tracking-error free case, the side-illumination geometry allows better resolution of the internal motion above the measurement noise floor (black curves, tracking error only, $\sigma_{\text{im}} = 0$). However, tracking-error clearly impedes our ability to measure the internal dynamics when the amplitude of motion is below 50nm.

With this observation, a natural question to ask is what is the optimal positioning of the probe beam that provides best spatial resolution, and how does this optimal position depend on the tracking-error and the background level. These questions are addressed in the next section.

Optimal positioning of the probe beam

The sensitivity of the tracking-FCS signal relates to the strength of the coupling between fluctuations in space (end-to-end motion) and fluctuations in fluorescence.

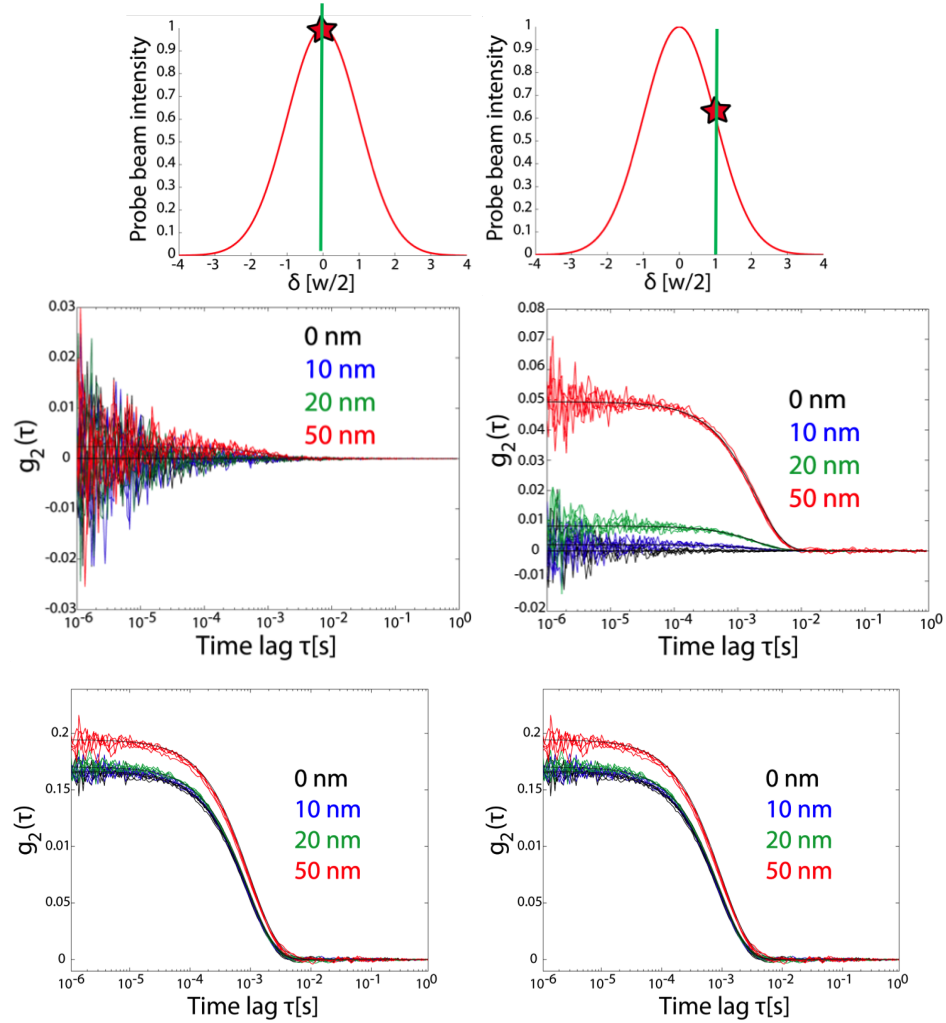


Figure 2.3: Top left. Schematic of the centered illumination geometry: probe beam (intensity along x axis shown in red) is centered with respect to the tracking center (position of tracking center along x axis shown in green). Star represents average position of the probe dye. In this illumination condition, small displacements of the probe dye lead to small fluctuations in intensity. Top right. Schematic of the side illumination geometry: probe beam is offset with respect to the tracking-center. The probe is on average located at a point of steep intensity gradient, resulting in larger fluorescence fluctuations. Middle and bottom rows. Fluorescence correlation functions $g(\tau)$ for a simulated relaxation with timescale $\tau_c = 1000\text{ms}$ and for several amplitudes of motion σ_{im} (black: 0nm, blue: 10nm, green=20nm, red=50nm). Middle Left and right are centered and side illumination ($\delta = 0$ and $\delta = 1$ respectively) in absence of tracking error. Bottom left and right are centered and side illumination in presence of 100nm tracking error.

Consider small motions in 1 dimension (motion amplitude much smaller than the beam size) and in absence of tracking error. In that case, we can do a first order expansion of the intensity profile and replace $I(x)$ with $I(x) \approx I(x=0) + (\nabla_x I)^T \cdot x$ in the expression (2.1). We obtain

$$g(\tau) \approx SE [x_{\text{im},t} x_{\text{im},t+\tau}] \quad (2.25)$$

where we have introduced the sensitivity S

$$S = \left(\frac{\|\nabla_x\|}{I_0} \right)^2 = \frac{\partial g(0)}{\partial v_{\text{im}}} \quad (2.26)$$

which is also the derivative of the fluorescence correlation function amplitude $g(0)$ with respect to the variance of the intermolecular motion v_{im} . The fluorescence correlation function is proportional to the autocorrelation of the end-to-end trajectory with a proportionality factor that is equal to the square of the relative intensity gradient. This is conform to the intuition that to obtain a large value of g for a given amplitude of motion, we need a large local intensity gradient.

However, since g quantifies the relative fluorescence fluctuations, it is the relative intensity gradient that matters rather than the gradient itself. For this reason, the point of steepest gradient is not the optimal position for the tracking center. Fig 2.4 shows the sensitivity as a function of the beam position δ and for different background levels. In the extreme case where there is an absence of background ($k = 0$), the sensitivity is maximized for $\delta \rightarrow \infty$. In that case, it is advantageous to maintain the molecule as far as possible in the tail of the probe beam since the loss of intensity can be compensated for by an increase in laser power without increasing the noise, and since the relative gradient grows as the distance to the center of the beam. For a non-zero background, the signal-to-noise degrades as the offset increases, which trades off for the increased gradient, and there is a finite value of the offset that maximizes the sensitivity. Note that the optimal value of δ is always larger than 1, which corresponds to the point of steepest gradient of the beam profile. The point of steepest gradient is only optimal in the limit $k \rightarrow \infty$.

In the presence of the tracking error, the sensitivity can be calculated by doing a Taylor expansion directly on the expression of the correlation function with respect to v_{im} . The analytical expression is easy to obtain and not interesting by itself, but we plot S in presence of 100nm tracking error in fig. 2.4 (blue lines). Here again, there is for any given background level an optimal position of the beam which maximizes the sensitivity, and that is shifted towards larger δ compared to the perfect tracking case. Note that for non-optimal small values of the offset, the presence of tracking error increases the sensitivity. This is because the tracking error naturally displaces the molecule away from the beam center towards side regions where the relative intensity gradient is larger. Inversely, when the beam position is chosen optimally, tracking error degrades the sensitivity by inducing a residual motion of the molecule in the frame bound to the tracking center. This is equivalent to randomly moving the probe beam away from its optimal position, which is where the point of largest relative intensity gradient coincides with the tracking center. Because of tracking-error, the molecule gets exposed to regions of shallower intensity profile where the coupling between position and fluorescence is weaker.

Resolving small differences in size between large molecules

In the section above, we computed the sensitivity to the detection of small internal dynamics by doing a Taylor expansion of the correlation function amplitude at the point $v = v_{\text{err}}$. This approach applies identically to the case where we are interested in resolving differences in end-to-end motion between large molecules that have an internal dynamics with an amplitude comparable to the amplitude of the tracking error. In that case, the Taylor expansion should be carried near the point $v_{\text{err}} + v_{\text{im},0}$ where $v_{\text{im},0}$ is the average value of the range of internal dynamics motion we seek to resolve. All the results derived in this chapter apply to that situation provided that we replace v_{err} by $v_{\text{err}} + v_{\text{im},0}$.

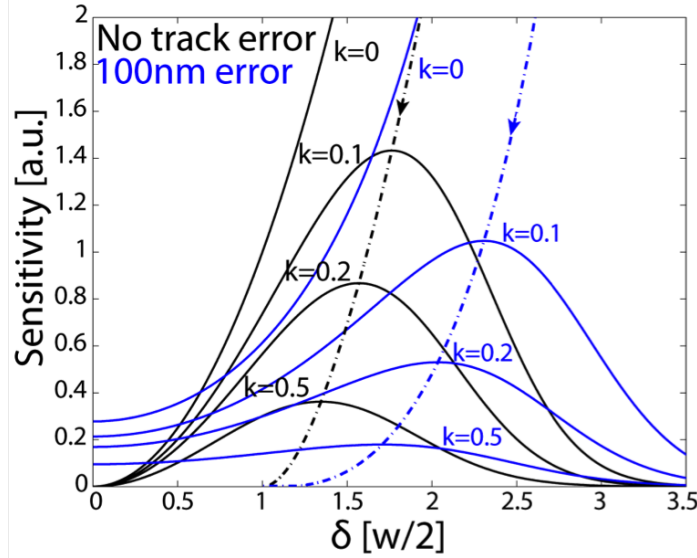


Figure 2.4: Sensitivity of the correlation function to the probe motion as function of the probe offset δ with respect to the tracking center, in absence of tracking-error (black curves), and in presence of 100nm tracking error (blue curves). For both cases, each curve corresponds to a given background level (0,0.1,0.2,0.5). Typical background level for single dye labeling in buffer conditions with oxygen scavenger is between 0.1 and 0.3. Dotted lines are optimal offset as a function of background level. For every point in the parameter space $[k, v_{\text{err}}]$ there exist an optimal offset δ_{opt} that maximizes the sensitivity

Optimal choice of beam waist

The analysis above was carried in adimensional units, where all the spatial dimensions have been normalized w.r.t. to the beam half waist $w/2$. The effect of tracking error can be attenuated by increasing the beam size, which effectively reduces v_{err} when expressed in normalized units as above. However, increasing beam size also decreases v_{im} and increases the noise level k . This trade-off leads to an optimal value for the beam waist that can be calculated by expressing all the quantities in spatial units, and optimizing the sensitivity with respect to w . Only in the case where tracking error is large ($> 100\text{nm}$) or for large molecules does it become advantageous to increase beam waist above diffraction limit.

2.2 Optimal performance of tracking-FCS and resolution

In this section, we are interested in calculating the spatial and temporal resolution of tracking-FCS. In other words, what is the smallest internal motion that can be resolved from a tracking-FCS signal given that the motion happens at a given timescale?

2.2.1 Noise on the correlation function

Motivation

To address the question above, we first need to know the effect of noise on the correlation function. We aim to derive a simple analytical expression for the variance $\text{var}(g(\tau))$ which is valid independently of the stochastic process that drives the fluctuations in the fluorescence rate I_t . Noise in fluorescence correlation functions has been studied in several papers [32, 33, 34, 35] in the context of traditional FCS. However, rigorous quantification of the noise is rarely carried in FCS studies because it is in general possible to acquire data for large enough periods, such that the counting noise becomes essentially negligible on the timescales of interest. Counting noise is usually not the dominant difficulty in the interpretation of FCS data, but it is rather the selection of a proper model to fit the data and the large number of parameters that need to be inferred. We argue that a thorough understanding of the noise in tracking-FCS is more critical because we are working in the single molecule regime, where the number of photons is limited by photobleaching. Invariably, the tracking-FCS traces for individual molecules are noisier than their ensemble-average counterparts in open-loop FCS. Moreover, characterization of the noise on individual tracking-FCS traces is highly relevant in the context of heterogeneous samples where we cannot resort to averaging across multiple molecules to obtain error bars on the parameters inferred from the data. It may allow for example to distinguish between presence of multiple species and low quality data. For these reasons, we revisit the analysis of the noise on the fluorescence correlation function. Additionally, we propose a different approach compared to previous works, which uses ideas from stochastic integrals over counting

processes. Our derivation is somewhat heuristic, as we do not rigorously introduce the required stochastic calculus framework (which would be beyond the scope of this section).

Estimator for g

The noise on the correlation function is dependent on the estimator used for g , which we need to discuss first. The definition of the correlation function involves instantaneous rates I_t which are not measured in practice. The only information we have access to is the arrival time of each photon recorded by a Time Interval Analyzer board. Equivalently, we have access to the counting process N_t which describes the total number of photons collected up to time t . We use the estimator introduced by Laurence et al. to compute the raw intensity correlation χ_I function from the photon counting process [36].

$$\hat{\chi}_I(\tau) = \frac{\epsilon}{(T - \tau)} \sum_{k=1}^{N(T)} N(t_k + \tau + \epsilon) - N(t_k + \tau) \quad (2.27)$$

where $N(T)$ is the total number of photons (T is the total observation time), t_k is the arrival time of the k^{th} photon, and ϵ is a small binning time. The sum in eq. (2.27) simply counts the number of pairs of photons separated by τ with a tolerance ϵ on the exact time lag. This estimator has the advantage to scale linearly with the number of photons (rather than quadratically). We can first use a heuristic reasoning to convince ourselves that this expression approximates the true intensity correlation. Replacing in the expression of χ (eq. (2.27)) the true rates $I(t)$ and $I(t + \tau)$ by the estimated rates $\frac{N(t+\epsilon)-N(t)}{\epsilon}$ and $\frac{N(t+\tau+\epsilon)-N(t+\tau)}{\epsilon}$, and approximating the integral by a Riemannian sum over the intervals $[k\epsilon, (k+1)\epsilon]$, $k = 0..n = T/\epsilon$, we obtain

$$\chi_I(\tau) \approx \frac{\epsilon}{(T - \tau)} \sum_{k=1}^n \frac{N(k\epsilon + \epsilon) - N(k\epsilon)}{\epsilon} \frac{N(k\epsilon + \tau + \epsilon) - N(k\epsilon + \tau)}{\epsilon} \quad (2.28)$$

For ϵ small enough, each interval contains either 0 or 1 photon, and we can rewrite the sum in expr (2.28). as the sum over all the non-empty bins or equivalently as the

sum over all the photons

$$\chi_I(\tau) \approx \frac{\epsilon}{(T - \tau)} \sum_{k=1}^{N(T)} \frac{1}{\epsilon} \frac{N(i_k \epsilon + \tau + \epsilon) - N(i_k \epsilon + \tau)}{\epsilon} \quad (2.29)$$

where i_k is the index of the binning window that contains the k^{th} photon. This expression is equal to the proposed estimator modulo a redefinition of the initial partition $[k\epsilon, (k+1)\epsilon], k = 0..n = T/\epsilon$ such that $i_k \epsilon = t_k$.

Expectation value and variance of the estimator

$N(t)$ is a non homogeneous (time varying) poisson counting process with rate $I(t)$ that is itself a stochastic process. To calculate expectation values, we condition on the underlying rate $I(0;T)$ (the whole history, for $t=0$ to T). Conditional expectation over the rate will be denoted $E_{|I}$. For the conditioned counting process, we have the relations

$$E_{|I} [N(t_k + \tau + \epsilon) - N(t_k + \tau) | I_{t=0,T}] = I(t_k) \epsilon$$

and

$$\text{var} [N(t_k + \tau + \epsilon) - N(t_k + \tau) | I_{t=0,T}] = I(t_k) \epsilon + (I(t_k) \epsilon)^2$$

which result directly from the properties of a Poisson process and are valid ϵ sufficiently small. Our approach for computing the expectation and variance of the estimator $\hat{\chi}$ relies on rewriting the expression (2.27) as a stochastic integral over the process N_t .

$$\hat{\chi}_I(\tau) = \frac{1}{\epsilon(T - \tau)} \int_{\tau}^T \Delta N_{s-\tau} dN_s \quad (2.30)$$

The standard approach in stochastic calculus is to write N_t as

$$N_t = M_t + \int_0^t I(s) ds \quad (2.31)$$

and we have the property that M_t is a martingale w.r.t. the natural filtration of the

process N . We next use the result that the two processes

$$\int_{\tau}^t \Delta N_{t-\tau} dN_s - \int_{\tau}^t \Delta N_{t-\tau} I(s) ds \quad (2.32)$$

and

$$\left(\int_{\tau}^t \Delta N_{t-\tau} dN_s - \int_{\tau}^t \Delta N_{t-\tau} I(s) ds \right)^2 - \int_{\tau}^t \Delta N_{t-\tau}^2 I(s) ds \quad (2.33)$$

are also martingales [37]. Taking the expectation value of the first martingale (eq. (2.32)), we obtain

$$E_I[\hat{\chi}_I(\tau)] = \frac{1}{\Sigma(t-\tau)} \int_{\tau}^t E_I[\Delta N_{t-\tau}] I(s) ds = \frac{1}{t-\tau} \int_{\tau}^t I(t-\tau) I(s) ds$$

Therefore, now taking the expectation over the rate process I , we get

$$E[\hat{\chi}_I(\tau)] = E[E_I[\hat{\chi}_I(\tau)]] = E[I(t-\tau)I(s)]$$

which shows that our estimator $\hat{\chi}_I(\tau)$ indeed computes the correlation function $\chi(\tau)$.

To compute the variance, we use the fact that the process defined in eq. (2.33) is also a martingale. Therefore

$$\begin{aligned} E_I[\hat{\chi}_I^2(\tau)] &= \frac{1}{\epsilon^2(T-\tau)^2} \left(\int_{\tau}^T E_I[\Delta N_{s-\tau}^2] I(s) ds \right. \\ &\quad + E_I \left[\left(\int_{\tau}^T \Delta N_{s-\tau} I(s) ds \right)^2 \right] \\ &\quad \left. + E_I \left[2 \int_{\tau}^T \Delta N_{s-\tau} dM_s \int_{\tau}^T \Delta N_{s-\tau} I(s) ds \right] \right) \quad (2.34) \end{aligned}$$

The third term in the sum is zero. The second term is

$$\begin{aligned} E_I \left[\left(\int_{\tau}^T \Delta N_{s-\tau} I(s) ds \right)^2 \right] &= \int_{\tau}^T ds \int_{\tau}^T ds' E_I[\Delta N_{s-\tau} \Delta N_{s'-\tau}] I(s) I(s') \\ &= \epsilon^2 \int_{\tau}^T ds \int_{\tau}^T ds' I(s-\tau) I(s'-\tau) I(s) I(s') \end{aligned}$$

and finally the first term is

$$\int_{\tau}^T E_I [\Delta N_{s-\tau}^2] I(s) ds = \int_{\tau}^T (\epsilon I(s-\tau) + \epsilon^2 I(s-\tau)^2) I(s) ds$$

Putting everything together we finally obtain

$$\begin{aligned} E_I [\hat{\chi}_I^2(\tau)] &= \frac{1}{T-\tau} \frac{1}{\epsilon} E[I(s-\tau)I(s)] \\ &\quad + \frac{1}{T-\tau} E[I(s-\tau)^2 I(s)] \\ &\quad + \frac{1}{(T-\tau)^2} \int_{\tau}^T ds \int_{\tau}^T ds' E[I(s-\tau)I(s)I(s'-\tau)I(s')] \end{aligned} \quad (2.35)$$

For ϵ small the first term dominates, and therefore we obtain

$$\text{var} [\hat{\chi}_I(\tau)] = \frac{1}{\epsilon(T-\tau)} \bar{I}^2 (1 + g_{\text{meas}}(\tau)) \quad (2.36)$$

We finally obtain the following expression for the variance on g , which is valid in the limit of $\epsilon\tau$ small, and is therefore asymptotically valid for short time lags.

$$\text{var} [g_{\text{meas}}] = \frac{1}{N\bar{I}\epsilon\tau} (1 + g_{\text{meas}}(\tau)) \quad (2.37)$$

where \bar{I} is the average fluorescence rate and N is the total number of photons. This is the variance on the measured correlation function, and the expression applies independently of the presence of background and for any form of correlation function, as long as the time lag is small enough can be neglected. Not too surprisingly, the variance of the correlation function scales as the inverse of the number of photons.

In practice, we are interested in the noise on the background corrected correlation function g_{signal} , rather than on the raw measured correlation function g_{meas} . Additionally, it makes sense to express the noise in terms of photons from the dye only Nd (rather than the total number of photon N which also includes N_b background photons), since the dye is what is setting our photon budget. The number of photons

emitted by the background and the dye can be expressed respectively in the form

$$N_b = TI_0k$$

$$N_d = TI_0\bar{\Phi}$$

where I_0 is the the fluorescence rate from the dye located in the center of the beam (which is only a function of the laser power) Using the expressions above as well as expressions (2.37) and (2.1) we obtain

$$\text{var} [g_{\text{signal}}(\tau)] = \frac{1}{N_d I_0 \tau \epsilon} (\Theta + g_{\text{signal}}) \quad (2.38)$$

2.2.2 Optimal performance of tracking-FCS and spatio-temporal resolution

Suppose we are trying to extract some information on the internal dynamics $x_{\text{im}}(t)$ of a tracked molecule from the measurement of the background corrected correlation function $g_{\text{signal}}(\tau)$. Without averaging over multiple molecules, we will be able to obtain meaningful information at timescale τ provided that the value of $g_{\text{im}}(\tau)$ is separated from the value that would have been measured in absence of internal dynamics ($x_{\text{im}} = 0$), by at least one standard deviation of the noise. In absence of internal dynamics, the correlation function is the one generated by the tracking error which we denote $g_{\text{signal,im}=0}(\tau)$. This yields the following condition

$$|g_{\text{signal}}(\tau) - g_{\text{signal,im}=0}(\tau)| > (\text{var}(g_{\text{signal}}(\tau)) + \text{var}(g_{\text{signal,im}=0}(\tau)))^{1/2}$$

Denoting g the background corrected correlation function, and keeping track explicitly of the dependency in the covariance matrix, we obtain the following condition for the internal dynamics to be resolved

$$|g_{\text{eff}}(\tau)| > \frac{1}{\sqrt{N_d I_0 \tau \epsilon}} \quad (2.39)$$

where we have defined the effective correlation function g_{eff}

$$g_{\text{eff}}(\tau) = \frac{g(\tau, \Sigma_{\text{im}} + \Sigma_{\text{err}}) - g(\tau, \Sigma_{\text{err}})}{((\Theta + g(\tau, \Sigma_{\text{im}} + \Sigma_{\text{err}}))^2 + (\Theta + g(\tau, \Sigma_{\text{err}}))^2)^{1/2}} \quad (2.40)$$

which quantifies the strength of the internal dynamics signal in the correlation function, by normalizing it with respect to the noise standard deviation. The term on the right side of the inequality is left out of the definition of the effective correlation as it is only a function of the photon budget N_d , the maximal fluorescence rate I_0 , and the timescale τ , which are all parameters that are independent of the dynamics and illumination geometry.

It is clear from expression (2.40) that the presence of finite background reduces the spatial resolution, as the effective correlation is a strictly decreasing function of Θ .

While it is possible to use this expression to calculate the resolution at any timelag, in practice we are often interested in looking at the amplitude of the effective correlation for time lags shorter than the characteristic timescales of the internal dynamics and where $g_{\text{eff}}(\tau)$ has essentially converged to its zero-lag value $g_{\text{eff}}(0)$. Additionally, the effective correlation amplitude is sufficient to discuss the effects of signal to noise and beam configuration on the resolution. Fig 2.5 shows the resolution curves obtained by solving eq. (2.39) given a photon budget of $N_d = 10^6$, which is what can be typically obtained from a single dye before bleaching, and a maximum fluorescence intensity of $I_0 = 50\text{kPhotons/s}$. $\epsilon = 0.1$ as discussed earlier.

The values reported on these resolution curves correspond to the standard deviation of the smallest resolvable internal dynamics $\sigma_{\text{id,min}}$ projected along the axis of beam offset. For isotropic dynamics, we are usually interested in measuring the square root of the mean square end-to-end three dimensional distance, which is directly related to the radius of gyration, and is 3 times the mean square of the projection of the end-to-end distance along one axis. Therefore, the smallest resolvable end-to-end standard deviation in 3-dimensions is $\sigma_{\text{id,min,3D}} = \sqrt{3}\sigma_{\text{id,min}}$.

Similar to what we observed for the sensitivity, there is for every point in the parameter space (k, v_{err}) an optimal beam position δ_{opt} that maximizes the spatial

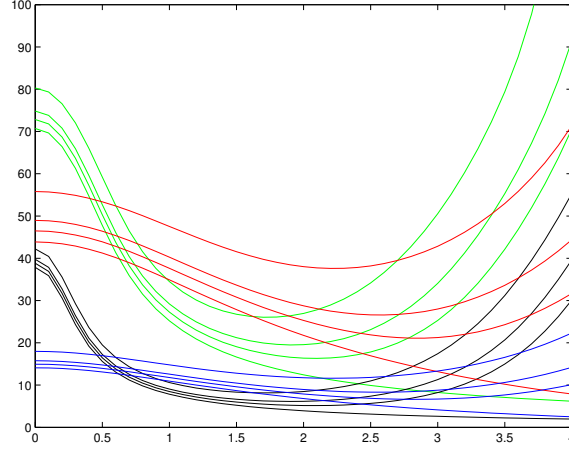


Figure 2.5: Spatial resolution $\sigma_{im,min}$ function of beam offset δ at timescales $\tau = 1\mu s$ (green and red) and $\tau = 100\mu s$ (black and blue) for various noise levels ($k = 0, 0.1, 0.2, 0.5$) and in presence of tracking error (blue and red, $\sigma_{err} = 100nm$) or with perfect tracking (black and green)

resolution and this optimal position always corresponds to having the tracking center beyond the point of steepest gradient of the gaussian probe beam ($\delta_{opt} > 1$ fig. 2.5). However the resolution is only weakly dependent on the exact value of δ , especially in presence of tracking error and background. This suggests that in practice, it should be sufficient to choose a fixed offset value around $\delta = 1.5$ to obtain near optimal resolution independently of the exact background level and tracking error (fig 2.6).

From this analysis, we expect to be able to achieve better than 40nm spatial resolution for end-to-end distance fluctuations occurring on the μs timescale, and 20nm for fluctuations occurring on the $100\mu s$ timescale, even in presence of 100nm tracking error and with a relatively strong background level $k = 0.2$. Importantly, these values are for a single shot measurement on an individual molecule labeled with a single probe dye, assuming emission of 10^6 photons over the course of a 20s tracking. These are reasonable parameters for in vitro conditions where anti-blinking reagents can be added. For molecules labeled with far red dyes organic dyes such as Atto647N or Alexa647, we typically observe emission traces that exceed 10^6 photon before photobleaching.

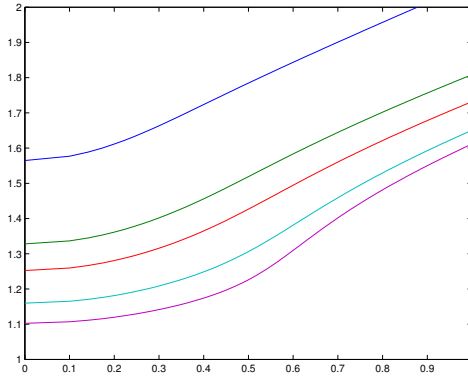


Figure 2.6: Left. Optimal beam position δ to achieve maximum resolution, as a function of tracking error σ_{err} and for various background levels $k = 0.01, 0.1, 0.2, 0.5$.

2.3 Deconvolution of fluorescence correlation functions and dye-blinking free signals

2.3.1 The convolution problem in FCS

The discussion in this chapter has focused so far on the fluorescence fluctuations generated by the random motion of the probe dye within the illumination volume. In reality, the fluorescence fluctuations also originate from the photophysics of the dye itself, which exhibit triplet-state and in some cases stereoisomerization transitions associated with blinking and changes in brightness. These processes contribute to the fluorescence correlation function and complicate its interpretation, especially when the timescales associated with the dye blinking dynamics and the timescales of interest (diffusion timescale in open-loop FCS, internal end-to-end motion in tracking-FCS) overlap. Another difficulty is that the blinking properties of the dye are strongly dependent on the local environment, and are affected by the buffer composition, pH, as well by its interactions with the molecule it is attached to. It is therefore difficult to predict the blinking dynamics for a given system. Typically, the analysis of conventional FCS data requires an explicit model for all the processes giving rise to fluorescence fluctuations (diffusion, dye blinking and in some cases molecular reactions

or conformational dynamics), to obtain an analytical expression for the correlation function which can then be fitted to the data to obtain values for the model parameters (diffusion coefficient, reaction rates, dye transition rates k_{on} , k_{off} ,...). Inclusion of the dye dynamics in the model therefore requires inferring additional parameters which may increase error bars on the estimate of the parameters of interest.

The contribution of the dye photophysics to the correlation function relates to a more general difficulty associated with fluorescence correlation spectroscopy. FCS is fundamentally a one-dimensional measurement (the signal consists of a single stream of photons), but multiple independent physical processes contribute to the signal that eventually need to be deconvolved if we wish to quantitatively interpret the data. The deconvolution step is traditionally done through modeling and fitting, which for the reasons discussed above is not an ideal method.

In tracking-FCS, we can circumvent this problem and naturally deconvolve the contribution of various processes by taking advantage of the fact that the tracking feedback maintains the molecule in a controlled position with respect to the excitation beam. By measuring the intensity correlation under different illumination conditions, one can separate for example the fluctuations originating from intermolecular dynamics, from those originating from the dye itself. The basic idea is explained in fig 2.9(a, b). As the probe beam is displaced with respect to the lock point of the tracking feedback and goes from a centered position (illumination state 0) to an offset position (illumination state 1), the probe dye sees a different excitation profile (2.9.a). As discussed earlier in this chapter, the gradient of the excitation field being larger in state 1 than in state 0, small motions of the probe within the beam results in fluorescence fluctuations with larger amplitude, and contribute to a larger signal in the intensity correlation as sketched in fig. 2.9.b. However, the dye blinking dynamics is unaffected by the change in illumination pattern and contributes to an equal amount to the correlation functions obtained under the two different illumination conditions. One can then essentially subtract the two correlation functions to obtain a signal that is free of the dye blinking dynamics. The details of how to combine the correlation functions obtained under the illumination conditions is described below.

2.3.2 Natural suppression of dye blinking from tracking-FCS signals

We represent the effect of the physical state of the dye on the fluorescence signal by the stochastic process D_t such that the intensity is

$$I_t = D_t \Phi(x_t) + k$$

For example, for a two-state model where the dye can be either on or off, D_t is equal to 0 when the dye is off, and is equal to 1 when the dye is on. More complicated models can fit into a similar description. Using the algebraic rules on correlation functions derived earlier in this chapter and the fact D_t and x_t are independent processes, the measured correlation function factorizes into

$$g_{\text{meas}}(\tau) = g_{D\Phi}(\tau) \frac{E[D\Phi]^2}{(E[D\Phi] + k)^2} = (-1 + (1 + g_D(\tau))(1 + g_\Phi(\tau))) \frac{1}{\Theta} \quad (2.41)$$

where Θ now includes the dye blinking

$$\Theta = \left(1 + \frac{k}{E[D\theta]}\right)^2 \quad (2.42)$$

and can be obtained directly from the data, using the mean intensity before and after bleaching. The first step in the tracking-FCS data processing is therefore to correct for the background contribution by computing the signal correlation function:

$$g_{\text{signal}} = \Theta g_{\text{meas}} \quad (2.43)$$

Suppose now we measure the signal correlation function for two different values of the beam offset, δ_0 and δ_1 , denoted $g_{\text{signal}}(\tau, \delta_0)$ and $g_{\text{signal}}(\tau, \delta_1)$. We define the relative correction function

$$\Delta g(\tau) = \ln(1 + g_{\text{signal}}(\tau, \delta_1)) - \ln(1 + g_{\text{signal}}(\tau, \delta_0)) \quad (2.44)$$

The dye process D_t is independent of the beam position, and the only term in eq.

(2.44) that is a function of δ is $g_\Phi(\tau)$. Therefore, the dye contribution cancels out and using expression (2.8) we obtain

$$\Delta g(\tau) = \ln(1+g_\Phi(\tau, \delta_1)) - \ln(1+g_\Phi(\tau, \delta_0)) = -\frac{1}{2}(\delta_1^2 - \delta_0^2) C^T ((\mathbb{I} + \Sigma)^{-1} - (\mathbb{I} + \Sigma_\infty)^{-1}) C \quad (2.45)$$

where $C = \begin{pmatrix} 1 \\ 1 \end{pmatrix}$. The amplitude has a quadratic dependency in the laser positions δ_0 and δ_1 . Interpretation of the relative correlation function therefore requires careful calibration of the microscope, where the position of the beam needs to be known accurately for both illumination conditions.

Alternatively, it is possible to perform a calibration free normalization, by remarking that the relative fluorescence intensity, defined as

$$\Delta \bar{I} = \ln(\bar{I}(\delta_1)) - \ln(\bar{I}(\delta_0)) \quad (2.46)$$

has the same quadratic dependency in the laser offsets.

$$\Delta \bar{I} = -\frac{1}{4}(\delta_1^2 - \delta_0^2) C^T (\mathbb{I} + \Sigma_\infty)^{-1} C \quad (2.47)$$

Therefore we can obtain a self-calibrated fluorescence correlation signal which does not require knowledge of the beam position, by using a normalized version of the relative correlation function

$$\Delta g_{\text{norm}(\tau)} = \frac{\Delta g(\tau)}{\Delta \bar{I}} = 2 \frac{C^T ((\mathbb{I} + \Sigma)^{-1} - (\mathbb{I} + \Sigma_\infty)^{-1}) C}{C^T (\mathbb{I} + \Sigma_\infty)^{-1} C} \quad (2.48)$$

The normalized relative correlation function is appealing because it is only a function of the motion of the probe dye, via the covariance matrix function $\Sigma(\tau)$, and the dye dynamics is naturally deconvolved out.

2.3.3 Model-free extraction of position dynamics from fluorescence correlation data

Using the normalized relative correlation function

The normalized relative correlation function has the convenient advantage of being analytically tractable. There is in fact a closed expression for the correlation matrix Σ as a function of $\delta g_{\text{norm}}(\tau)$. Starting from eq. (2.48) and explicitly writing the matrix elements of Σ as in eq. (2.9), we derive the following relations:

$$v = -\frac{\Delta g_{\text{norm}}(0)}{2(\Delta g_{\text{norm}}(0) + 1)} \quad (2.49)$$

$$c(\tau) = -\frac{v\Delta_{\text{norm}}(\tau) + \Delta_{\text{norm}}(\tau)}{v(\Delta_{\text{norm}}(\tau) + 2)} \quad (2.50)$$

Expression (2.49) provides a practical way to directly convert the intensity correlation function $g(\tau)$, which is experimentally measured, into a position correlation function $\Sigma(\tau)$ which is the quantity of interest. This approach contrasts with the typical workflow in conventional FCS. In conventional FCS, the various processes that contribute to the fluorescence correlation function cannot be easily separated from one another, and there is a large number of unknown parameters that need to be estimated all at once. Even for a homodisperse solution of particles, the simplest model contains four unknown parameters (diffusion coefficient, concentration, transition rates of the 2-states model describing the dye blinking). For this reason interpretation of FCS data is challenging, requires careful experimental crosschecks (for example it is common to repeat the experiment at different laser powers and concentrations), and is prone to errors and misinterpretations as different models or even different set of parameters for a given model can provide equally good fit of the data. This is especially true for complicated systems, such as mixture of different species and systems with internal coordinates (ex: systems with molecular reactions or conformational dynamics), or systems where a simple Brownian diffusion is not a good model. Tracking-FCS offers a clear advantage in that respect. In addition to being a

single molecule measurement (being thereby naturally adapted to the study heterogeneous systems), the precise positioning of the probe beam w.r.t to the molecule allows us to tune the relative contribution of the molecular motion and the dye blinking to the correlation signal, deconvolve these two contributions, and ultimately be left with a one dimensional estimation problem. This is a fit-free procedure that does not require modeling of neither the dye photophysics nor of the intermolecular dynamics.

Using the non-normalized relative correlation function

If the position of the laser is well calibrated and we know the values of the offsets δ_0 and δ_1 , it is also possible to use directly the non-normalized version of the relative correlation function. In that case, we first compute Δg_{calib} defined by

$$\Delta g_{\text{calib}}(\tau) = \frac{\Delta g(\tau)}{\delta_1^2 - \delta_0^2} \quad (2.51)$$

And we can solve for c and $v(\tau)$ as a function of Δg_{calib} . One problem with this approach is that there are in fact too solutions for the variance v :

$$v = \begin{cases} \frac{1-3x-\sqrt{1-6x+x^2}}{4x} & \text{if } v < 1/\sqrt{2} \\ \frac{1-3x+\sqrt{1-6x+x^2}}{4x}, & \text{if } v > 1/\sqrt{2} \end{cases} \quad (2.52)$$

where $x = \Delta g_{\text{calib}}$. If we know if $v < 1/\sqrt{2}$ or $v > 1/\sqrt{2}$, then we can pick the right solution. And the correlation function can then be obtained according to:

$$c(\tau) = -\frac{(1+v)^2 x}{v(-1+x+vx)} \quad (2.53)$$

Note however that the solution will be very inaccurate for v near or larger than $1/\sqrt{2}$. This can be seen on figure 2.7, which shows the amplitude of the calibrated relative correlation function $\Delta g_{\text{calib}}(0)$ and of the normalized relative correlation function $\Delta g_{\text{norm}}(0)$.

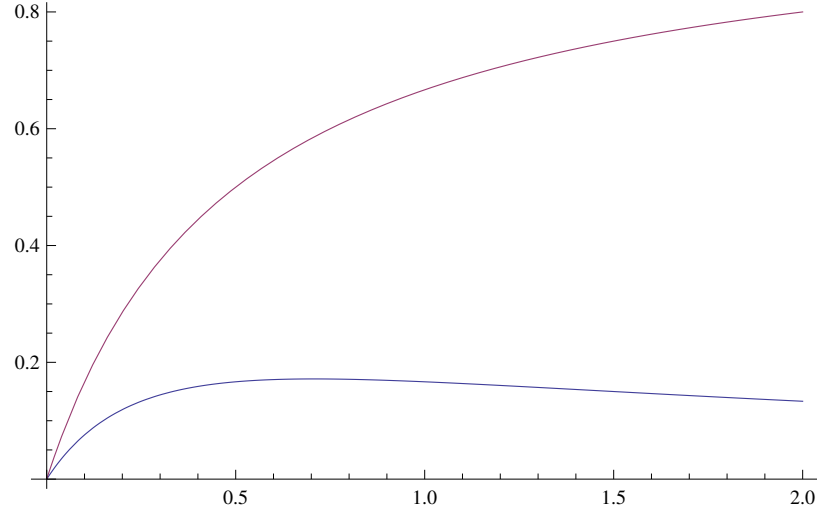


Figure 2.7: Amplitude of the calibrated relative correlation function $\Delta g_{\text{calib}}(0)$ (blue) and of the normalized relative correlation function $\Delta g_{\text{norm}}(0)$ (red) as a function of the variance v

2.3.4 Suppression of tracking-error and extraction of the correlation function for the internal dynamics

The only undesired contribution that is left over after inversion of the normalized relative correlation function is the tracking-error contribution. The correlation matrix given by equations (2.49) is $\Sigma = \Sigma_{\text{id}} + \Sigma_{\text{err}}$. To obtain the position correlation function of the internal dynamics only, we simply need to measure separately the position correlation function for the tracking error, and subtract the corresponding covariance matrix Σ_{err} to Σ . The position covariance function of the tracking error can be obtained by taking data on control molecules that are labeled so that the probe and reference dyes are next to each other (cf. chapter 3). The tracking-FCS data processing flow is summarized in fig. 2.8.

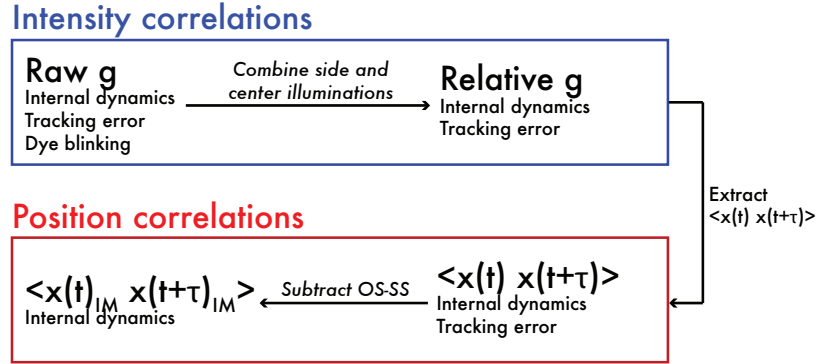


Figure 2.8: Data processing steps to convert the fluctuation correlation functions to end-to-end position correlation functions, that do not have dye or tracking contribution.

2.4 Switched-illumination tracking-FCS and single molecule deconvolution of the dye dynamics

A drawback of the scheme presented in the previous section is that tracking-FCS data need to be taken with two different configurations of the microscope. Typically, 10-100 molecules are tracked under illumination state 0, and the fluorescence correlation function is computed for each molecule individually. Then the illumination state is switched to state 1, another 10-100 molecules are tracked and their fluorescence correlation function computed. In order to combine the correlation functions obtained in both illumination conditions, the data need to be averaged over all the molecules to obtain a single correlation function per illumination state. This loses the single molecule nature of the tracking-FCS assay. The long-observation period of an individual molecule in tracking-FCS allows to get around this problem as each individual molecule can be exposed to the two illumination conditions. To achieve this, the probe beam is periodically switched between the two states 0 (center) and 1 (offset) several times during the course of a tracking event (fig. 2.9b.). The collected photons are then sorted based on the illumination state at the time of emission (0 and 1), to produce two gated photon streams $I_{|0}$ and $I_{|1}$ (fig. 2.9c). The correlation function is then computed for each gated stream of photons individually, to obtain the gated correlation functions $g_{|0}$ and $g_{|1}$. We can then compute a single-molecule

version of the relative correlation function using the two gated correlation functions to obtain a deconvolved signal free of any contribution from the dye dynamics. The switched-illumination assay can be thought of as a way to multiplex multiple experimental illumination conditions into a single photon stream, while the gating of the photon stream performs the demultiplexion operation.

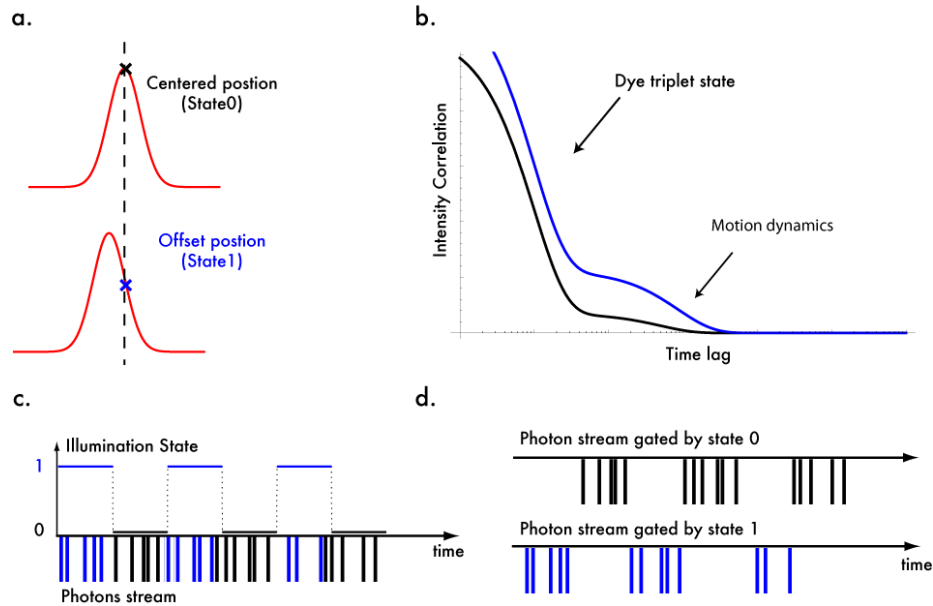


Figure 2.9: a. As the probe beam (red) is displaced with respect to the locking point of the tracking feedback (dashed line), the probe dye (x) sees a different excitation gradient. b. Typical form of the intensity correlation under the two illumination conditions (1 blue, 0 black). Here we assumed a fast triplet state dynamics and a slower motion dynamics of the probe. Note that the two timescales were chosen far from each other in this schematic but this does not need to be the case in practice. c During the course of a tracking event, beam is rapidly moved from the centered (state 0) to the offset position (state 1). d. A single stream of photon is gated by the switching signal to generate two photon streams corresponding to illumination states 0 and 1

In presence of switching, the processing steps described in the previous section, background correction, relative correlation function and normalization apply almost identically, but the background correction needs to be slightly adapted. The intensity

processes used to compute the gated correlation functions are of the form

$$I_{t|i} = S_{i,t}(D_t\Phi(x_t, \delta_i) + k) \quad (2.54)$$

where $i = 0, 1$ represents the illumination state and $S_{i,t}$ is a deterministic function which accounts for the gating process by selecting the photons that arrived during illumination state i . $S_{0,t} = 1$ when the laser is at offset position δ_0 , and $S_{0,t} = 0$ when the laser is at offset position δ_1 . Likewise, $S_{1,t} = (1 - S_{0,t})$ is 1 when the laser is in position 1 and 0 otherwise. Using the rules for correlation functions with periodic modulation derived earlier, we obtain

$$g_{|i} = g_{S_i D\phi} \frac{(E[S_i D\phi])^2}{(E[S_i D\phi] + E[S_i k])^2} + g_{S_i} \frac{(E[S_i k])^2}{(E[S_i D\phi] + E[S_i k])^2} + 2 \frac{E[S_i k] E[S_i D\phi]}{(E[S_i D\phi] + E[S_i k])^2} g_{S_i D\phi, S_i k} \quad (2.55)$$

Note that the cross term in eq. (2.55) is not zero in the presence of strobing, which is why the background correction needs to be adapted.

Using the rule on products, the cross correlation $g_{S_i D\phi, S_i k}$ is

$$g_{S_i D\phi, S_i k} = (1 + g_{D\phi, k})(1 + g_{S_i}) - 1 = g_{S_i} \quad (2.56)$$

where

$$g_{S_i} = \frac{\langle S_i(t + \tau) S_i(t) \rangle}{\bar{S}_i^2} - 1$$

There are two ways to obtain g_{S_i} . The first way is to use eq xxx directly, using the explicit form of S_i (a square wave for example if we use a square modulation as shown in fig xxx).

The second way is to simply compute the correlation function for experimental data corresponding to molecules with a photobleached probe dye. In that case, $D\phi = 0$ and the measured correlation is g_{S_i} . In practice, we use the "experimental" way as it is more robust to changes in the strobing signal $S_i(t)$ (for example if the square wave is not perfectly 50 percent duty cycle, this is accounted for directly by method

2). In the switched illumination case, we redefine the background correction factor as

$$\theta_i = \left(1 + \frac{E[S_i k]}{E[S_i D \phi]}\right)^2 \quad (2.57)$$

θ_i is obtained directly from the data through the equation

$$\theta_i = \left(\frac{\bar{I}_{|i}}{\bar{I}_{|i} - \bar{I}_{|i,bck}}\right)^2 \quad (2.58)$$

where $\bar{I}_{|i}$ is the average intensity of the gated photon stream, and $\bar{I}_{|i,bck}$ is the average intensity of the gated photon stream for molecules that do not have a probe dye (gated background intensity). Therefore, using eq. (2.57) and rearranging terms in eq. (2.55), we obtain

$$g_{|i,\text{signal}} = g_{|i}\theta_i - g_{S_i}(\theta_i - 1) \quad (2.59)$$

Eq. (2.59) allows us to obtain the signal contribution $g_{S_i D \theta}$ of the measured gated correlation function $g_{|i}$ in the presence of background ($\theta_i > 1$).

Subsequent steps to obtain the relative correlation function and its normalized version are unchanged.

Chapter 3

Instrumentation and tracking performance

In the first part of this chapter, I describe the optical implementation of the tracking microscope. I first give a very brief overview of the previous version of the apparatus and discuss some of the limitations that I sought to improve. I focus next on detailing the changes made to the instrument, which allow faster tracking feedback and better control over the position of the laser beams. In the second part of the chapter, I present a mathematical description of the instrument seen as a dynamical system. I include some theoretical results to discuss the performance of the revised instrument, and the expressions for the laser and stage position correlation functions, which are important for fitting and interpreting the position trajectory data obtained from tracking experiments.

3.1 Optical design

3.1.1 General principles and original design

Introduction

For details about the original instrument developed in the Mabuchi lab, I recommend in particular reading Andrew Berglund's or Kevin McHale's thesis [38, 39], which give

fairly complete descriptions of the setup and discuss practical aspects and limitations of some of the core optical components. I start here with a very brief description of the tracking microscope instrumentation, which should serve as a basic standalone introduction.

The tracking microscope consists essentially of a confocal fluorescence imaging setup equipped with a feedback loop. To obtain real-time position information on the diffusing molecule, we employ a fluorescence modulation strategy. The tracking laser beam (561nm) is tightly focused to form a near diffraction limited optical excitation volume in a diluted solution of fluorescently labeled molecules. Using acousto-optic modulators (AOMs), the focus of the beam is steered along a circular rotation pattern at 100kHz to achieve high frequency modulation of the fluorescence signal in a position dependent manner. The fluorescence signal is demodulated by a lockin amplifier along two orthogonal quadratures to obtain an (x, y) error signal proportional to the distance between the particule and the center of the rotation. The error-signal is then fed to an integral controller. The output of the controller drives a 3D-piezo stage on which the sample is mounted so as to maintain the particle in the focus of the excitation beam.

The rotation radius of the orbit can be optimized to minimize the localization error [27]. For detecting the position of the particle along the z-axis, a similar modulation strategy is used. The initial design uses a second copy of the rotating beam used for XY tracking, but with its focus plane shifted a few microns either above or below the focus plane of the initial beam. We then alternate excitation between the two focal planes at 95kHz to obtain a fluorescence modulation that is dependant on the position of the particle along the z axis, at a frequency orthogonal from the frequency encoding the XY position. A second lockin amplifier demodulates the fluorescence signal and just like for XY, feeds an integral controller which drives the z piezo stack.

Note that in this implementation, the rotation of the beam is generated by AOM rather than by galvanometric mirrors, as it is the case for the other tracking-feedback microscopes developed in other groups. Because of the higher bandwidth of the AOM compared to galvanometric mirrors, the rotation can be chosen to be an order of magnitude faster than with a galvanometric implementation.

Limitations and desired improvements

While the original microscope functioned well and was able to track particles as fast as $20\mu m^2/s$, the tracking-FCS measurements that I aimed to obtain required more stringent conditions on the performance of the instrument. The first essential limitation that needed to be addressed was the tracking bandwidth. Because the original implementation used the 3D piezo stage as the only actuator, the bandwidth of the feedback loop was limited by the mechanical resonances in the stage and could not exceed 100Hz. As we will see in the second part of this chapter, this limitation not only affects the ability to track molecules diffusing faster than $20\mu m^2/s$, but also the accuracy with which we are able to track slower molecules. The best achievable mean square tracking error with a bandwidth of 100Hz is on the order of 200nm for a particle diffusing at $10\mu m^2/s$. Unfortunately, this figure of merit is not good enough to resolve internal dynamics on length scales below 100nm.

Besides extending the feedback bandwidth, another aspect of the instrument that I sought to improve was the optical implementation of the intensity modulation along the propagation axis. Obtaining a sensitive position detection along the z axis is intrinsically more difficult than in the lateral directions for 2 reasons. First, there is no simple equivalent of an AOM to displace the beam focus axially. Second, gaussian optics dictates that the intensity gradient at the focus is shallower along the propagation direction than in the transverse plane. Even for a diffraction limited beam, which has the smallest aspect ratio at the waist, the beam waist diameter is roughly $w = \lambda/2$, whereas the Raleigh range is $z_r = \lambda\pi/w^2 \approx \lambda\pi/4$. Therefore, to obtain the same amplitude of fluorescence modulation with an axial dithering as with a transversal dithering, the dithering amplitude needs to be larger in the axial case. The dual beam strategy offers an elegant and simple solution, but it has the inconvenient of not being dynamically adjustable. In particular, without a dedicated optical design, it is difficult to control the distance between the two foci. This can be done by changing the position of lenses along one of the two beam paths, but this is a tedious procedure which require time consuming realignment of the instrument. Additionally, one needs to pay attention to not affect the beam waist and the amplitude of the transversal modulation at the same time. More importantly, using two

independent beams introduces an additional alignment concern. Improper alignment of the two tracking beams results in a coupling between the (x,y) and z error signals and in a z-dependent gain in the feedback loop, which deteriorates tracking performance. I found that this alignment needed to be done carefully on a regular basis (at least before every new set of experiments), and was difficult to optimize, resulting in a lot of variability in the data quality. I therefore sought to modify the instrument to permit a more flexible control of the axial position of the beam.

In fact, the microscope should ideally have a single beam per excitation wavelength, with fast and accurate electronic control of the foci positions in the x,y and z directions. This would permit both a simpler fluorescence modulation scheme, high tracking bandwidth, as well as rapid reconfigurability of the illumination conditions. We have highlighted in the previous chapter that reconfigurability of the beams positions is important in the context of tracking-FCS. The changes I have implemented in the microscope design, as well as some additional improvements that are currently being made towards these goals are discussed in the next section.

3.1.2 Redesigned apparatus

Optimal design for (x,y,z) scanning

To obtain high bandwidth control over the lateral position of the tracking beam, we use the same AOMs that are used to generate the rotation of the tracking beam. The feedback control loop employing these AOM for high bandwidth tracking is described in the second part of this chapter. A similar design is used for the probe beam for which I have introduced a pair of acousto-optic modulator to get independent control of the probe and tracking beams position. Control of the beams position along the z axis is more difficult. Several methods have been proposed to achieve remote axial scanning (i.e. the ability to move focus plane of the beam in the sample in a situation where the objective lens and the sample remain fixed). For example, it has been demonstrated that AOM can be driven by chirped signals to produce a tunable focusing effect [40]. Remote axial scanning has been demonstrated in the context of two-photon microscopy by means of pulse shaping and temporal focusing strategies

[41]. More recently, optical elements that essentially behave as lenses with variable and controllable focus have become commercially available. These include Tunable Acoustic Gradient lenses, and electrically adressable lenses based on elastic polymers, which have found use in various imaging applications. We will discuss the use of these two components later in this chapter.

Independently of the method used to achieve remote scanning, the optical system for a tracking microscope must be designed so as to reach some important criteria. First, we need to be able to displace the focus position in the sample along the 3 axis independently. In particular, axial and lateral scanning must be decoupled such that a change in deflection angle by the AOM does not move the focus axially. Reciprocally, an axial displacement of the focus should not shift the beam laterally or induce a change in waist size. Additionally, acousto-optics based beam deflection permits hight bandwidth control of the beam position but this comes to the expand of range. The range of angular displacement of the beam that can be obtained is on the order of 10mrads. Therefore it is important to design the imaging system such that a given angular displacement generated by the AOM matches to a maximally large lateral displacement in the sample focus plane. Let's note $r_s(\theta_0, z_0)$ and $z_s(\theta_0, z_0)$ the transversal and axial position of the focus on the sample side of the imaging system, and $w_s(\theta_0, z_0)$ the corresponding waist. They are both functions of the deflection angle generated by the AOM θ_0 and of z_0 , the position of the incoming beam waist the nearest to the AOM (z_0 is somewhat loosely defined here but it will become clearer what we mean by z_0 as we define the imaging system more precisely later on). The desired properties described above give rise to 5 design constraints:

1. Maximize $\frac{\partial r_s}{\partial \theta_0}$
2. Maximize $\frac{\partial z_s}{\partial z_0}$
3. $\frac{\partial z_s}{\partial \theta_0} = 0$
4. $\frac{\partial r_s}{\partial z_0} = 0$
5. $\frac{\partial w_s}{\partial \theta_0} = 0$

$$6. \frac{\partial w_s}{\partial z_0} = 0$$

The constraints 3 and 5 are automatically satisfied in the paraxial approximation ($\theta_0 \ll 1$). It turns out that there is an optimal positionning of the relay lenses that satisfies all remaining 4 criteria, which corresponds to maintaining a telescope condition between each lens: the distance between any pair of lenses should be equal to the sum of their focal length.

To derive this result, it is sufficient to consider the effect of a single lens with focal length f , placed at a distance d away from the acousto-optic modulator which coincides with the focus plane of a gaussian beam. Gaussian optics dictates that the beam configuration before the lens (resp. after the lens) is entirely defined by 4 parameters: the position of the waist z_w and the waist size w (resp. z'_w and w' after the lens), as well as the angle θ (resp. θ' after the lens) between the optical axis and the beam propagation axis, and the lateral distance r_w (resp. r'_w after the lens) between the optical axis and the focus. The relationship between the beam parameters (z_w, w) and (z'_w, w') before and after the lens requires gaussian optics and can be calculated using ABCD matrices. The ABC matrix that accounts for the propagation of the beam in free space from the AOM to the lens over a distance d , followed by propagation through the lens of focal length f is given by

$$M = \begin{pmatrix} 1 & 0 \\ -1/f & 1 \end{pmatrix} \begin{pmatrix} 1 & d \\ 0 & 1 \end{pmatrix} = \begin{pmatrix} 1 & d \\ -1/f & 1 - d/f \end{pmatrix} \quad (3.1)$$

Denoting q the complex gaussian beam parameter at the focus before the lens, and q' the beam parameter right after the lens, we have

$$q' = \frac{qM_{1,1} + M_{1,2}}{qM_{2,1} + M_{2,2}} \quad (3.2)$$

with

$$q = iz_R, \quad z_R = \frac{\pi w^2}{\lambda} \quad (3.3)$$

The waist at the focus point after the lens, w' , and the position of the focus relative

to the lens z'_w are obtained by solving

$$z'_R = \frac{\pi w'^2}{\lambda} = \text{Im}(q), \quad z'_w = -\text{Re}(q') \quad (3.4)$$

In order to achieve condition 3, we are interested in maximizing the axial sensitivity $\frac{\partial z_w}{\partial d}$. From eq. (3.2) we have

$$\frac{\partial q'}{\partial d} = \frac{1}{(-1/fiz_R + 1 - d/f)^2} = \frac{(1 - d/f)^2 - z_R^2/f^2 + 2z_R/f(1 - d/f)}{((1 - d/f)^2 + z_R^2/f^2)^2} \quad (3.5)$$

Hence

$$\frac{\partial z_w}{\partial d} = \frac{(1 - d/f)^2 - z_R^2/f^2}{((1 - d/f)^2 + z_R^2/f^2)^2} \quad (3.6)$$

The extremum of $\frac{\partial z_w}{\partial d}$ is reached for $d = f$ and in that case we have

$$\left. \frac{\partial z'_w}{\partial d} \right|_{d=f} = \sup_d \left| \frac{\partial z'_w}{\partial d} \right| = \left(\frac{f}{z_R} \right)^2 \quad (3.7)$$

This dictates that if we want to maximize the axial sensitivity, we should place the lens exactly one focal lens away from the object focus plane. In that configuration, we obtain also immediately

$$\frac{\partial z'_R}{\partial d} = \frac{\pi}{\lambda} \frac{\partial w'^2}{\partial d} = \text{Im} \left[\frac{\partial q'}{\partial d} \right] = 0 \quad (3.8)$$

To a first order approximation, the waist size in the image plane is unaffected by the axial motion, so condition 4 is also satisfied. To compute the lateral sensitivity we can use ray optics to relate the vector $\begin{pmatrix} r \\ \theta \end{pmatrix}$ describing the beam position and propagation

orientation in the object focal plane of the lens to the vector $\begin{pmatrix} r' \\ \theta' \end{pmatrix}$ describing the beam in the image focal plane. Using here again the ABCD matrices formalism, we obtain

$$\begin{pmatrix} r' \\ \theta' \end{pmatrix} = \begin{pmatrix} 1 & d' \\ 0 & 1 \end{pmatrix} M \begin{pmatrix} r \\ \theta \end{pmatrix} = \begin{pmatrix} 1 - d'/f & d + d' - dd'/f \\ -1/f & 1 - d/f \end{pmatrix} \begin{pmatrix} r \\ \theta \end{pmatrix} \quad (3.9)$$

where d' is the distance from the lens to the image focus plane and is

$$d' = -Re[q'] = f \frac{z_R^2 + d^2 - df}{z_R^2 + d^2 - 2df + f^2} \quad (3.10)$$

From these results, we obtain the lateral sensitivity

$$\frac{\partial r'}{\partial \theta} = d + d^2 - dd'/f = \frac{fz_R^2}{z_R^2 + (1 - d/f)^2} \quad (3.11)$$

which is maximized when $d = f$.

In conclusion, conditions 1,2,4,6 are simultaneously satisfied when the input waist is placed one focal length away from the lens. It follows from that result that for any given series of lens, the unique configuration that satisfies conditions 1 through 6 is the configuration where all the lenses are separated by the sum of their focal length.

3.1.3 Remote axial scanning using a relay objective lens in double pass configuration

To control the axial position of the beam waist with respect to the AOM, and obtain orthogonal control of the lateral and axial focus point of the beam in the sample, we used the configuration shown in figure 3.1. The beam is focused onto a piezo mirror by a relay microscope objective and back reflects to form a focus on the AOM. A small displacement of the mirror leads to an axial displacement of the beam focus which coincides with the AOM and which maps onto an axial displacement of the beam in the sample. Lenses f_2 and f_3 in this system serve as a telescope to control the beam size in the AOM.

While we can use equations derived in the previous section to evaluate more precisely the lateral and axial scanning properties of the imaging system, it is more important to characterize the system experimentally, as there will be unavoidable errors in the positioning of the lenses. However the analysis done in the previous is extremely useful to provide guidelines for designing the system in the first place, and in particular to decide what combination of lenses should be used to obtain

the appropriate scanning range in both the axial and lateral directions. For example, for the choice of the lenses shown in fig. 3.1 corresponding to $f_2 = 500, f_3 = 75.6, f_4 = 125, f_5 = 300, f_{\text{obj,scan}} = 165/40$, we can expect that a displacement δz of the mirror should provide an axial displacement of the focus in the sample of $\delta z_s = 2 \left(\frac{f_2}{f_{\text{obj,scan}}} \frac{f_4}{f_3} \frac{f_{\text{obj}}}{f_5} \right)^2 \delta z \approx 6.5 \delta z$

This configuration can be used for any of the optical beams that we wish to control. We used this configuration for the 561nm tracking beam and 635nm probe beam. We did not implement this configuration on the 488nm GFP detection beam.

My original idea was to use this optical configuration as a way to replace the existing z-modulation involving alternative excitation with two separate beams. By rapidly dithering the piezo mirror, I thought that I would be able to generate a rapid axial scanning of a single rotating beam. That way, a single tracking beam would be necessary for x,y,z tracking, which would potentially greatly reduce the alignment overhead. However, this approach did not succeed as even the smallest piezo I was able to find commercially (few μm range) had too high a capacitance to be easily driven at the desired frequency (10kHz or more) without excessive heating due to the large currents involved. Additionally, I found that aligning the scanning objective and the scanning mirror properly to avoid coupling between the axial and lateral beam motion was a challenging task. This problem by itself negated the original motivation for using the piezo mirror as a modulation element to obtain an axial error signal. However, the scanning mirror turned out to be useful to adjust the position of the beam, and I decided to keep it for that reason.

A simplified schematic of the first version of the redesigned setup, is show fig. 3.1. Most relay lenses are left out of this schematic for the sake of simplicity. This configuration still involves two tracking beams, but one of them uses the arrangement described above with a double pass through the relay objective. This allows us to use the piezo mirror to simply adjust the distance between the two tracking beams. The actual instrument as it was in June 2013 can be seen on the picture figure 3.2 (Photo taken by Hardeep Sanghera).

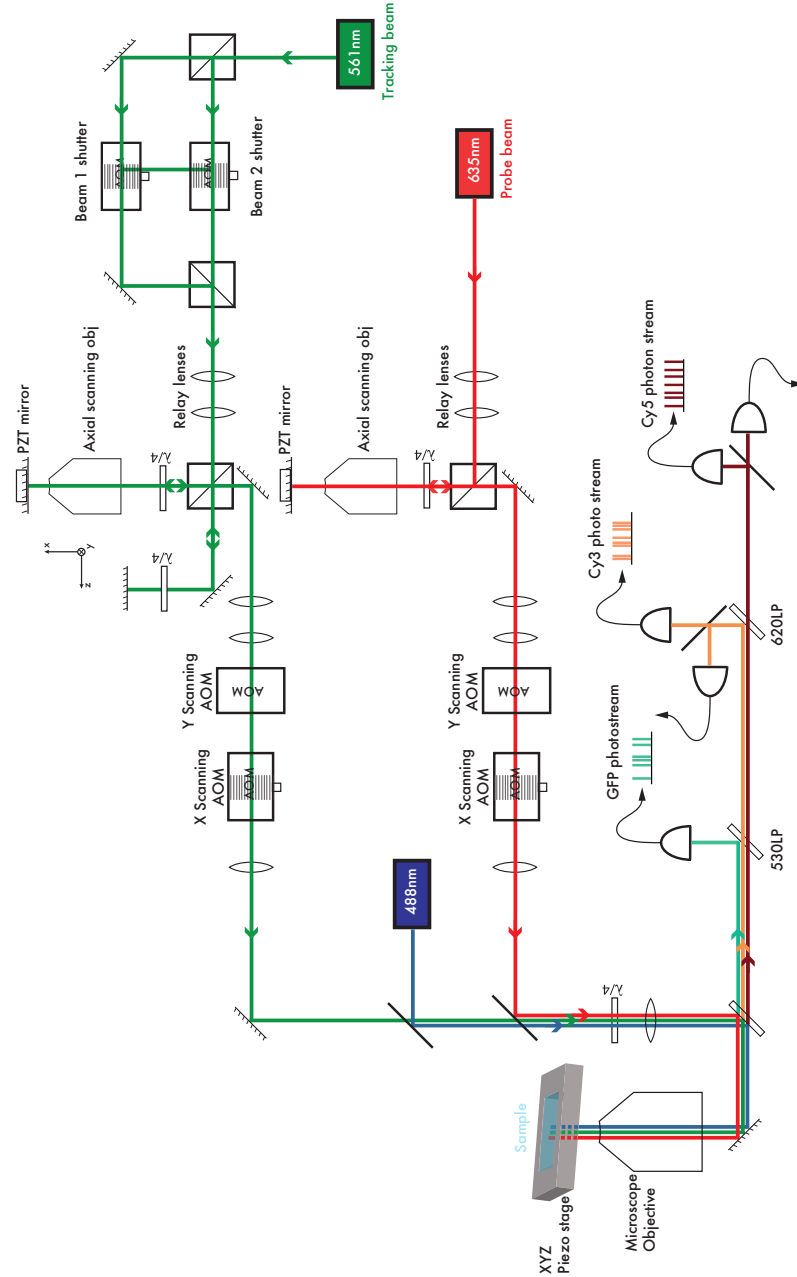


Figure 3.1: Simplified optical design of the tracking microscope with 3 excitation wavelength. AOMs are used to control the lateral position of the focus of the tracking beam (561nm) and the probe beam (635nm). The axial position of these two beam foci is adjusted by moving the piezo mirror located at the focus of a scanning objective. A third beam at 488nm can be used to detect binding of GFP tagged molecules during tracking.

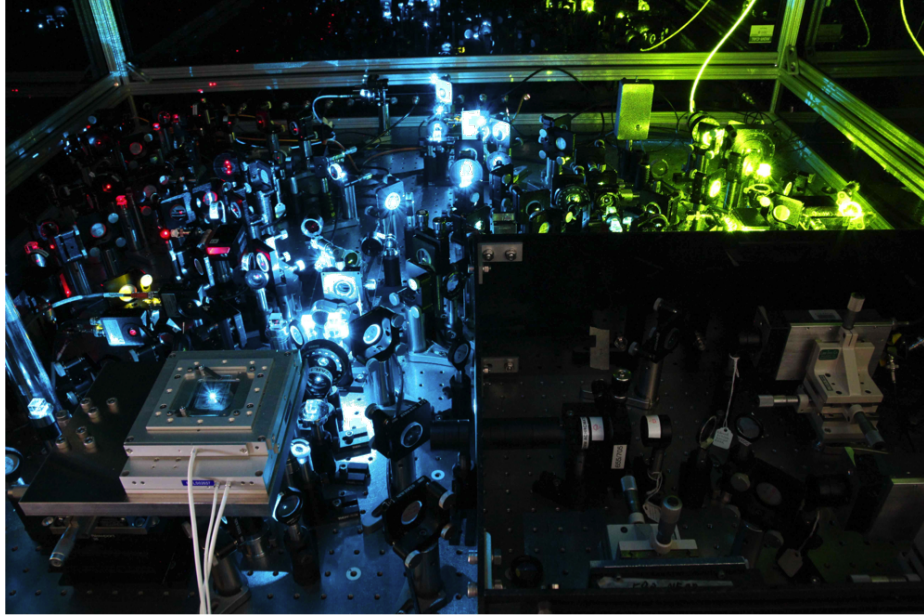


Figure 3.2: Picture of the tracking microscope in June 2013.

3.1.4 Wide-band axial scanning and positioning using a Tunable Acoustic Gradient lens and an elastic polymer lens

I am currently replacing the dual beam configuration by a configuration involving a tunable acoustic gradient lens and a variable focus elastic polymer lens. The idea of this design is to use a tunable acoustic gradient lens (TAG) to generate a fast axial dithering of the beam to produce the z-error signal, and an elastic polymer lens to apply a DC or low frequency bias to the axial position of the focus. Since these components are fairly new, I first briefly describe their principle of operation, and I then describe how to set them up in the tracking microscope. At the time of this writing, I have installed the TAG lens and have already been able to track freely diffusing fluorescent beads with a single tracking laser (fig.3.3 shows the TAG lens in the microscope). The elastic polymer lens has not been set up in the instrument yet.

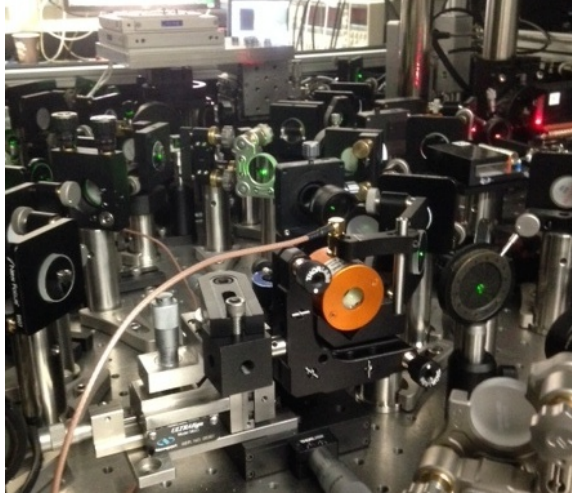


Figure 3.3: Picture of the TAG lens (in orange) recently inserted in the tracking microscope, and mounted on a v-groove sitting on top of a mirror mount positioned on an XZ translation stage.

Tunable Acoustic Gradient Lens

The TAG lens is a relatively simple optical component, but it is only recently that the technology has become commercially available (Tag Optics Inc.). TAG lenses have now been used for various applications, including for the generation of Bessel beams [42] and for fast axial scanning in microscopy [43, 44, 45]. The TAG lens essentially consists in a cavity filled with a refractive fluid. The cavity shell is driven by a cylindrical piezo actuator which creates a standing acoustic wave in the fluid. The acoustic wave alters the refractive index $n(r, t)$ inside the cavity according to (a detailed mathematical description of the acousto mechanical response of the lens can be found in [2])

$$n(r, t) = n_0 + n_a J_0 \left(\frac{\omega r}{\nu} \right) \sin(\omega t) \quad (3.12)$$

where J_0 is the first Bessel function of the first kind, r is the radial position inside the lens, ν is the speed of sound in the fluid, n_0 the refractive index of the fluid, and n_a is the amplitude of the refractive index modulation and depends on the lens design and the drive amplitude and frequency ω (typically $n_a \approx 10^{-5}$). This is a standing wave oscillating at frequency ω with a Bessel profile displaying a central peak of width

given by

$$w_0 = \frac{\nu}{\omega} z_0 \quad (3.13)$$

where z_0 is the first zero of the bessel function. When the beam size is large compared to the width of the central peak ($w > w_0$) it can be shown that the TAG lens essentially behaves like an axicon and produces a Bessel beam. Here, we are interested in the situation where the beam waist is small ($w < w_0$). In that case, the variation of the refractive index as a function of the distance to the optical axis is approximately quadratic, and the TAG lens behaves as a conventional lens where the focal power $1/f_{\text{TAG}}$ is inversely proportional to the radius of curvature of the index profile:

$$1/f_{\text{TAG}} \propto \frac{\partial^2 n}{\partial r^2} \propto n_a \omega^2 \sin(\omega t) \quad (3.14)$$

Therefore, the power of the TAG lens oscillates at the drive frequency ω . Additionally, there is a tradeoff between lens power and optical aperture. A large drive frequency ω leads to a larger oscillation amplitude ((3.14)), but reduces the optical aperture according to equation (3.13). The TAG lens we use (Tag Optics Inc.), has a few resonance frequencies between 140kHz and 515kHz. In practice we are using a small beam through the lens ($w < 1\text{mm}$) and we can use the largest resonance frequency which produces maximal swing in the focal length (+/- 30 diopters) without any noticeable aperture effect.

There are typically two possible ways to operate the TAG lens as a variable focus optical element. In the first mode of operation (which appears to be the most common scenario), the lens is used with a pulsed laser phase locked with the drive cycle of the lens. As a result, each pulse effectively experiences a frozen refractive profile, and the TAG lens acts as a conventional lens where the focal power is controlled by the relative phase between the lens oscillation and the laser. The other mode of operation, which is the one we are interested in, is when the lens is used with a CW laser. In that case, the focal length of the TAG lens continuously oscillates at the drive frequency ω . This mode of operation is ideal for continuously scanning the axial position of focus, and is therefore ideal to replace the dual-beam configuration used in the original tracking microscope. The optical arrangement necessary to obtain correct axial scanning in

the sample using the TAG lens is discussed in the next section.

Electrically tunable lens

While the TAG lens is ideal for generating the continuous oscillation of the beam focus along the z-axis for phase sensitive position detection, it is not possible to operate the lens so as to obtain a static displacement of the focus. Such a feature is useful for alignment purposes (for example to align the tracking and probe laser foci axially), as well as a way to electronically control the position of various beams in the sample and allow for rapid reconfigurability of the illumination geometry in the sample. A simple solution to control the axial position of the beam focus is to use a tunable lens based on elastic polymer. These lenses are sold by Optotune, and are composed of a refractive fluid filling a cylindrical container made out of an elastic polymer that can be deformed by the mechanical displacement of a ring. The deformation of the container changes the shape of the lens and alters its optical power, which can be tuned between 8 and 22 diopters. Additionally, the focal power of the lens is current controlled and the focal power is linear in the applied current i_{tune} : $1/f_{\text{tune}} = 1/f_{\text{tune},0} + \alpha_{\text{tune}} i_{\text{tune}}$. An initial thought was to use such an electrically tunable lens as a fast actuator to use in the z-feedback loop to increase the tracking bandwidth. However, the response time of the lens is on the order of a few ms, which is comparable to the piezo stage. I therefore do not expect to be able to use this lens for feedback purposes but it is a compact solution to generate relatively slow (up to a few tens of Hz) displacements of the beam focus.

Optical design for axial positioning and scanning with tunable lenses

Earlier in this chapter, we discussed the optical design that gives rise to optimal scanning properties, in the case where all the lenses had a fixed focal length. Here, we consider the case where one of the lenses has an adjustable focal length. Let us consider the simple system composed of the tunable lens (optical power P), followed by a static lens (optical power P_1) at a distance d_1 away from it. Using notations similar to section 3.1.2, we denote d the distance between the focus of the input beam

and the tunable lens, q the gaussian beam parameter at the input focus and q' the beam parameter just after the second lens. We denote $z_R = \pi w^2/\lambda$ and z_w (resp. $z'_R = \pi w'^2/\lambda$ and z'_w) the Raleigh range and the position of the axial position of the focus at the input (resp. output) of the optical system. The desirable scanning properties for this optical system are: 1. varying the focal power P of the tunable lens should not vary the waist of the output beam w' , and 2. varying the focal power P should maximally couple to a change in focus position z'

The transfer matrix between q and q' is now

$$M = \begin{pmatrix} 1 & d_1 \\ -P_1 & 1 - d_1 P_1 \end{pmatrix} \begin{pmatrix} 1 & d \\ -P & 1 - dP \end{pmatrix} \quad (3.15)$$

And using the propagation equations, we obtain the Raleigh range at the output

$$z'_R = \text{Im}(q') = \frac{z_R}{(-1 + d_1/f_1 + d(P + 1/f_1 - d_1/f_1 P))^2 + z_R^2(P + 1/f_1 - d_1/f_1 P)^2} \quad (3.16)$$

For the output waist size to be independant of P , we need to require that the distance between the tunable lens and the second lens f_1 be exactly one focal length f_1 . In that case, we obtain

$$z'_R = f_1^2 \frac{z_R}{(z_R^2 + d^2)} \quad (3.17)$$

Eq. (3.17) indicates that the output waist can be controlled by varying the position of the input focus d with respect to the tunable lens. Additionally, for $d = 1/f_1$, we can verify that the distance between the ouput focus and the lens f_1 is given by

$$z' = -\text{Re}(q') = f_1^2 \left(\frac{d}{(d^2 + z_R^2)} - (P - 1/f_1) \right) \quad (3.18)$$

The axial shift of the output focus is linear in the power of the tunable lens P , which is a nice property for scanning purposes.

The optical layout used in the microscope for axial scanning is shown fig 3.4.

The beam coming out of the AOM encounters the TAG lens which is situated at a distance $d_1 = f_1$ away from a lens of focal length f_1 . Changes in the focal

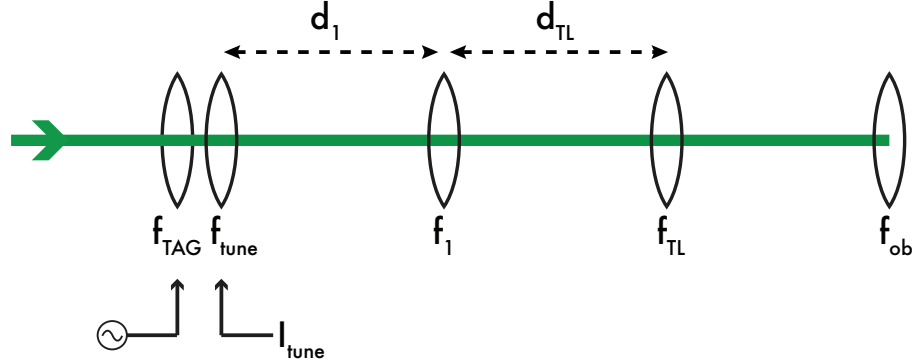


Figure 3.4: Basic optical layout for axial scanning using a tunable lens

length of the TAG result in an axial displacement of the focus past the lens f_1 , which is relayed to the sample via the tube lens f_{TL} and the microscope objective. An electrically tunable lens f_{tune} is placed right next to the TAG lens to bias the overall focusing power of the tunable element ($P = P_{TAG} + P_{tune}$). With this configuration, the axial displacement of the beam in the sample is linear in the current i_{tune} applied to the tunable lens. Additionally the amplitude of the modulation generated by the TAG lens is linear in the TAG lens driving signal amplitude V_{TAG} . Therefore, the displacement of the focus axial position in the sample Δz_0 is of the form

$$\Delta z_o = \left(f_1 \frac{f_{obj}}{f_{TL}} \right)^2 (\alpha_{TAG} V_{TAG} \sin(\omega t) + \alpha_{tune} i_{tune}) \quad (3.19)$$

Using this geometry, I have been able to observe more than $10\mu\text{m}$ of swing in the axial focus position in the sample during the lens oscillation cycle. To calibrate the effect of the lens and determine the amplitude of the axial modulation, I am using one of the AOM along the tracking beam path to shutter the beam with a low duty cycle square wave (10 percent duty cycle or less), phase locked with the lens driving signal. The beam position is then determined for several values of the phase using a fluorescent bead immobilized on the surface of the coverslip. The beam focus position is obtained by finding the position of the fluorescent bead that maximizes the fluorescence signal.

3.2 Mathematical description of the tracking dynamics

A thorough mathematical description of the dynamics can be found in [27, 26]. Here, I am investigating in more details the case where two actuators are used in the feedback loop: the piezo stage controls the sample position and cancels the low frequency components of the Brownian motion of the particle, whereas the AOM is used as a fast actuator to lock onto the higher frequency components of the Brownian motion. This allows me to discuss the choice of corner frequency, and obtain explicit expressions for the stage and laser correlation functions, which are usefull for fitting experimental data. Additionally, the dynamics of the tracking apparatus is described with a different formalism compared to the description in [27, 26]. To my perspective, this description has the advantage of allowing very compact calculations, and the correlation functions of the measured signals can be calculated in a straightforward manner.

3.2.1 General model for the tracking system dynamics

Consider the case of the feedback loop represented in fig. 3.5. The locking amplifier is integrated, and then fed to both the stage and the laser voltage controlled oscillator that drives the acousto-optic modulator to displace the laser beam, after a low pass and high pass filter stage respectively.

We represent the state of the tracking system by the state vector $x = (e, x_s, x_l, z, l)$ where e is the true error $e = x_p - x_s - x_l$ with x_p the particle position, x_l the laser position, x_s the stage position, and z is the integral of the lockin output l . The lockin-amplifier provides an electronic signal that is of the form

$$dl_t = -Bl_t + B(\alpha_{\text{err}}e_t dt + \eta dW_{n,t}) \quad (3.20)$$

where B is the lockin amplifier integration bandwidth, α_{err} is the error signal slope in mV/ μm and η is a noise density and $W_{n,p}$ is a standard Wiener process. Eq. (3.20) simply represents the output of the lockin amplifier as a low pass filtered version of

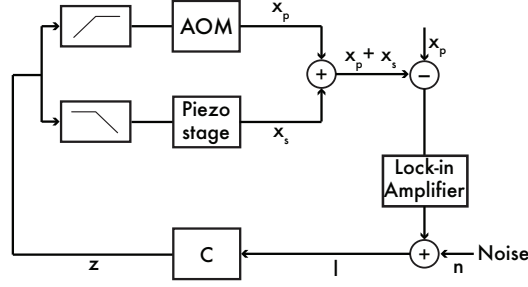


Figure 3.5: Tracking feedback loop used in the revised apparatus. The controller C is a pure integrator. The noise n originates from localization error due to counting noise. While it is represented past the lockin amplifier, it is in fact filtered by the lockin low pass

the error e_t to which a white estimation noise has been added. The values of α_{err} and η are function of the illumination geometry (tracking laser waist and rotation radius), as well as of the fluorescence rate f . More specifically these quantities can be expressed in the form

$$\alpha_{\text{err}} = a * f \quad (3.21)$$

$$\eta = \sqrt{f \sqrt{2 * a^2 * \theta^2}} \quad (3.22)$$

where a is the error signal slope per unit of fluorescence (a in $\text{mV}/(\mu\text{m} * \text{Hz})$) and θ is in a normalized noise density in (μm) such θ/\sqrt{f} is the true noise density in $\mu\text{m}/\sqrt{\text{Hz}}$. The advantage of expressions (3.21) is that the parameters θ and a are a function of the illumination geometry only.

The particle has a brownian motion described by the equation $dx_p = \sqrt{(2 * Dp)} dW_{p,t}$ where $W_{p,t}$ is a standard Wiener process independant of $W_{n,t}$. Therefore, the equation of motion for the state vector is the following linear stochastic differential equation.

$$dx = Mxdt + NdW_t \quad (3.23)$$

where the dynamics and noise matrices M and N are given for by

$$M = \begin{pmatrix} 0 & B_{\text{LP}} & B_{\text{HP}} & -B_{\text{LP}}G_s & -G_l \\ 0 & -B_{\text{LP}} & 0 & B_{\text{LP}}G_s & 0 \\ 0 & 0 & B_{\text{HP}} & 0 & G_l \\ 0 & 0 & 0 & 0 & 1 \\ B\alpha_{\text{err}} & 0 & 0 & 0 & -B \end{pmatrix} \quad (3.24)$$

$$N = \sqrt{2D_p}N_p + B\eta N_n, \quad N_p = \begin{pmatrix} 0 & 1 \\ 0 & 0 \\ 0 & 0 \\ 0 & 0 \\ 0 & 0 \end{pmatrix}, \quad N_n = \begin{pmatrix} 0 & 0 \\ 0 & 0 \\ 0 & 0 \\ 0 & 0 \\ 1 & 0 \end{pmatrix} \quad (3.25)$$

and

$$dW_t = \begin{pmatrix} dW_{p,t} \\ dW_{n,t} \end{pmatrix} \quad (3.26)$$

Equation (3.23) should not be too surprising. At the control level, the tracking microscope is a closed loop system that responds to a single measurement consisting in the stream of photons emitted by the fluorescent particle. As such, it can be viewed as a dynamical system driven by two stochastic inputs: the particle position, which follows a Brownian motion, and some noise related to the random nature of the photon emission process, which obeys Poissonian statistics. For sufficiently large fluorescence rates however (roughly when the number of photons collected during a time window $1/\beta$ where β is the unity gain frequency of the feedback loop is much larger than 1), the Poissonian statistics of the photon emission can be approximated by gaussian statistics. These two source of noises are represented here by the processes $dW_{p,t}$ and $dW_{n,t}$. Additionally, if we assume that the particle is tracked sufficiently well so that it stays near the center of the rotation (this is the relevant case in practice, otherwise the particle escapes the tracking system very quickly), the equations of motion should be linear.

It is easy to integrate eq. (3.23) which yields, assuming $X^{t=0} = 0$

$$X^t = \int_0^t e^{M(t-s)} dW^s \quad (3.27)$$

3.2.2 Mean square displacement of stage and laser

It is useful to derive an analytical expression for the correlation functions of the stage and the laser position because these correlation functions can be measured experimentally. Fitting the experimental data allows us to infer the diffusivity of the particle and the localisation noise. We describe a fitting strategy that reduces to a linear least-mean-sqaure problem with 2 degrees of freedom and does not involve detailed knowledge of the feedback loop. Define the correlation function for the state vector

$$\chi_X(\tau, t) = \mathbb{E} [X_{t+\tau} X_t^T] \quad (3.28)$$

The correlation function for the laser position is of the form

$$\chi_{x_l}(\tau, t) = \mathbb{E} [x_{l,t+\tau} x_{l,t}] = C_l \chi_X(\tau, t) C_l^T \quad (3.29)$$

where $C_l = (0, 0, 1, 0, 0)$ For the stage, rather than the correlation function which is a function of time (since the particle position is not a stationarry process since its variance grows as $2Dt$), we will compute the normalized mean square displacement defined as

$$m(\tau) = \frac{1}{2\tau} \mathbb{E} [(x_{s,t+\tau} - x_{s,t})^2] \quad (3.30)$$

We thus need to compute $\chi_X(t, \tau)$

$$\begin{aligned} \chi_X(t, \tau) &= \mathbb{E} [Z^{t+\tau} Z^{t^T}] \\ &= \mathbb{E} \left[\int_0^{t+\tau} e^{M(t+\tau-s)} N dB^s \int_0^t e^{M(t-s)} N dB^s \right] \\ &= e^{M\tau} \mathbb{E} \left[\int_0^t e^{M(t-s)} N dB^s \int_0^t e^{M(t-s)} N dB^s \right] \\ &\quad + e^{M\tau} \mathbb{E} \left[\int_t^{t+\tau} e^{M(t-s)} N dB^s \int_0^t e^{M(t-s)} N dB^s \right] \end{aligned} \quad (3.31)$$

Since the increments of a Wiener process are independent, the second term in the equation above cancels out. Furthermore, using the Ito Isometry, we can explicitly calculate the expectation value in the first term, which gives

$$\chi_X(t, \tau) = e^{M\tau} \int_0^t e^{M(t-s)} N N^T e^{M^T(t-s)} ds \quad (3.32)$$

By introducing

$$Q(t) = \int_0^t e^{Ms} N N^T e^{M^T s} ds \quad (3.33)$$

we get

$$\chi_X(t, \tau) = e^{M\tau} Q(t) \quad (3.34)$$

In practice, we are interested in the expression of the correlation function in the stationary regime (after the system loses memory of the initial conditions), so we can take the limit $t \rightarrow \infty$ in the expression above. We are tempted to write

$$\chi_X(t \rightarrow \infty, \tau) = e^{M\tau} Q_\infty \quad (3.35)$$

where

$$Q_\infty = \int_0^\infty e^{Ms} N N^T e^{M^T s} ds \quad (3.36)$$

The problem is that the eigenvalues of M are not necessarily all strictly negative, so Q_∞ is not finite and the expression above is not well defined. In fact, in the case discussed above where M is given by eq. (3.24), M clearly has a null eigenvalue. This stems from the fact that $x_{s,t}$ is included in the state vector, and the stage position is not bounded. In general, for an arbitrary dynamic matrix M , the tracking system is stable (marginally) as long as all the eigenvalues of M have a negative or null real part. In that case, by writing M as $M = P^{-1} \Delta P$ where Δ is diagonal, we can show that the $Q(t)$ has the form

$$Q(t) \sim Q_0 + Q_1 t + Q_2 e^{\tilde{\Delta} t} Q_2^t \quad (3.37)$$

where Q_0 and Q_1 are symmetric matrices of the same size as M (n), Δ is a diagonal

matrix of size $m = \text{rank}(M)$ with $\text{Re}[\tilde{\Delta}] < 0$ (stable eigenvalues), and Q_2 is an $n \times m$ constant matrix. Note that the matrices Q_0 and Q_1 satisfy the following continuous time Ricatti equations

$$Q_1 = MQ_0 + Q_0M^T + N^TN \quad (3.38)$$

$$0MQ_0 + Q_0M^T \quad (3.39)$$

By plugging the form (3.37) into eq. (3.34), we get the correct expression for the correlation function

$$\chi_X(t, \tau) = \lim_{t \rightarrow \infty} e^{M\tau} (Q_0 + Q_1 t) \quad (3.40)$$

We can now compute the correlation functions for the stage and laser position: The laser position x_p is a stationnary process, so we should have $C_l e^{M\tau} Q_1 C_l^T = 0$ and therefore the correlation function for the laser position is

$$\chi_{x_l}(\tau) = C_l e^{M\tau} Q_0 C_l^T \quad (3.41)$$

Using eq. (3.40), and ignoring the terms that grow as t as they should cancel out for a stable system, the normalized MSD for the stage reads:

$$m_{x_s}(\tau) = \frac{1}{\tau} (1 - e^{M\tau}) Q_0 + Q_1 \quad (3.42)$$

3.2.3 Model-free fitting of experimental correlation functions

Experimental correlation functions and MSD can be fitted to infer the value of D_p and η , as well as the other paramters in the matrix M. By writing N in the form of eq. (3.25), we obtain

$$NN^T = 2D_p N_p N_p^T + (\eta B)^2 N_n N_n^T \quad (3.43)$$

The correlation function for the laser position and stage can be expressed as

$$\chi_{x_l}(\tau) = 2D_p \bar{\chi}_{p,x_l}(\tau) + (\eta B)^2 \bar{\chi}_{n,x_l}(\tau) \quad (3.44)$$

$$m_{x_s}(\tau) = 2D_p \bar{m}_{p,x_l}(\tau) + (\eta B)^2 \bar{m}_{n,x_l}(\tau) \quad (3.45)$$

$$(3.46)$$

where $\bar{\chi}_{p,x_l}(\tau)$ and $\bar{\chi}_{n,x_l}(\tau)$ (resp. $\bar{m}_{p,x_l}(\tau)$ and $\bar{m}_{n,x_l}(\tau)$) represent the contribution of the particle diffusion and the noise to the laser correlation function (resp. stage MSD) and are only a function of the parameters in the matrix M. It follows that if M is known (ie. we know all the gains and corner frequencies), inferring D_p and η reduces to a simple linear mean least square problem. Eq. (3.44) is maybe even more useful in the case where the parameters in M are unknown (or in the case where the form of M itself is unknown). In that case, rather than fitting the correlation functions using additional free parameters, we can use a pair of calibration samples with 2 different known values of D_p (typically fluorescent beads immobilized on a coverslip ($D_p = 0$) or freely diffusing) to obtain an experimental measurement of $\bar{\chi}_{p/s,x_l}(\tau)$ and $\bar{m}_{p/s,x_s}(\tau)$. These functions fully describe the dynamics of the system and can be directly used to extract the diffusion coefficient of a target sample via a mean least square approach. This inference strategy does not require a priori knowledge on the feedback loop and is thus robust to modeling uncertainties.

3.2.4 Optimal tracking performance

We want the overall loop transfer function to look like a pure integrator [26]. Therefore, the gains and bandwidth are adjusted so that $G_s = G_p = G$ and $B_{LP} = B_{HP} = B_f$, where G is a common loop gain and B_c is the corner frequency at which the stage branch in the control loop rolls off and the laser branch rolls in. When these conditions are satisfied, the unity gain frequency for the loop is

$$\beta = afG \quad (3.47)$$

and it is possible to explicitly calculate the correlation matrices Q_0 and Q_1 .

Using the fact that the error signal is given by $e_t = C_e X_t$ with $C_e = (1, 0, 0, 0, 0)$ we obtain an expression for the tracking error

$$\text{var}(e_t) = \frac{Dp}{B} + \frac{Dp}{\beta} + \frac{\beta\theta^2}{f} \quad (3.48)$$

Optimal tracking is obtained by taking the locking bandwidth $B \rightarrow 0$ and for a choice of unity gain frequency given by

$$\beta_{\text{opt}} = \sqrt{Dp} \sqrt{\frac{f}{\theta^2}} \quad (3.49)$$

in which the tracking error becomes

$$\text{Var}(e_t)_{\text{opt}} = E[x] \quad (3.50)$$

As expected, since the acousto-optic and piezo stage actuators operate in parallel

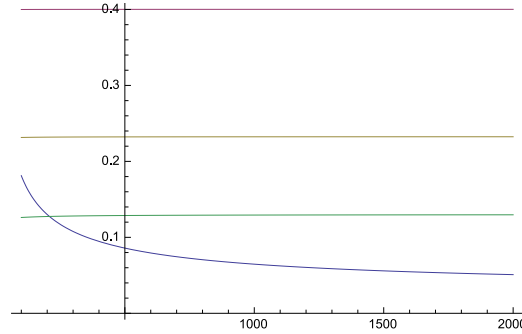


Figure 3.6: Tracking localization standard error $\text{std}(e_t)$ in μm as a function of the optimal unity gain frequency (blue). Green, yellow and red are laser motion amplitude $\text{std}(x_{l,t})$ for corner frequency of 10,30 and 100Hz respectively

to realize an ideal actuator with unity transfer function, we recover the result from [27]. In the present implementation however, the unity gain can be in principle chosen arbitrarily large, as we are not limited by the mechanical resonance of the stage (as long as the corner frequency B_c is chosen wisely, in practice 100Hz or less). The limitation of this implementation comes from the finite range of motion of the laser which is set by the maximum deflection angle of the acousto-optic modulator. It is therefore

important to consider the amplitude of the laser motion, which has the form

$$\text{Var}x_{l,t} = D_p \frac{\beta}{B_c(B_c + \beta)} + \frac{\theta^2}{f} \frac{\beta^2}{B_c + \beta} \stackrel{\beta \rightarrow B_c}{=} \frac{D_p}{B_c} \quad (3.51)$$

For a choice of corner frequency of 30Hz for example, if we set the threshold for the laser mean square displacement at $1\mu m^2$ (which is well within the achievable range of motion), we obtain an upper threshold on the particle diffusivity around $180\mu m^2/s$. This suggests that the limitation in our ability to track fast particles is essentially shot-noise limited. Finally, fig. 3.6 shows the optimal localization performance of the tracking feedback as function of the optimal unity gain frequency β_{opt} . The bottom line is that to achieve 100nm accuracy for a particle diffusing around $10\mu m^2/s$, we need to be able to track at about 1kHz closing frequency, which imposes constraints on the noise density θ/\sqrt{f} via the relation (3.49).

Chapter 4

End-to-end dynamics of DNA with tracking-FCS

In this chapter, I present an experiment that aimed at demonstrating that tracking-FCS can be applied to measure the distance fluctuations between two labeled sites on individual biological molecules. I carefully go through the various steps involved in the processing and interpretation of the obtained data.

4.1 Results

4.1.1 Description of the experiment

We first performed a tracking-FCS assay for two DNA samples of different size: a 979bp fragment (denoted 979OS) and a 472bp fragment (472OS). Both fragments were dual labeled with Cy3b at one end and Atto647N at the other end. Labeling was performed as described in the methods section. Cy3b and Atto647N were chosen for their good photostability. We have observed in particular greatly extended lifetime and increased brightness of Cy3b compared with Cy3 during tracking experiments in the same buffer environment. As a reference to monitor the dynamics of the tracking error, we measured correlation functions for control samples that were identical in length, but were labeled with Cy3b and Atto647N on the same end, 30bp away from

each other. This separation corresponds to a physical distance between the two dyes of about 10nm, which is sufficiently large to prevent any appreciable FRET, but well below our expected spatial resolution (10nm corresponds to 6nm after projection along one fixed axis). The fluctuations in Atto647N fluorescence for the single side labeled samples (denoted 979SS and 472SS) should therefore accurately represent the motion of the probe dye resulting from tracking error. For each of the four samples, we kept the probe laser in a constant offset position and acquired data until about 10 to 20 molecules were tracked. The laser position was then changed, and another set of 10 to 20 molecules were tracked. We only counted molecules that showed stable fluorescence from Atto647N for at least 1s. The series of laser position was chosen to cover a range between $\delta = 0$ (centered illumination) and $\delta = 2 \cdot w/2$.

4.1.2 Background correction

Before proceeding to computing the fluorescence correlation functions, we first subtracted the background noise from the fluorescence signal for each molecule. The background noise originates from autofluorescence of the sample, which is pumped by both the tracking laser (561nm) and the probe laser (635nm), and potentially from bleed-through of the Cy3b signal into the Atto647N channel. In these tracking-FCS experiments, the intensity of the probe 635nm laser is maintained constant, whereas the intensity of the tracking laser is adjusted through a feedback loop such that the fluorescence from the tracking dye remains at a constant predefined value. Locking the fluorescence from the tracking dye rather than the laser power is necessary to keep the gain (which is proportional to the fluorescence rate) of the tracking feedback constant. This property, combined with the observation that the main contribution to the background comes in fact from the Raman scattering of water induced by the 561nm illumination, makes it necessary to account for variations in brightness across individual molecules. Fig 4.1 illustrates the background calibration procedure for the 472bp DNA sample (similar data are obtained for the 979bp DNA sample).

For each molecule that exhibited a signal from Atto647N (referred to as type A molecules), we measured the average red fluorescence signal, as well as the average

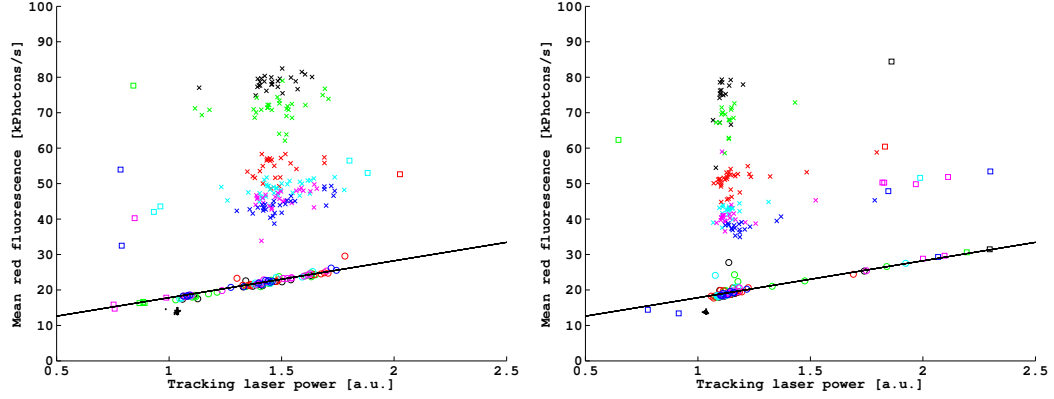


Figure 4.1: Brightness of individual molecules in the probe channel, plotted against tracking laser power (a.u.). This plot combines all the measured illumination conditions for the 472SS (left) and 472OS (right). Color represents offset value. Crosses are individual molecules retained for subsequent processing (type A). Circles are molecules used for background calibration (type B). Squares are outliers that are discarded from subsequent analysis. Black line is fitted background level as a function of green laser power. Solid black circles below black line are type C events

tracking laser power (determined by the feedback loop so as to lock the Cy3b signal at 70kPhotons/s and inversely proportional to the brightness of the molecule measured along the tracking channel). Averages were taken over the tracking window of the molecule. Additionally, the same two quantities (red fluorescence and green laser power) were measured for molecules for which no Atto647N signal was detected (type B molecules). For this population of molecules, we fitted the red fluorescence signal as an affine function of the green laser power. The affine function from the fit was then used to infer the background intensity and the background correction factor θ for molecules of type A. We noticed that the red fluorescence signal from the type B molecules was slightly higher than the signal measured in between tracking events, i.e. when no molecule is present in the laser focus (fig. 4.1). This suggests that a small amount of Cy3b fluorescence leaks into the red detection channel. We confirmed this hypothesis by computing the correlation function for the molecules of type B (used for background calibration), and for a set of traces of fluorescence recorded in between tracking events (type C traces). As shown in fig. 4.2, the correlation functions for

molecules of type B, unlike the correlations for type C traces, have a non-zero amplitude, and exhibit small oscillations at short timescales, which is a characteristic signal of a periodic modulation in the excitation signal. This modulation in fact corresponds to the rotation of the tracking laser. From fig. 4.1, we can also notice that for each value of the probe beam position offset, the distribution of brightness is dominated by a main cluster. This is consistent with a nearly homogeneous population of molecules labeled with a single Cy3b and a single Atto647N dye.

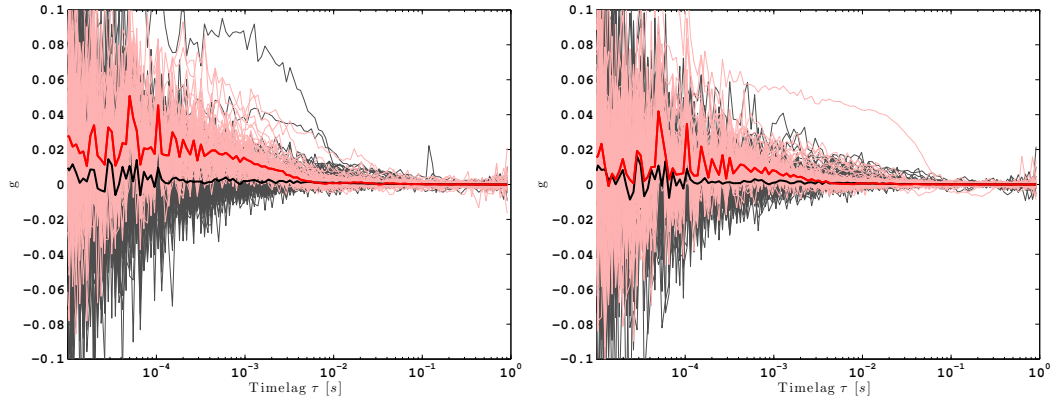


Figure 4.2: Correlation functions for background molecules (type B, red) and type C traces (black). Each thin line corresponds to an individual molecule (type B) or trace (type C). Thick lines are sample averages

For each molecule, the raw fluorescence correlation function was finally computed, and multiplied by the background correction factor θ according to eq.2.20.

4.1.3 Raw correlation functions

Fig 4.3 shows the raw correlation function data for the 4 different samples measured in the five illumination conditions. In this figure, light color lines represent individual molecules and thick lines are sample averages.

For all offsets and all samples, the raw correlation functions exhibit features on various timescales, ranging from $50\mu\text{s}$ to 10ms , that originate from end-to-end motion, tracking error, and dye blinking. We also observed oscillations on long time scales ($>10\text{ms}$) that originate from mechanical vibrations in the microscope that are not

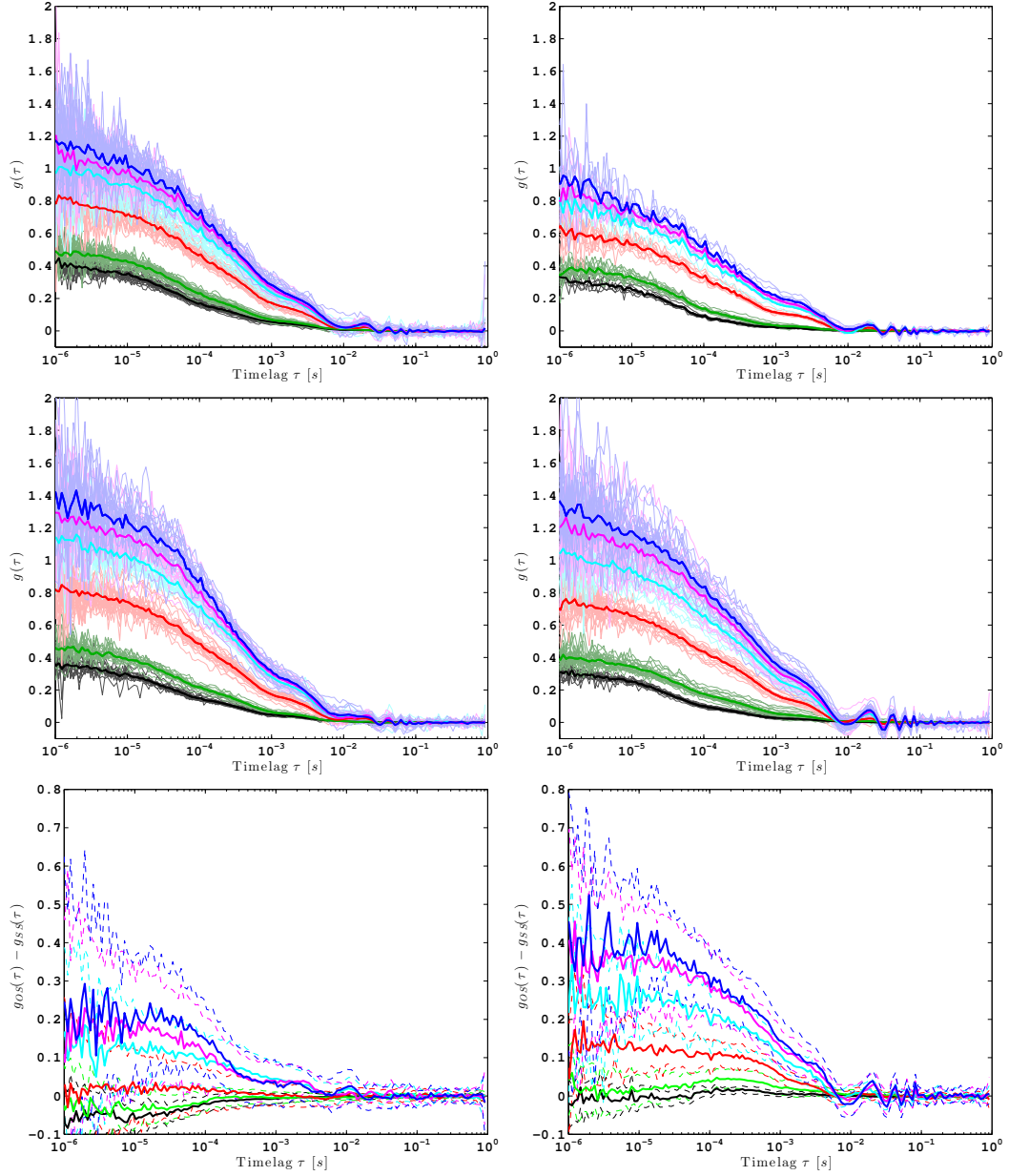


Figure 4.3: Raw correlation functions for 472SS (top left), 472OS (top right), 979SS (middle left) and 979OS (middle right). Difference between means of OS vs SS samples \pm sample std are represented in the bottom row (472OS-472SS bottom left, 979OS-979SS bottom right). Colors represent offset value δ_1 : 0 (black), 0.68 (green), 1.36 (red), 1.70 (cyan), 1.81 (magenta), 1.92 (blue)

canceled by the feedback loop. Information on the end-to-end dynamics for a given molecule length should appear as differences between same side and opposite side labeled samples. In order to better visualize potential differences, we subtracted the mean correlation function of each SS sample from that of the OS sample of matching length. While SS and OS samples look identical under central or near central illumination ($\delta = 0$ black, $\delta = 0.68$ green, $\delta = 1.36$ red), larger probe beam offsets clearly allow us to see a difference between the OS and SS labeling in both the 472bp and 979bp samples. To separate the various features in the raw fluorescence correlation functions and extract the position correlation for the end-to-end motion only, we then followed the processing pipeline discussed in chapter 1.

Relative correlation functions for DNA data

We first computed the relative correlation functions (eq.(2.44)), using different pairs of offset values δ_0 and δ_1 to serve as the reference and signal illumination conditions. More precisely, for each pair of offsets, the centered illumination was chosen as the reference offset δ_0 , and the correlation functions for this offset were averaged across molecules to provide the reference correlation. This reference correlation function was then subtracted from the correlation function corresponding to each molecule tracked under illumination condition δ_1 . This produced for each molecule of each sample a series of relative correlation function with increasing value for $(\delta_1 - \delta_0)$.

As expected, the relative correlation functions exhibited simpler features compared to the raw data. Noticeably, these correlation functions were completely flat at timescales shorter than $50\mu s$. This suggests that the contribution from the dye triplet-state dynamics, which we suspect to happen in the tens of μs timescale, is correctly suppressed. However, these data by themselves do not exclude the possibility that dye exhibit fluctuations at timescales above $100\mu s$ that are still present in the relative correlation functions and overlap with the signal coming from the dynamics itself. Future experiments, for example using surface immobilized molecules will be needed to confirm the suppression of dye dynamics at longer timescales.

Finally, we verified that the amplitude of the relative correlation function had a quadratic dependency in the beam position (fig. 4.5). Fig. 4.5 shows clearly that for

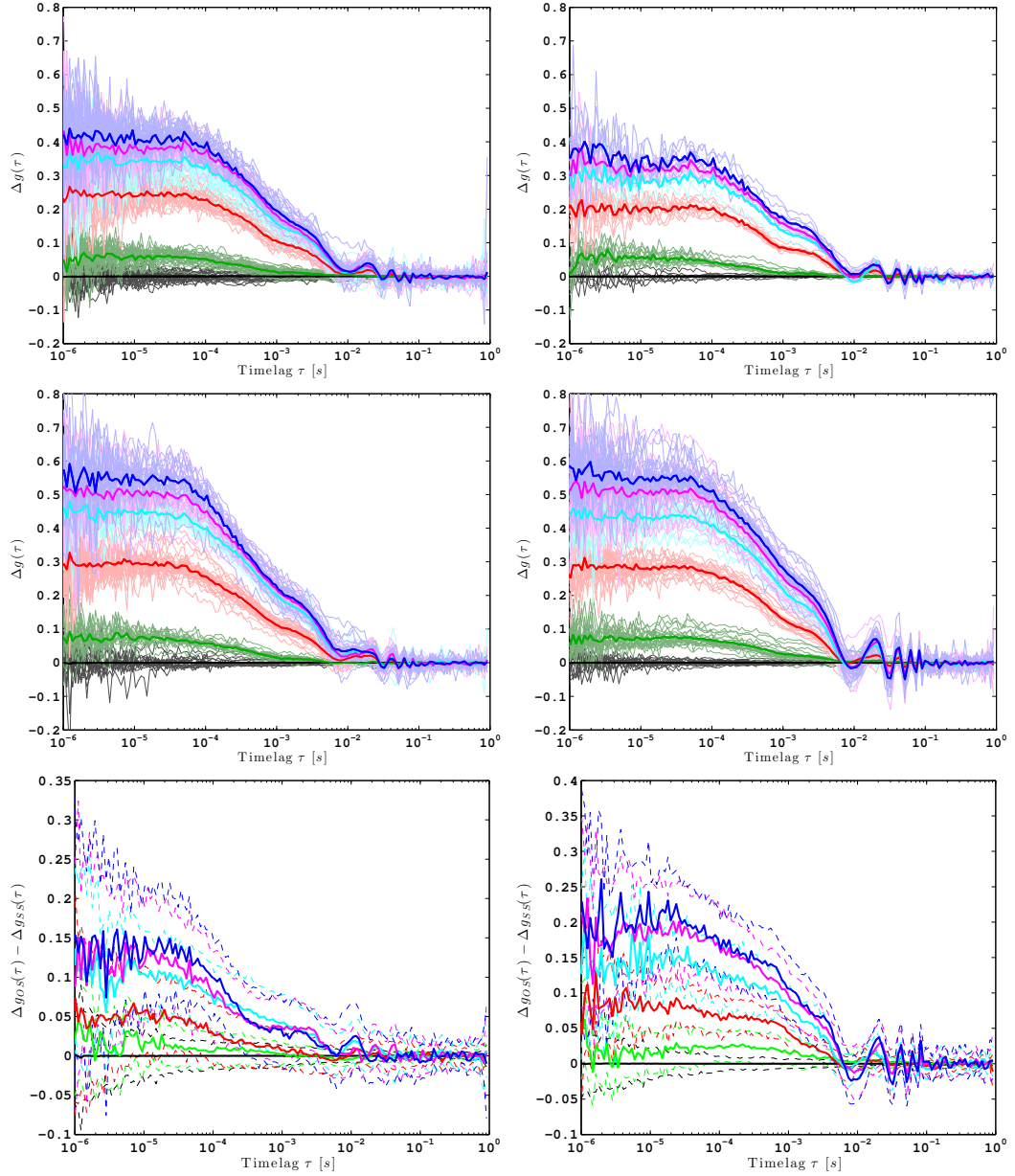


Figure 4.4: Relative correlation functions for all 4 samples and differences between OS and SS samples. Same plotting conventions as in fig. 4.3

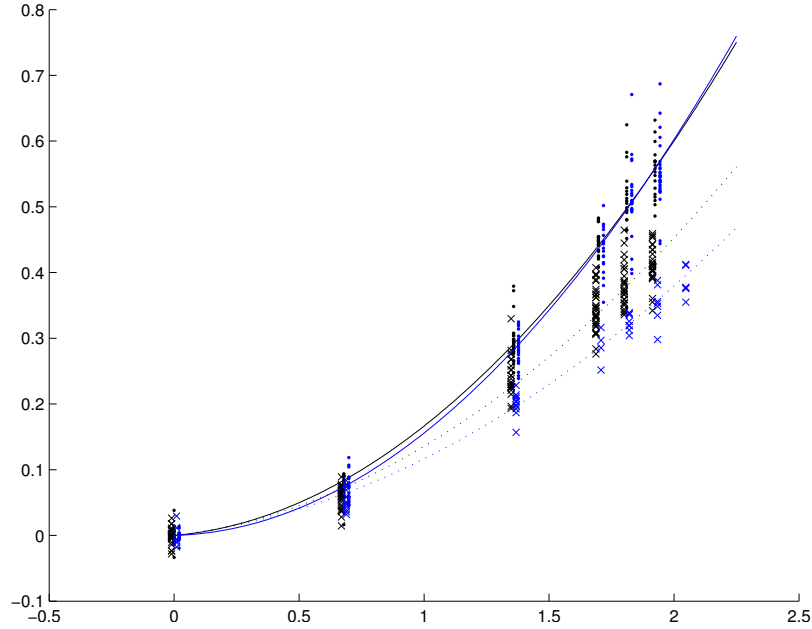


Figure 4.5: Amplitude of the relative correlation functions as a function of offset for all 4 samples. Marks are individual molecules (blue crosses and points are 979SS and 979OS respectively, and black crosses and points are 4720SS and 4720S). Plain and dotted lines are fitted quadratic functions (OS, SS samples respectively). The fact that we can resolve the end-to-end DNA dynamics for both the 472bp and 979bp samples is clearly visible on this plot. Note also the increase in tracking error for faster diffusing samples (472SS vs 979SS)

both the 472bp and 979bp samples, the end-to-end internal dynamics of the DNA is resolved above the tracking noise represented by the SS samples. Additionally, we observe that the tracking noise is large for the 472SS sample than for the 979SS sample. This is not surprising as the tracking error is expected to be larger for faster diffusing molecules.

Normalized relative correlation functions

To normalize the relative correlation functions, we used the two different approaches described in chapter 2. We first carried the normalization using the fact that we had access to calibrated values for the offset δ . Figure 4.6 shows the relative correlation functions normalized by simply dividing the data from fig. 4.4 by the squared offset

δ .

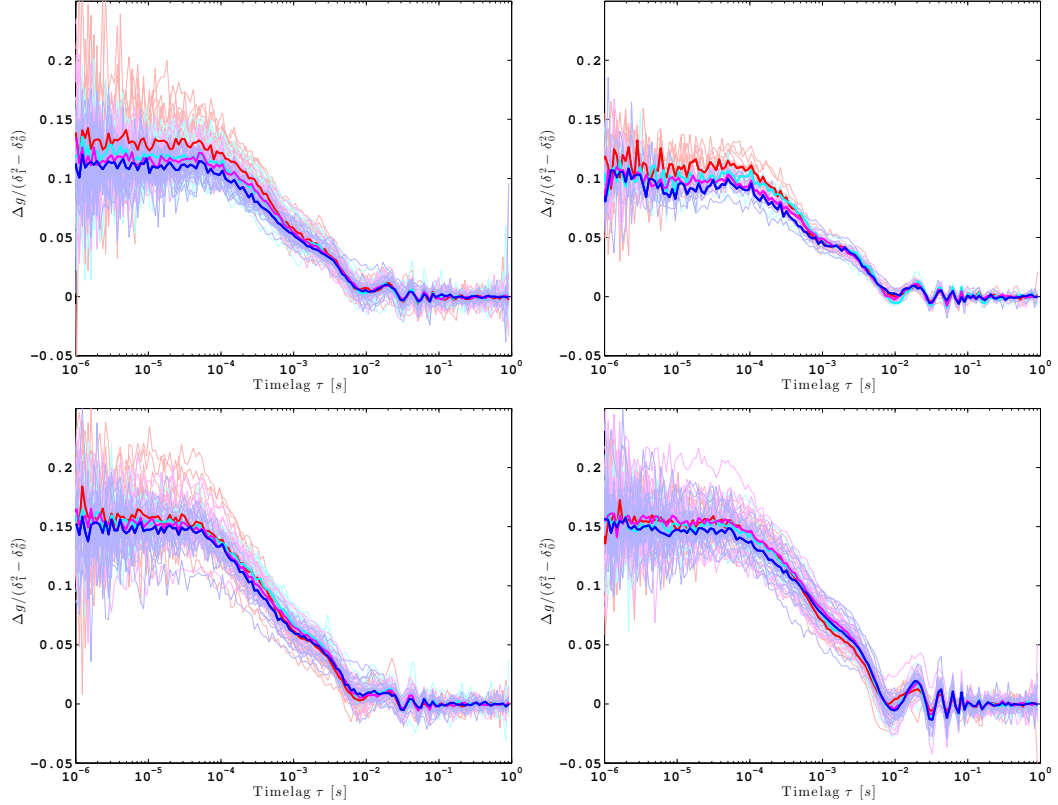


Figure 4.6: Normalized relative correlation functions using calibrated value of offset. for all 4 samples and differences between OS (bottom) and SS (top) samples. Same plotting conventions as in fig. 4.3, ie. color represents value of offset δ_1 . We discarded the smaller offset (green in previous figure) as the data at this offset were very noisy.

For both normalization procedures (fig. 4.6 and fig. 4.7) the resulting correlation curves were, as expected, independent of the choice of beam position.

Extraction of position correlation functions from intensity correlation functions

At this stage, the relative correlation functions are more easily interpretable than the raw data, as the effects of they dye blinking are canceled. However, they are still indirectly informative about the end-to-end dynamics, as they quantify fluctuations in fluorescence rather than fluctuations in end-to-end distance. The next step in

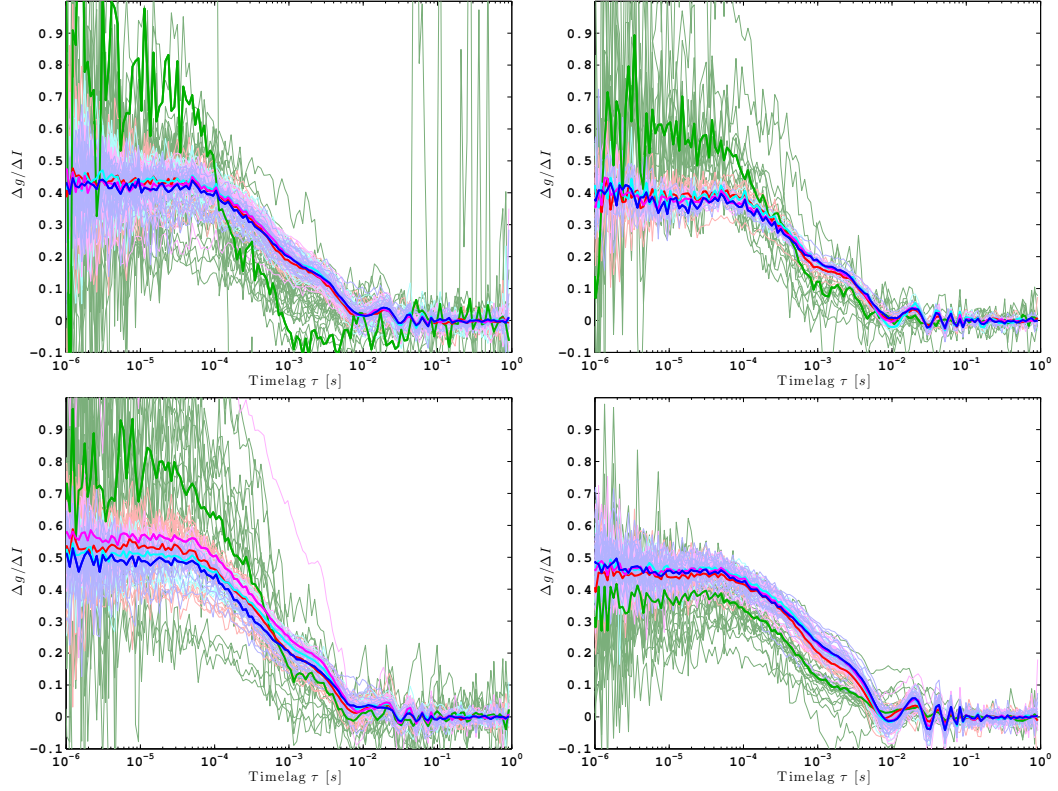


Figure 4.7: Normalized relative correlation functions using calibration free approach. for all 4 samples and differences between OS (right) and SS (left) samples. Same plotting conventions as in fig. 4.3. Top is SS samples, bottom is OS samples. Left is 472bp, right is 979bp

the tFCS data processing pipeline is to convert the fluorescence correlation functions into position correlation functions $\chi_x(\tau) = E[x_t x_{t+\tau}]$. Here, $x_t = x_{\text{im},t} + x_{\text{err},t}$ is the position of the probe dye relative to the tracking center and projected along the axis of probe beam offset (the axis that joins the foci of the tracking and probe beams). Inverting the non-normalized relative fluorescence correlation functions as described in chapter 1, we obtained the position correlation functions shown in fig. 4.8. Note that data in that figure were converted back to true distance units using a value of $w = 410\text{nm}$, and represent the square root of the correlation function rather than the correlation function itself. Thereby, the plateau value at short timescales represent the standard deviation of the probe dye motion. Note that these values obtained

from the SS samples indicate tracking accuracy of about 80nm for the 979bp sample, and 90nm for the 472bp sample

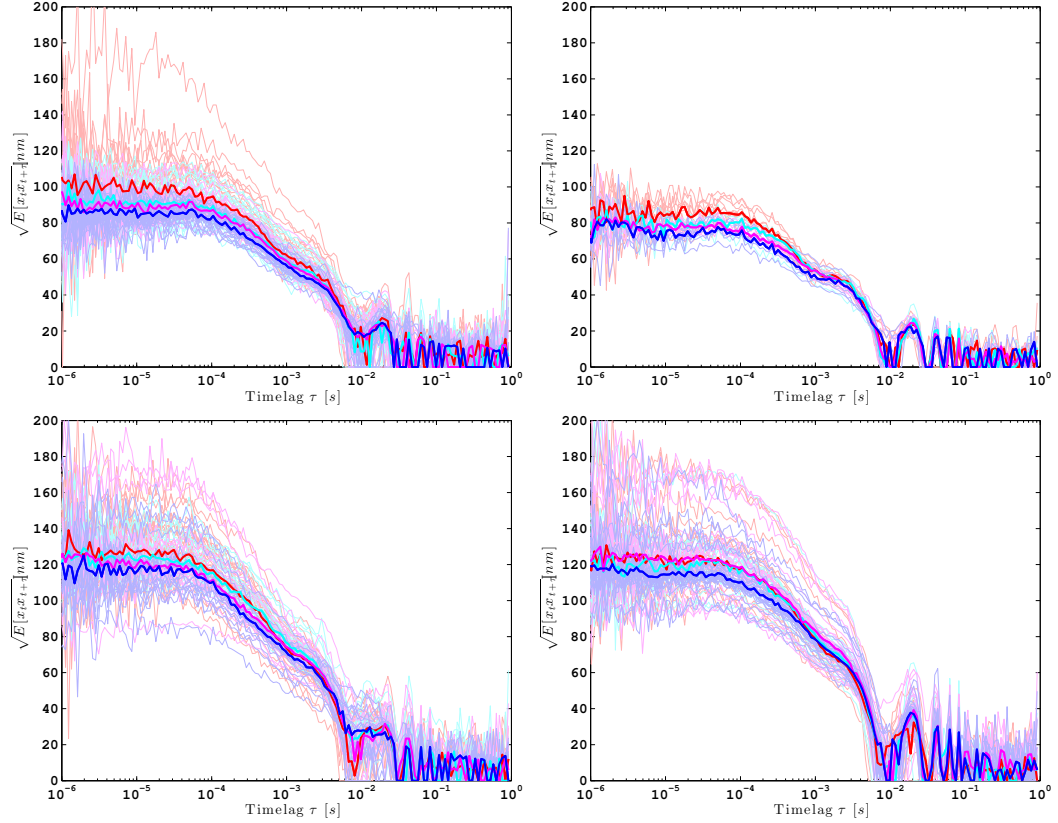


Figure 4.8: Probe dye position correlation functions obtained by inverting the non-normalized relative correlation function. Same plotting conventions as in fig. 4.3. Top is SS samples, bottom is OS samples. Left is 472bp, right is 979bp

Finally, we can also alternatively obtain $\chi_x(\tau)$ from the normalized relative correlation functions by following the calibration free method described chapter 2, as shown fig. 4.9.

Subtraction of tracking error and end-to-end correlation functions

Now that the intensity correlation functions have been converted into position correlation functions, we are ready to remove the tracking error contribution from the data and extract $\chi_{x_{im}} E[x_{im,t+\tau} x_{im,t}]$. To do so, to each position correlation function

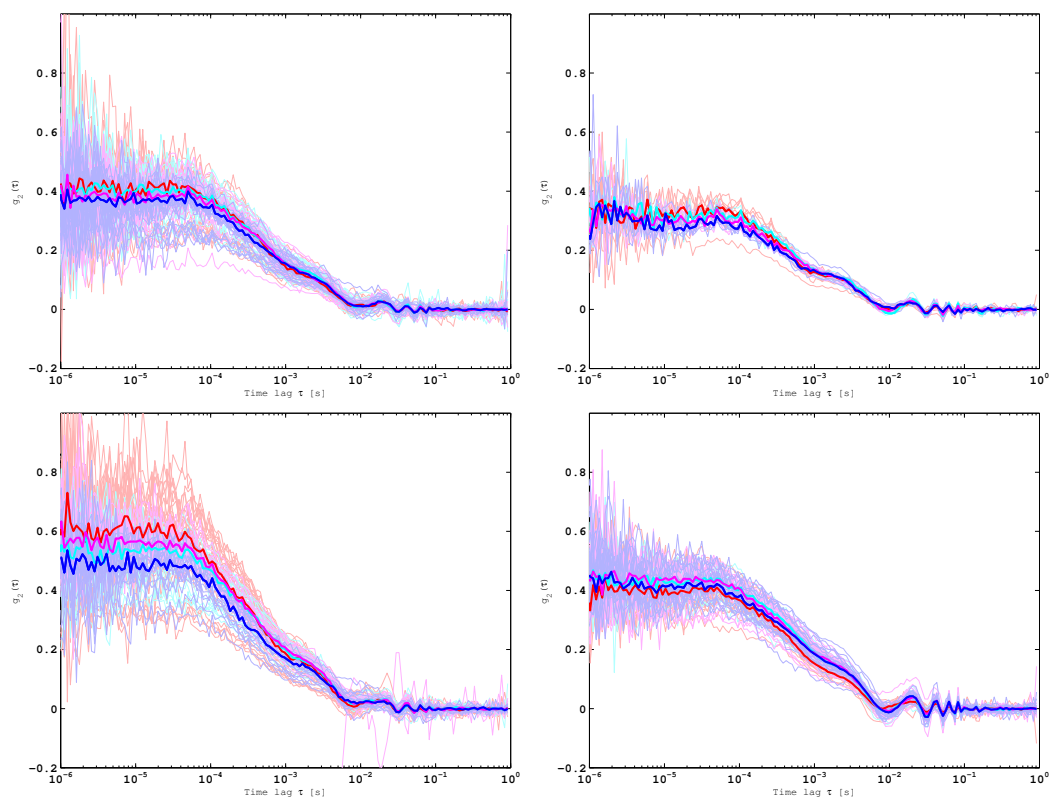


Figure 4.9: Probe dye position correlation functions obtained by inverting the normalized relative correlation function (calibration free approach). Same plotting conventions as in fig. 4.3.

corresponding to an individual molecule of the 472SS (resp 979SS), we subtract the average correlation function (across all the molecules) of the 472SS sample (resp. 979SS). Fig 4.10 represents the resulting end-to-end correlation functions, obtained by using the position correlation functions resulting from either the calibration free procedure (right, using data fig. 4.9), or the alternative procedure (left, using data fig. 4.8), and considering the largest offset only ($\delta = 1.92$).

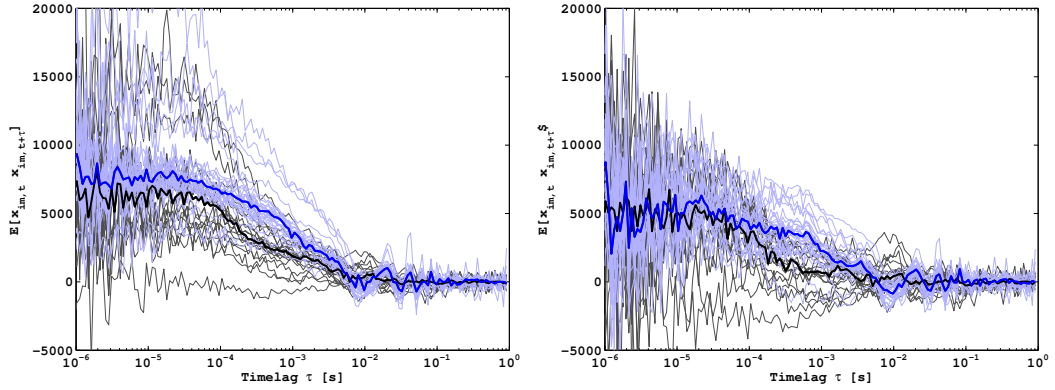


Figure 4.10: End-to-end correlation functions obtained by subtracting the position correlation from SS samples to the ones from OS samples. We used either the non-normalized correlation functions from fig. 4.8 (left), or the normalized correlation functions from fig. 4.9 (right). Black: 472bp OS, blue: 979bp OS

Using either approach, we are able to resolve an end-to-end dynamics signal, where the 472bp sample exhibits a faster correlation decay compared to the 979bp sample. However, the two approaches provide different values for the amplitude of the end-to-end motion ($\text{var}[x_{\text{im}}] = \lim_{\tau \rightarrow \infty} \chi_{x_{\text{im}}}$). I hypothesize that this discrepancy might be due do calibration errors, either for the offset δ , or for the beam waist w .

4.2 Initial data with switched-tFCS

The switched illumination tracking-FCS assay described in section 2.4 was applied to measure the end-to-end dynamics of DNA fragments of various length, ranging from 472bp to 6080bp. We chose the following DNA length: 472bp, 673bp, 979bp, 1618bp, 2467bp, 3873bp, and 6080bp. Similarly to what was done for the non-switched case,

for each length, we measured switched tracking-FCS spectra for molecules labeled with Cy3b and Atto647N either on opposite sides of the DNA fragment (OS) or on the same side of the DNA fragment, 30bp away from one another (see fig. 4.14). Data were processed according to the workflow described in section 2.4.

Typical switched-illumination tracking-FCS data

To illustrate the data obtained with a switched-TFCS assay, we first look in more details at the 979bp sample by itself. Fig. 4.13 shows experimental switched-illumination tracking-FCS data for the 979OS sample.

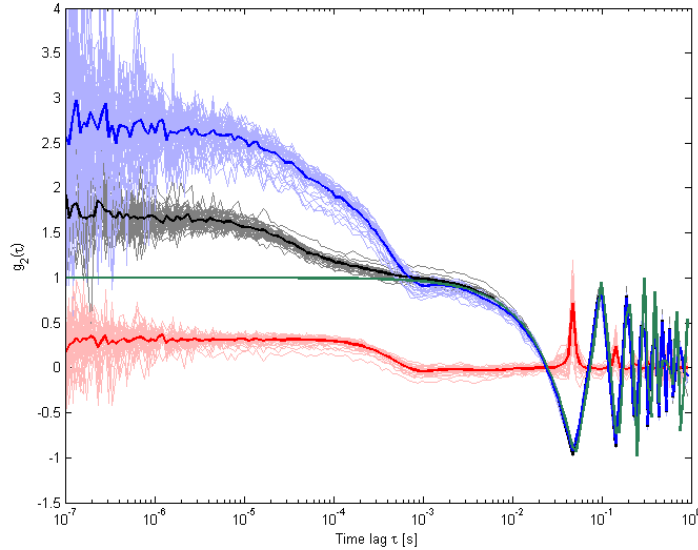


Figure 4.11: Switched-illumination tFCS data for a 979bp long dsDNA, with cy3b and Atto647N attached on opposite ends of the DNA. About 20 individual molecules were tracked, and intensity correlation was computed for each molecule and for the gated photon streams corresponding to both the 0 (black) and 1 (blue) illumination states. Thick lines represent mean (blue, state 1, black state 0). Relative correlation function (red) were obtained for each molecule by combining state 0 and state 1 correlation functions. Green is predicted correlation function for the strobing signal g_s

Switching between state 0 and state 1 was done at 10Hz, resulting in an oscillation of the autocorrelation that is apparent at long time lags (≥ 10 ms) and follows the

expected triangle wave pattern (green, time autocorrelation of the square switching signal showed in figure 2.9.a). The states 0 and 1 correspond to an offset value of respectively 0 and about 1.5 (we did not calibrate the offsets precisely for this experiment). As expected, contribution from the Atto647N-labeled end-motion within the probe beam (decay feature between 0.1 and 1ms) is larger in state 1 than in state 0, due to the steeper intensity gradient in state 1. The relative correlation only contains signal from the end-motion dynamics, and is flat over 3 orders of magnitude in time from $0.1\mu\text{s}$ to 0.1ms, suggesting cancellation of the triple-state dynamics. Note that the triangle wave signal due to the periodic switching between the two laser positions is also cancelled in the relative correlation, since it is a common feature of both state 0 and state 1. Narrow peaks in the relative intensity correlation appear above 10ms at the time lags where the switching g is near zero. These are due to the fact that correlations at timelags multiple of the switching half-period cannot be recovered from the gated signals.

Switched-illumination tracking-FCS data for DNA of various length

We next look at the data for the other sizes of DNA constructs. Fig. 4.12 shows the normalized relative correlation functions for the OS and SS constructs corresponding to the 7 different DNA length (472bp, 673bp, 979bp, 1618bp, 2467bp, 3873bp, and 6080bp). As expected, the SS constructs show similar correlation functions, with the differences in between the different length behind likely due to differences in tracking accuracy. The OS constructs on the other hand show a progression in the correlation functions. We observe an increase in the correlation amplitude with the length of the construct, and an increase in the characteristic timescales of motion (the correlation function takes longer to decay to zero).

Finally, we used the relative correlation data show in fig. 4.12 and the methodology described in chapter 3 to compute the correlation functions of the end-end vector (projected along the axis connecting the positions of the probe beam in state 0 and state 1). These represent directly the end-to-end dynamics of each DNA sample. Results are shown fig. 4.13.

We observe for the end-to-end correlation functions the same trend as for the

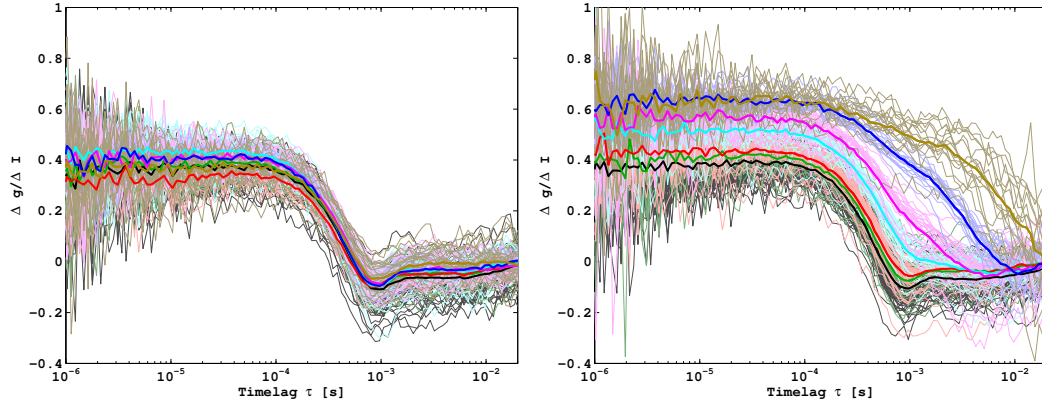


Figure 4.12: Normalized relative correlation functions obtained from switched tracking-FCS data. Each color corresponds to a given DNA length (black: 472bp, green: 673bp, red: 1618bp, cyan: 2467bp, magenta: 3873bp, brown: 6080bp). Thin lines are individual molecules, thick line are sample median. Left is SS labeling, right is OS labeling

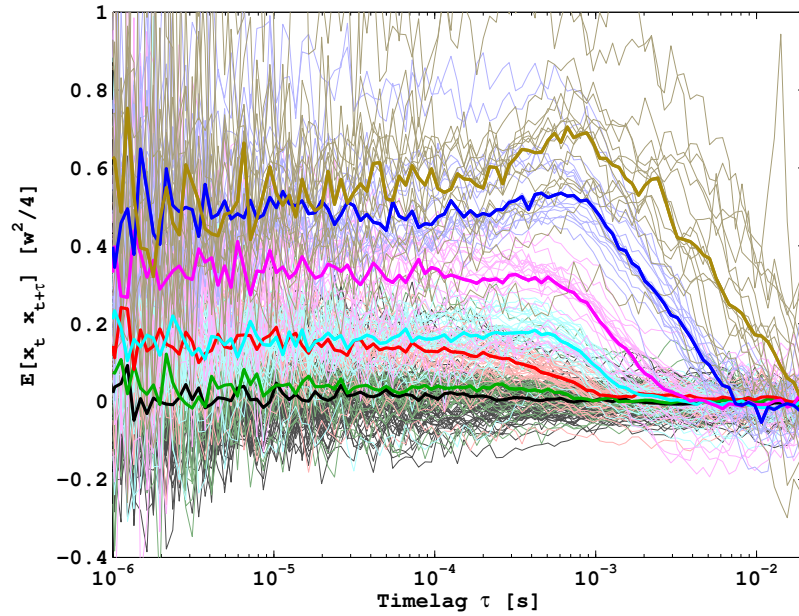


Figure 4.13: End-to-end correlation functions obtained from switched tracking-FCS data by inverting data from fig. 4.12 to extract position correlations and by subtracting SS correlations to OS correlations. Each color corresponds to a given DNA length (black: 472bp, green: 673bp, red: 1618bp, cyan: 2467bp, magenta: 3873bp, brown: 6080bp).

fluorescence correlations: the end-to-end motion amplitude (which is related to the radius of gyration) appears larger for longer molecules, while the dynamics get slower. Contrary to what we obtained in absence of switching, we were not able to resolve the end-to-end dynamics for the 472bp sample. I suspect this is due to poorer tracking performance at the time of this experiment (tracking performance depends on the quality of the microscope alignment). At the time of this writing, I intend to retake these data with the improved version of the apparatus. Additionally, it would be interesting to compare these experimental correlation functions with predictions from polymer dynamics theories.

4.3 Methods

Preparation of labeled DNA fragments

All the labeled DNA were prepared using a similar protocol, where short labeled ‘capping’ oligonucleotides were ligated onto the extremities of a long core DNA fragment of desired length. Each core DNA fragment was obtained by double restriction digest of a specific plasmid with XbaI and EcoRI, followed by gel electrophoresis and extraction. The plasmids were selected from the laboratory database based on their XbaI-EcoRI digestion pattern so as to produce XbaI-EcoRI fragments of the right length. The two ends of each core DNA fragment could then be addressed independently by ligation of universal capping oligonucleotides presenting a XbaI and EcoRI 5’ overhang respectively. To produce the capping oligonucleotides in a modular manner, we designed a small library of ssOligonucleotides each harboring a specific functionality (for ex: XbaI or EcoRI 5’end, Cy3b or Atto647N label, Biotin label). By annealing different subsets of sequences in the library, we could simply produced varied capping oligonucleotides that displayed any desired set of functionalities (ex: Cy3b label + EcoRI overhang, or Cy3b + Atto647N + XbaI overhang). Library sequence details and assembly protocols for each capping oligonucleotides are shown in the figure 4.14. Finally, various combination of capping oligonucleotides and core DNA fragments were ligated and gel purified, to obtain dual labeled DNA molecules

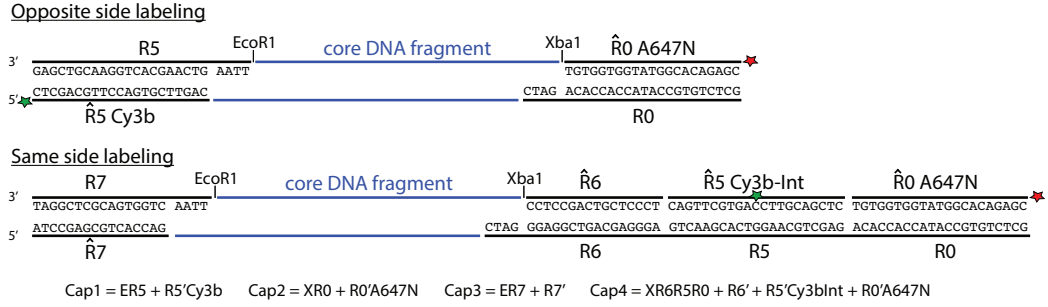


Figure 4.14: Protocol for assembly of SS and OS DNA constructs. Core DNA fragment of desired length is purified from plasmid and displays EcoRI and XbaI overhangs (central blue segment). Capping oligonucleotides Cap1-4 are assembled from our ssOligonucleotides library. ssOligonucleotides library are designed using a set of random sequences (R3,R5,R6). Capping oligonucleotides (black segments) have XbaI or EcoRI sticky ends that are used for ligation onto core DNA fragments

of different sizes that were either dual labeled with Cy3b and Atto647N on the same end (SS) or on opposite ends (OS). Unmodified single stranded DNA library sequences were obtained directly from IDT DNA. Fluorescently labeled ss-DNAs were prepared by conjugation of NHS-Ester reactive dyes (Monoreactive NHS-Ester Cy3b from GE Healthcare, NHS-Ester Atto647N from AttoTec) with amine-modified ssDNA (IDT), followed by PAGE purification.

Chapter 5

Future improvements and concluding remarks

5.1 Future Instrumentation developments

I list here what I think are some desirable technical improvements in the instrumentation.

5.1.1 Tracking bandwidth and axial control

With the use of acousto-optics as a fast actuator for feedback, the bandwidth of the plant along the X and Y axis can be considered as infinite for all practical purposes. However, the axial bandwidth is still essentially defined by the response of the piezo stage because the response time of the elastic polymer tunable lens is too slow (2ms) to allow for much faster locking than the piezo stage. However, I am, at the time of this writing, testing a fast feedback strategy that relies on strobing the tracking laser with a low duty cycle square wave synchronized to the TAG lens driving signal. Focus position can then be controlled by phase shifting the strobing signal. We have already implemented the phase shifting electronics, which operate on the strobing square wave directly and consists of a 12 bit shift register the clock frequency of which is set by a low frequency VCO to control the phase delay. An advantage of

this strategy is that the off time of the tracking laser can be synchronized with the on time of the probe laser, so as to completely get rid of fluorescence bleed through between the tracking and the probe channels. While the use of tunable optics is a promising approach, simpler or more versatile implementations would constitute important progress. For example, adaptive optics could potentially find applications in the tracking microscope.

5.1.2 Feedback loop in low photon count or large background regime

Demodulation of the tracking fluorescence signal by local oscillator mixing and low pass filtering (lock-in detection) is the optimal strategy for estimating the position of the particle in the case where the fluorescence rate is large (which corresponds to approximating the Poissonian counting noise during the integration bandwidth by a Gaussian noise). However, in the case where the fluorescence rate is low (on the order of the tracking bandwidth or less), better control strategies might be possible, that take into account the Poissonian nature of the emission and the dependence of the rate in the laser position. Dmitri Pavlichin did some initial work on applying HMM filters that can be applied to the single molecule tracking system. Additionally, even in the large fluorescence rate limit, the optimal unity gain frequency of the feedback loop is a function of the particle diffusivity. For this reason, filters that also estimate the diffusivity in real time have an advantage. How much the tracking performance can be improved using these approaches remains to be characterized.

5.1.3 Tunable beam waist

Suppression of the contribution from dye dynamics in tracking-FCS relies on combining correlation functions obtained with two different positions of the probe beam with respect to the tracking center. An alternative solution to deconvolve correlations from dye blinking and motion is to measure the dynamics using two different beam waist sizes. One beam waist would be chosen near diffraction limit for maximal sensitivity, whereas the other beam would be much larger. Since the large beam would

essentially be insensitive to the spatial motion of the probe site, this would likely improve the relative correlation signal. Implementation of this approach requires the ability to dynamically adjust the beam size, which could be done using tunable lenses and appropriate optical design.

5.2 Improvements and extensions of the tracking-FCS assay

5.2.1 Measuring static distances

In this thesis, I have described the use of tracking-FCS to measure the fluctuations in the distance between two sites. A natural question one might ask is: what about measuring distances that do not fluctuate? This is a highly desirable extension which can potentially find many useful biological applications for example in the characterization of multimolecular complexes. I can think of several ways to adapt the assay to measure a static distance between the probe and tracking dyes. The simplest strategy relies on taking advantage of the rotational diffusion, which generates rotation of the molecule in and out of the focus plane. This rotation induces in turn variation in the length of the vector joining the two sites and that is projected onto the measurement axis (the axis joining the foci of the tracking and probe beam). One important difference in the analysis of the correlation function in that case is that the motions along the three axes can no longer be assumed independent (because of the rigid rotation), and the analysis carried in chapter 2 therefore needs to be adapted.

In some cases, especially *in vivo*, it might be impractical to rely on the Brownian rotational diffusion because it might be for example too slow or constrained. In that case, one can use dual tracking strategies, where either small oscillations along the x axis or rotation in the xy plane is applied to the probe beam. The fluorescence signal can then either be demodulated by a lock-in amplifier to produce a position signal, or the fluorescence correlation function can be directly computed. With the latter approach, the amplitude of the oscillation in the correlation function relates to the distance between the average beam position and the probe dye.

5.2.2 Better Suppression of the tracking error

Strategies to quantify and suppress the contribution of tracking error to the correlation functions that do not rely on single-side (SS) labeled molecule would be highly useful. The data processing would then be respecting the single-molecule nature of the assay, since it would no longer be necessary to subtract from the tracking-FCS data the average tracking contribution as measured through the use of SS labeled samples. Multiple approaches for that are possible. The first solution is to use the statistics of the stage and laser displacement as described in chapter 2. Provided good calibration of the loop response using for example diffusing and immobilized beads, or ideally a homogenous sample, this approach should be very reliable as the reads from the stage and laser position sensors are completely independent from the reads from the fluorescence signal. Another solution would be to use fluorescence fluctuations measured on the tracking channel. The difficulty with that approach is that the tracking laser power is not constant but dynamically adjusted to maintain the fluorescence rate constant. In order to still obtain interpretable fluorescence fluctuations on the tracking channel, one would need for example to alternate at high frequency between two excitation modes: one with fluorescence lock, during which the fluorescence signal would be fed to the tracking controller, and another with laser intensity lock, during which the photons would be simply recorded for subsequent fluctuation analysis.

5.3 Conclusion and perspective

In this work, we have shown the applicability of two-color tracking-FCS to the measurement of the internal dynamics of individual molecules. We have highlighted the advantage of being able to control the illumination landscape seen by the molecule, which can serve as free parameter to tune the relative contribution of various processes aggregated in the correlation signal. This approach allows us to obtain correlation functions which are free of dye dynamics and easier to interpret than the correlation functions obtained in conventional FCS. We have demonstrated spatial

resolution well below the diffraction limit, even for single shot measurements of individual molecules, labeled with single dyes. The time resolution on these measurements was on the order of $10\mu\text{s}$.

One surprising result was that the smallest construct we measured (472bp) was only barely resolvable from the noise, despite being about 70nm in size. Given the theoretical predictions from Chapter 2, we expected the spatial resolution to be about at least twice as good. I suspect that the reason for this discrepancy is a tracking error along the z-direction that was larger than expected. I anticipate that the tracking error will be reduced in the 2nd revision of the instrument including the TAG lens for axial scanning, and that the experimental resolution should meet the theoretical prediction. Additionally, I have chosen to focus on performing single molecule tracking assays on molecules labeled with single dyes. The rationale behind this choice was to keep the molecule as wild-type as possible (minimal tagging). However, it would also make sense (especially if we wish to apply tracking-FCS *in vivo*) to use brighter albeit larger tags to improve the signal to noise, reduce the localization error, and increase the spatial resolution. This route is certainly worth investigating in the future.

A practical but remarkable aspect of the assay is its simplicity. Once the instrumentation is setup, and the labeled molecules are prepared (which is often the most challenging step!), a small volume of sample (typically $20\mu\text{l}$ at 1pM concentration) is simply injected in between two coverslips and data are ready to be collected within a minute. A tracking-FCS assay is as simple as a conventional FCS assay.

The measurements presented in the 4th chapter illustrate the usefulness of the tracking-FCS to address biophysical questions. The end-to-end correlation data obtained can be in principle directly used to test models for polymer dynamics. The range of DNA lengths that I was able to resolve covers the semiflexible to flexible transition, which is interesting from a biophysical and theoretical perspective. I expect the technique to be more generally applicable to the study of a broad range of biological systems. At the time of this writing, I have begun using tracking-FCS to measure CTCF mediated looping processes on short DNA segments displaying two or more CTCF binding sites. These studies should shed some light on ubiquitous regulation mechanisms involving long range contacts in the genome. In another field, we have

in collaboration with the Pfeffer Lab (Biochemistry, Stanford) initiated experiments that will measure the conformational dynamics of GCC185, a long 150nm coil-coil protein present at the surface of the trans-golgi network and involved in membrane trafficking and tethering processes.

I expect tracking-FCS measurements similar to the ones shown in vitro can be made in vivo. The specificities of the assay for in vivo contexts will need to be worked out, but the core ideas of the measurement should hold. For applications in vivo, tracking-FCS will surely benefit from the ongoing development of brighter and more stable fluorescent tags.

Bibliography

- [1] B MüllerHill. The function of auxiliary operators. *Molecular microbiology*, 29:13–18, 1998.
- [2] Euan McLeod and Craig B. Arnold. Mechanics and refractive power optimization of tunable acoustic gradient lenses. *Journal of Applied Physics*, 102(3):033104, 2007.
- [3] Sreenivasulu Kurukuti, Vijay Kumar Tiwari, Gholamreza Tavoosidana, Elena Pugacheva, Adele Murrell, Zhihu Zhao, Victor Lobanenko, Wolf Reik, and Rolf Ohlsson. CTCF binding at the H19 imprinting control region mediates maternally inherited higher-order chromatin conformation to restrict enhancer access to Igf2. *Proceedings of the National Academy of Sciences of the United States of America*, 103(28):10684–9, July 2006.
- [4] Les J Burke, Ru Zhang, Marek Bartkuhn, Vijay K Tiwari, Gholamreza Tavoosidana, Sreenivasulu Kurukuti, Christine Weth, Joerg Leers, Niels Galjart, Rolf Ohlsson, and Rainer Renkawitz. CTCF binding and higher order chromatin structure of the H19 locus are maintained in mitotic chromatin. *The EMBO journal*, 24(18):3291–300, September 2005.
- [5] Young Soo Yoon, Sangkyun Jeong, Qi Rong, Kye-Yoon Park, Jae Hoon Chung, and Karl Pfeifer. Analysis of the H19ICR insulator. *Molecular and cellular biology*, 27(9):3499–510, May 2007.
- [6] Jennifer E. Phillips and Victor G. Corces. CTCF: master weaver of the genome. *Cell*, 137(7):1194–211, June 2009.

- [7] Yusuke Miyanari, Céline Ziegler-Birling, and Maria-Elena Torres-Padilla. Live visualization of chromatin dynamics with fluorescent TALEs. *Nature Structural & Molecular Biology*, 20(11):1321 – 1324, 2013.
- [8] Bas Tolhuis, Robert Jan Palstra, Erik Splinter, Frank Grosveld, and Wouter de Laat. Looping and interaction between hypersensitive sites in the active beta-globin locus. *Molecular cell*, 10(6):1453–65, December 2002.
- [9] Job Dekker, Karsten Rippe, Martijn Dekker, and Nancy Kleckner. Capturing chromosome conformation. *Science (New York, N.Y.)*, 295(5558):1306–11, February 2002.
- [10] B Huang, M Bates, and X Zhuang. Super resolution fluorescence microscopy. *Annual review of biochemistry*, pages 993–1016, 2009.
- [11] Sebastian Berning, Katrin I Willig, Heinz Steffens, Payam Dibaj, and Stefan W Hell. Nanoscopy in a living mouse brain. *Science (New York, N.Y.)*, 335(6068):551, February 2012.
- [12] Yejun Wang, Shovamayee Maharana, Michelle D Wang, and G V Shivashankar. Super-resolution microscopy reveals decondensed chromatin structure at transcription sites. *Scientific reports*, 4:4477, January 2014.
- [13] C Zurla, a Franzini, G Galli, D D Dunlap, D E a Lewis, S Adhya, and L Finzi. Novel tethered particle motion analysis of CI protein-mediated DNA looping in the regulation of bacteriophage lambda. *Journal of Physics: Condensed Matter*, 18(14):S225–S234, April 2006.
- [14] Joel D Revallee, Gerhard a Blab, Henry D Wilson, Jason D Kahn, and Jens-Christian Meiners. Tethered particle motion reveals that LacIDNA loops coexist with a competitor-resistant but apparently unlooped conformation. *Biophysical journal*, 106(3):705–15, February 2014.
- [15] Hugo Geerts, M De Brabander, and Ronny Nuydens. Nanovid tracking: a new automatic method for the study of mobility in living cells based on colloidal gold and video microscopy. *Biophysical journal*, pages 775–782, 1987.

- [16] Chirlmin Joo, Hamza Balci, Yuji Ishitsuka, Chittanon Buranachai, and Taekjip Ha. Advances in single-molecule fluorescence methods for molecular biology. *Annual review of biochemistry*, 77:51–76, January 2008.
- [17] M J Saxton and K Jacobson. Single-particle tracking: applications to membrane dynamics. *Annual review of biophysics and biomolecular structure*, 26:373–99, January 1997.
- [18] Carmine Di Rienzo, Enrico Gratton, Fabio Beltram, and Francesco Cardarelli. Fast spatiotemporal correlation spectroscopy to determine protein lateral diffusion laws in live cell membranes. *Proceedings of the National Academy of Sciences of the United States of America*, 110(30):12307–12, July 2013.
- [19] Jörg Enderlein. Tracking of fluorescent molecules diffusing within membranes. *Applied Physics B*, 71(5):773–777, 2000.
- [20] Sri Rama, Prasanna Pavani, Michael A Thompson, Julie S Biteen, Samuel J Lord, Na Liu, Robert J Twieg, Rafael Piestun, and W E Moerner. imaging beyond the diffraction limit by using a double-helix point spread function. 106(9), 2009.
- [21] Valeria Levi, QiaoQiao Ruan, and Enrico Gratton. 3-D particle tracking in a two-photon microscope: application to the study of molecular dynamics in cells. *Biophysical journal*, 88(4):2919–28, April 2005.
- [22] Kevin McHale, Andrew J Berglund, and Hideo Mabuchi. Quantum dot photon statistics measured by three-dimensional particle tracking. *Nano letters*, 7(11):3535–9, December 2007.
- [23] Andrew J Berglund, Kevin McHale, and Hideo Mabuchi. Fluctuations in closed-loop fluorescent particle tracking. *Optics express*, 15(12):7752–73, June 2007.
- [24] Valeria Levi, QiaoQiao Ruan, Matthew Plutz, Andrew S Belmont, and Enrico Gratton. Chromatin dynamics in interphase cells revealed by tracking in a two-photon excitation microscope. *Biophysical journal*, 89(6):4275–85, December 2005.

- [25] Valeria Levi and Enrico Gratton. Exploring dynamics in living cells by tracking single particles. *Cell Biochemistry and Biophysics*, 48(1):1–15, May 2007.
- [26] a.J. Berglund and H. Mabuchi. Feedback controller design for tracking a single fluorescent molecule. *Applied Physics B: Lasers and Optics*, 78(5):653–659, March 2004.
- [27] a.J. Berglund and H. Mabuchi. Performance bounds on single-particle tracking by fluorescence modulation. *Applied Physics B*, 83(1):127–133, January 2006.
- [28] Peter Meister, Lutz R Gehlen, Elisa Varela, Véronique Kalck, and Susan M Gasser. Visualizing yeast chromosomes and nuclear architecture. *Methods in enzymology*, 470(10):535–67, January 2010.
- [29] Francesco Cardarelli, Luca Lanzano, and Enrico Gratton. Fluorescence correlation spectroscopy of intact nuclear pore complexes. *Biophysical journal*, 101(4):L27–9, August 2011.
- [30] Andrew Berglund and Hideo Mabuchi. Tracking-FCS: Fluorescence correlation spectroscopy of individual particles. *Optics express*, 13(20):8069–82, October 2005.
- [31] Kevin McHale and Hideo Mabuchi. Precise characterization of the conformation fluctuations of freely diffusing DNA: beyond Rouse and Zimm. *Journal of the American Chemical Society*, 131(49):17901–7, December 2009.
- [32] Saveez Saffarian and Elliot L Elson. Statistical analysis of fluorescence correlation spectroscopy: the standard deviation and bias. *Biophysical journal*, 84(3):2030–42, March 2003.
- [33] T Wohland, R Rigler, and H Vogel. The standard deviation in fluorescence correlation spectroscopy. *Biophysical journal*, 80(6):2987–99, June 2001.
- [34] DE Koppel. Statistical accuracy in fluorescence correlation spectroscopy. *Physical Review A*, 10(6), 1974.

- [35] H Qian. On the statistics of fluorescence correlation spectroscopy. *Biophysical chemistry*, 38(1-2):49–57, October 1990.
- [36] Ted a Laurence, Samantha Fore, and Thomas Huser. Fast, flexible algorithm for calculating photon correlations. *Optics letters*, 31(6):829–31, March 2006.
- [37] M Jeanblanc, M Yor, and M Chesney. *Mathematical methods for financial markets*. 2009.
- [38] KL McHale. *Feedback tracking and correlation spectroscopy of fluorescent nanoparticles and biomolecules*. PhD thesis, 2008.
- [39] AJ Berglund. *Feedback Control of Brownian Motion for Single-Particle Fluorescence Spectroscopy*. PhD thesis, 2006.
- [40] Gaddum Duemani Reddy and Peter Saggau. Fast three-dimensional laser scanning scheme using acousto-optic deflectors. *Journal of biomedical optics*, 10(6):064038, 2014.
- [41] Guanghao Zhu, James van Howe, Michael Durst, Warren Zipfel, and Chris Xu. Simultaneous spatial and temporal focusing of femtosecond pulses. *Optics express*, 13(6):2153–9, March 2005.
- [42] E McLeod, AB Hopkins, and CB Arnold. Multiscale Bessel beams generated by a tunable acoustic gradient index of refraction lens. *Optics letters*, 31(21):3155–3157, 2006.
- [43] Nicolas Olivier, Alexandre Mermillod-Blondin, Craig B Arnold, and Emmanuel Beaurepaire. Two-photon microscopy with simultaneous standard and extended depth of field using a tunable acoustic gradient-index lens. *Optics letters*, 34(11):1684–6, July 2009.
- [44] Martí Duocastella. Simultaneous imaging of multiple focal planes for three-dimensional microscopy using ultra-high-speed adaptive optics. . . . of *biomedical optics*, pages 8–11, 2012.

- [45] Benjamin F Grewe, Fabian F Voigt, Marcel van 't Hoff, and Fritjof Helmchen. Fast two-layer two-photon imaging of neuronal cell populations using an electrically tunable lens. *Biomedical optics express*, 2(7):2035–46, July 2011.